Inferring atomic line parameters from solar spectra

Dissertation

zur Erlangung des mathematisch-naturwissenschaftlichen Doktorgrades

"Doctor rerum naturalium"

der Georg-August-Universität Göttingen

im Promotionsstudiengang Physik

der Georg-August University School of Science (GAUSS)

vorgelegt von

Dušan Vukadinović

aus Niš, Serbia

Göttingen, 2023

One never notices what has been done;
one can only see what remains to be done.

Maria Skłodowska-Curie

Contents

Contents

Summary

The proximity of the Earth to the Sun offers a unique opportunity to study different plasma phenomena that occur in its atmosphere, which are unattainable in plasma laboratories. Advances in the instruments used for solar observations brought a wealth of high-quality, low-noise data that give insight into the dynamics of small scales ($\sim 70\,\mathrm{km}$) in the solar atmosphere and its magnetic properties. Along with the developments in instrumentation, methods used to analyse these observations have also improved, allowing for more feasible inference of different physical parameters of the solar atmosphere, such as temperature, velocity and magnetic field. Concurrently, the solar atmosphere can also be used as an atomic physics laboratory to infer atomic parameters.

Over many decades, the spatially averaged disc-centre quiet-sun spectrum has been used to infer the transition probability (also known as $\log(gf)$) of many spectral lines, predominantly in the visible and infrared wavelengths. The advancement in this field was achieved with the pixel-by-pixel based inference of the $\log(gf)$ parameter from spatially resolved spectropolarimetric observations. In this thesis, I developed a new method called the coupled method, which infers spatially coupled atomic line parameters from high spatial and spectral resolution spectropolarimetric observations of the solar atmosphere. The coupling of atomic parameters across the observed field of view is a natural consequence of atomic parameters being independent of the underlying physical structure of the solar atmosphere. The coupled method simultaneously fits all observed spectra from a given field of view and infers the atmospheric and atomic parameters self-consistently. Part of this thesis is also dedicated to developing a new inversion code in which I have integrated the coupled method.

The strength of the coupled method is in resolving the contribution of blended spectral lines and retrieving their $\log(gf)$ parameter and the central wavelength reliably. This result is achieved by coupling spectra emerging from atmospheres with very diverse thermodynamic and magnetic structures, such as those describing atmospheres of umbra, penumbra, granules and intergranular lanes. This result is essential for analysing near ultraviolet observations of the solar atmosphere, where spectral lines are severely blended. Many of these lines have poorly determined atomic parameters that impact the inference of atmospheric parameters from this spectral region.

The coupled method is tested on spectra formed under the assumption of local thermodynamic equilibrium (LTE), where the populations of atomic levels are determined from the Boltzmann-Saha distribution. The method can be extended to infer other atomic parameters of lines formed under the assumption of LTE, such as the lower excitation level, abundance, Landé g-factors, and collisional broadening coefficients. However, it is also flexible enough to be applied to the non-LTE lines, for which the LTE assumption fails. The coupled method is applicable to spectral lines from the near ultraviolet to the

Contents

infrared.

Introduction

The Sun is a G2 main-sequence star with an effective temperature of 5777 K, radiating most of its energy in the visible wavelength range around 500 nm (Stix 2004). Even though it is the closest star to the Earth, sending a space probe to obtain in situ measurements of the physical conditions in its atmosphere is impossible. The observable layers of the Sun from which the radiation can escape freely, without any interaction with the surrounding particles, make up the solar atmosphere. The Parker Solar Probe (Fox et al. 2016) is the only spacecraft that has successfully reached the outermost layers of the solar atmosphere called the corona and obtained in situ measurements from its million-degree plasma (Raouafi et al. 2023). Solar physicists are compelled to rely predominantly on observations obtained remotely using space-based and ground-based solar telescopes. The currently available suite of solar telescopes and instruments allows for routine observations of features in the solar atmosphere and can resolve structures with horizontal spatial scales as small as roughly $60 - 70$ km (Schlichenmaier et al. 2016, Campbell et al. 2023).

Different features are observed on the solar surface, such as bright granules and dark intergranular lanes, which are a manifestation of the convective plasma motion occurring in the solar convective zone; sunspots and pores as concentrations of strong magnetic fields that inhibit the plasma convection. In higher layers of the solar atmosphere, observations show bright structures surrounding sunspots called chromospheric plages, and they have counterparts at the solar surface named faculae. Observations of even higher atmospheric layers of the Sun show a plethora of features having very complex forms that are structured by the magnetic field, such as prominences, filaments, spicules and coronal loops. The Sun is used to better understand distant stars that are poorly resolved[1], test plasma theories in environments unattainable in laboratories on Earth and study the interaction between plasma, magnetic field and radiation field.

Physical conditions prevailing in the solar atmosphere are inferred by analysing the intensity variation in different wavelength bands (photometry) or its variation with wavelength (spectroscopy). Radiation emitted from a solar (or stellar) surface passes through its atmosphere where it interacts with different atoms, ions and molecules[2]. These interactions that imprint the physical conditions of the solar atmosphere onto the radiation field can be of two kinds: continuum and line processes. Spectral lines, superimposed on the continuum, result from electronic transitions between bound energy levels of atoms.

In the solar atmosphere, radiation is polarised by the magnetic field through the Zee-

---

[1] Only the surface of giant stars can be imaged using interferometric measurements (e.g., Roettenbacher et al. 2017). However, the resolution of these observations is incomparable to the resolution of solar observations.

[2] Throughout the thesis atoms, ions, and molecules will be referred to uniformly as atoms to simplify writing, unless the explanation requires a distinction between them.

man and Hanle effects and by scattering processes because of the anisotropy of the radiation field close to the solar surface. Spectropolarimetry is an analysis technique that studies the intensity and polarisation variations with wavelength. Spectropolarimetric analysis of different spectral line profiles observed in the solar spectrum is used to infer depth variations of the physical parameters in the solar atmosphere, such as the temperature, velocity and magnetic field vector. The generation, transport and orientation of the magnetic field vector, extending from the deepest layers of the solar atmosphere up to the outer layers, is important to understand the structure of the solar atmosphere.

Inference of physical parameters from spectral lines relies on the precision of adopted parameters describing atomic species: energies of atomic levels, transition probabilities, Landé g-factors, central wavelengths of spectral lines, broadening coefficients, abundances, etc. These atomic parameters can be estimated in laboratory setups (e.g., Blackwell & Collins 1972), from theoretical computations of atomic models (e.g., Cowan 1981) or from the observed stellar (e.g., Laverick 2019) and solar spectra (e.g., Borrero et al. 2003). Despite these techniques, many spectral lines that are observed in the solar spectrum (as well as in some stellar spectra) have poorly determined atomic parameters (Kurucz 2002, Shapiro et al. 2010) or are not even identified (Nave et al. 2017).

This thesis presents a novel technique which can be used to infer the atomic parameters from high spatial and spectral resolution spectropolarimetric observations of the solar atmosphere. We show that the atomic parameters can be inferred using a spectropolarimetric inversion method, which iteratively corrects atmospheric and atomic parameters simultaneously until the best match with the observations is achieved. The inversion method developed in the thesis relies on the self-consistent inference of the atmospheric and atomic parameters by imposing a coupling in the latter. This thesis aims to complement high-quality laboratory measurements and improve the currently available theoretical estimates of atomic parameters for spectral lines in wavelengths from the near ultraviolet to the infrared region.

The thesis has the following structure: Chapter 1 briefly describes the thermodynamic and magnetic properties of the solar atmosphere. Furthermore, the radiative transfer theory of polarised light through a solar/stellar atmosphere is presented. After that, different methods for estimating the atomic parameters are reviewed, which will help develop a sense of uncertainties in the inferred atomic parameters. The radiative transfer theory from the first chapter establishes a basis for understanding the inversion methods described in Chapter 2 and the new inversion method developed in this thesis. Chapter 3 describes the new inversion code, `globin`, that has implemented an inversion method for coupled inference of atomic line parameters. The chapter focuses on the implementation and different techniques for optimising the inversion algorithm to retrieve reliable atomic line parameters. Chapter 4 lists some preliminary results and promising ideas to which we intend to apply the `globin` code and the coupled method for inferring atomic line parameters. The conclusions of the work presented in this thesis are given in Chapter 5.

1 Theoretical background

1.1 The solar atmosphere

Solar energy is generated in nuclear fusion processes in the solar core as high energy γ photons that interact with the surrounding plasma and deposit their energy. The transfer of energy by radiation inside the Sun establishes a region known as the radiative zone that extends from the edge of the solar core (at $0.25\,R_\odot$) up to the tachocline at $\sim 0.7\,R_\odot$. From the tachocline to the surface of the Sun (the convective zone), the energy is predominantly transferred by convective plasma motions. Above the solar surface, the energy is again predominately transported by radiation throughout the solar atmosphere.

The solar photosphere is the deepest visible layer of the solar atmosphere from which the majority of radiation is emitted, and it lies on top of the convective zone. The characteristic features observed in the solar photosphere are granules, which are surrounded by intergranular lanes (Fig. 1.1). The granules are convective blobs that transport heat from the convective zone to the surface. In the granule centre, hot plasma travels upwards until it reaches the surface. Then, the plasma cools through radiative emission and has a predominantly horizontal motion. The cool plasma gathered in the intergranular lanes is heavier (denser) than the surrounding material and starts to sink. Sunk plasma gets heated up again, and the whole process repeats. The average lifetime of a granule is around 6 min, where the lifetime is dependent on a granule size: larger granules live longer (Bahng & Schwarzschild 1961). On average, granules have a diameter of around 1 Mm.

Since the central regions of granules carry hot plasma, these regions are brighter than the surrounding intergranular regions, which are cooler and emit less radiation (Fig. 1.1). The regions on the Sun which consist predominantly of granules and intergranular lanes are known as quiet-sun regions, and they are permeated with hG magnetic fields (e.g., Orozco Suárez et al. 2007) producing weak polarisation signals. The photospheric plasma motion governs the magnetic field structure in the quiet-sun regions. The magnetic field is said to be frozen into the plasma because the magnetic energy is lower than the kinetic plasma energy (Alfvén theorem; Alfvén 1942). The ratio of the kinetic plasma energy density to the magnetic field energy density is known as a plasma β parameter (e.g., Goedbloed & Poedts 2004) and in the quiet-sun region in the photosphere, it is much larger than unity (see for example Fig. 6 from Jurčák et al. 2020).

The horizontal plasma motions from the granule centres carry the frozen-in magnetic field into the intergranular lanes, thus forming magnetic flux concentrations. This increase in the magnetic energy causes the plasma β parameter to drop below unity. Because of the increase in the magnetic energy, the plasma down-flow is hindered, and the pressure scale
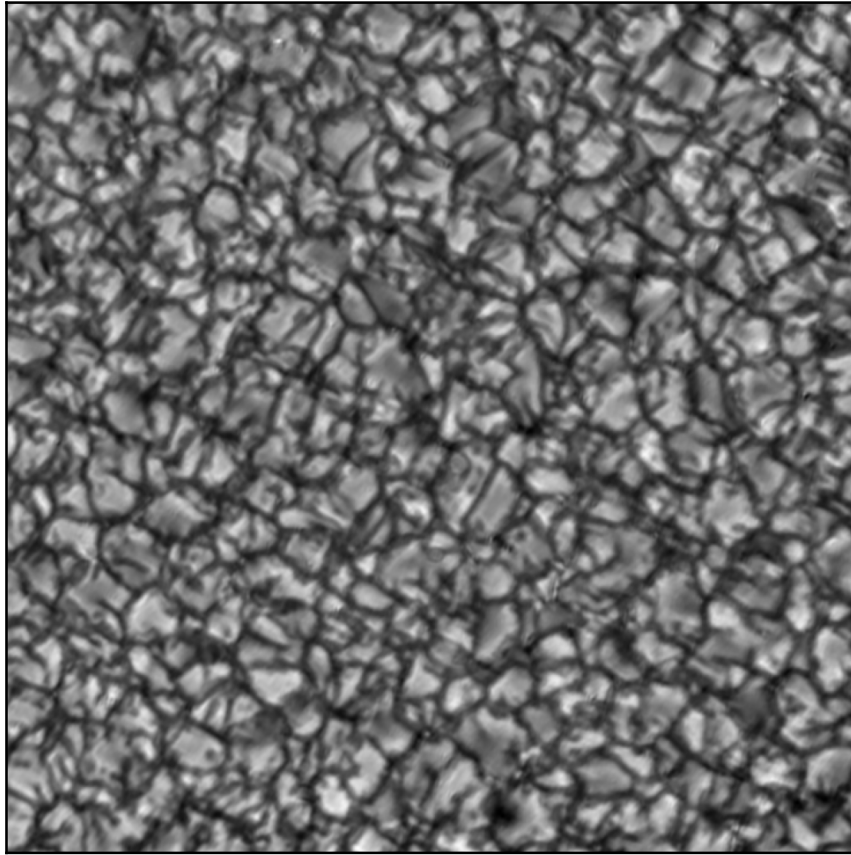
Figure 1.1. The granules and intergranular lanes observed with the Sunrise/IMaX instrument (Martínez Pillet et al. 2011). Bright features are the centres of convective cells that transport hot plasma to the surface. Dark regions are intergranular lanes where cold plasma returns to the convective zone.

of the local plasma is altered, allowing the radiation to escape from deeper layers. Since the radiation is emitted from deeper layers, which are hotter than the surface layers, these magnetic concentrations are observed as bright regions in the cool intergranular lanes. Owing to their nature, they are named magnetic bright points and are used as tracers of kG magnetic fields (e.g., Sánchez Almeida et al. 2010).

Larger concentrations of a strong magnetic field can entirely hinder the plasma convection, which results in sunspot formation (Borrero & Ichimoto 2011). Sunspots are large dark patches observed on the solar surface with two distinct regions: a central dark part called the umbra and a brighter part surrounding it named penumbra (Fig. 1.2). The sunspot magnetic field is predominantly vertical in the umbra and transits into a horizontal field in the penumbra. The characteristic photospheric magnetic field strength in the umbra is $2-3\,$kG (Solanki 2003), while Castellanos Durán et al. (2020) found a magnetic field strength up to $8.2\,$kG in a sunspot light bridge.

The penumbra is characterised by interchanging bright (intraspines) and dark (spines) filaments that are oriented radially from the sunspot's umbra (Lites et al. 1993) having a magnetic field strength that is a few times weaker than the maximum umbral one. Siu-

Tapia et al. (2017, 2019) found that the penumbral magnetic field can reach very high strengths, above 7 kG, in regions characterised with supersonic down-flows, which were later confirmed by Castellanos Durán et al. (2023). The intraspines are characterised by a more horizontal magnetic field than the magnetic field in spines, which are seen as umbral extensions into the penumbra. The regions in the photosphere occupied by a sunspot or group of sunspots are called active regions.
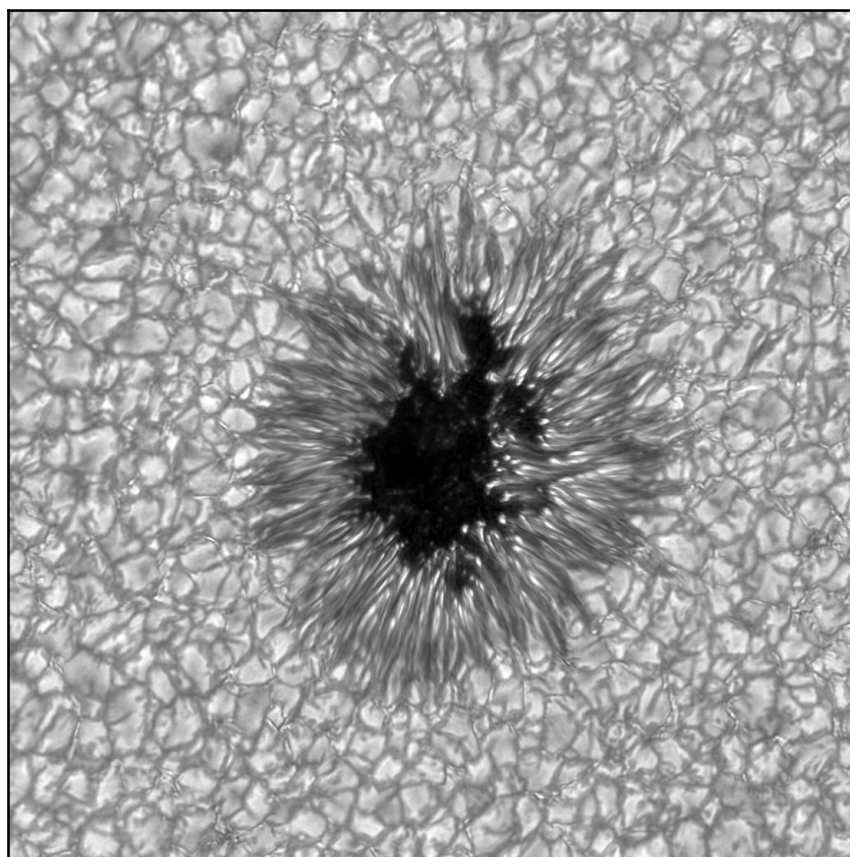
Figure 1.2. A sunspot observed in the G-band with the GREGOR/HiFi+ instrument (Denker et al. 2023). The dark central part of the sunspot is called the umbra, while the brighter fibril structure surrounding the umbra is called the penumbra (Image courtesy of Juan Sebastián Castellanos Durán).

The low brightness of the umbra indicates that it is cooler than the quiet-sun region. Observed spectra of umbrae show molecular spectral lines (e.g. CN, FeH, TiO; Sotirovski 1971), which form only in low-temperature layers in the atmosphere. These indicators constrain the umbra temperature in the photosphere to around $3000 - 4500$ K (e.g., Westendorp Plaza et al. 2001). Meanwhile, the penumbral structure is characterised by a brightness variation due to spines and intraspines. The average brightness of intraspines is comparable to the brightness of a quiet-sun region (see Fig. 1.2), indicating that they have a similar temperature (see for example Fig. 3 from Siu-Tapia et al. 2017).

The mass density of the solar atmosphere in the quiet-sun region drops with height (Fig. 1.3), causing the atmosphere to be more transparent (less radiation is absorbed) to

radiation emitted from the base of the photosphere. The emitted radiation thus carries energy out of the atmosphere, which causes a drop in the temperature in the photosphere (Fig. 1.3). At a height of around 500 km above the surface, the temperature in the quiet-sun region reaches its minimum of about 4200 K (Vernazza et al. 1981). In layers above, the temperature increases, reaching values of 10 000 K, after which the temperature suddenly jumps to 1 million K. The solar chromosphere is the layer in the solar atmosphere between the temperature minimum and the sudden temperature increase.
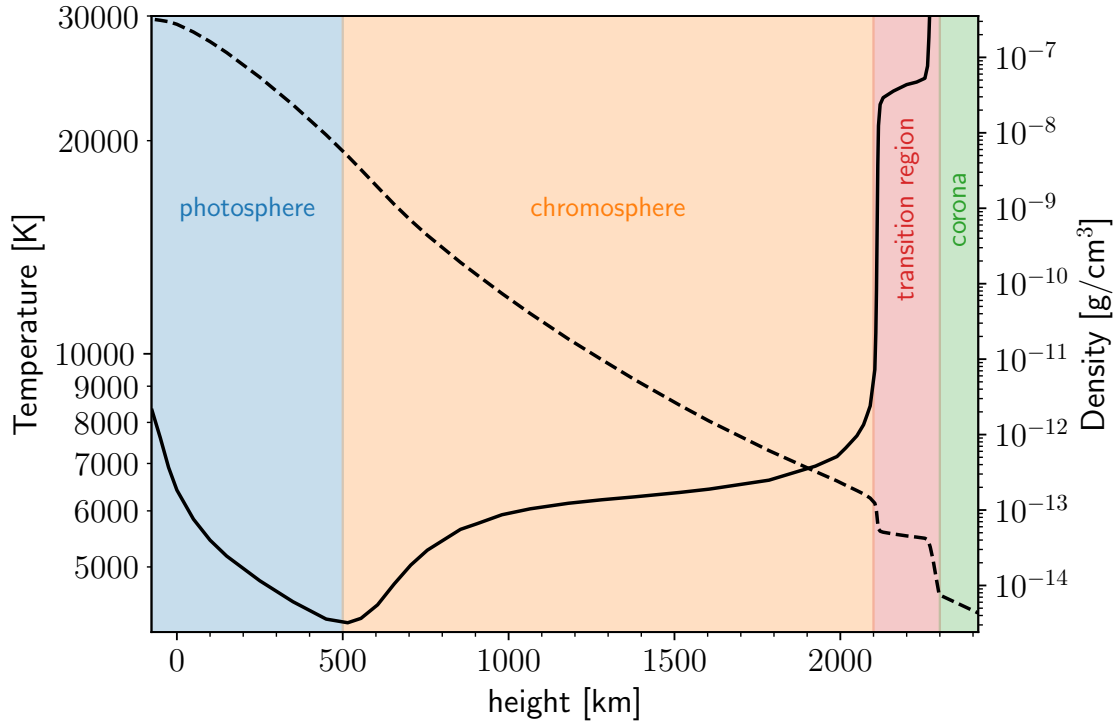
Figure 1.3. Temperature (full line) and density (dashed line) profiles with height in the 1D atmospheric model of the quiet Sun from Vernazza et al. (1981).

The chromospheric brightness in the continuum is insignificant compared to the photospheric brightness because of the much lower density. The chromosphere is either observed during a total solar eclipse as a thin bright halo surrounding the solar disc or in narrowband filters (filtergram observations) of spectral lines, such as Hα, Ca II H&K, Ca II infrared triplet, Mg II h&k. Observations in these lines demonstrate that the chromosphere is a dynamic and feature-rich region.

Observations in the Hα line show fibril-like structures (Fig. 1.4) that can sometimes be explained as hot plasma being trapped by the chromospheric magnetic field (e.g., de la Cruz Rodríguez & Socas-Navarro 2011). Filtergram observations of the chromosphere in the core of the strong Ca II H&K lines also reveal bright regions (Fig. 1.5) of two kinds: bright patches called plages that are associated with small magnetic filed concentrations in the photosphere and network-like structures above quiet-sun regions. The chromospheric bright network outlines what is known as a supergranular cell, which is characterised by a large-scale horizontal motion of photospheric plasma (Leighton et al. 1962), having a typical size of 30 Mm, encompassing tens of granules. This large-scale horizontal mo-

tion of photospheric plasma carries the magnetic field into the supergranular boundaries, increasing the magnetic energy. Following a decrease of the atmospheric mass density with height in the chromosphere, the horizontal pressure balance between the interior and the exterior of the magnetic concentrations is disrupted in regions between supergranules. The magnetic field strength must decrease with height to preserve this pressure balance, causing the field lines to funnel out. The funnelling of the magnetic field thus conserves the magnetic flux with height. This funnelling is observed as a wide bright region in the chromosphere, which traps hot chromospheric plasma because the plasma β parameter is below unity.
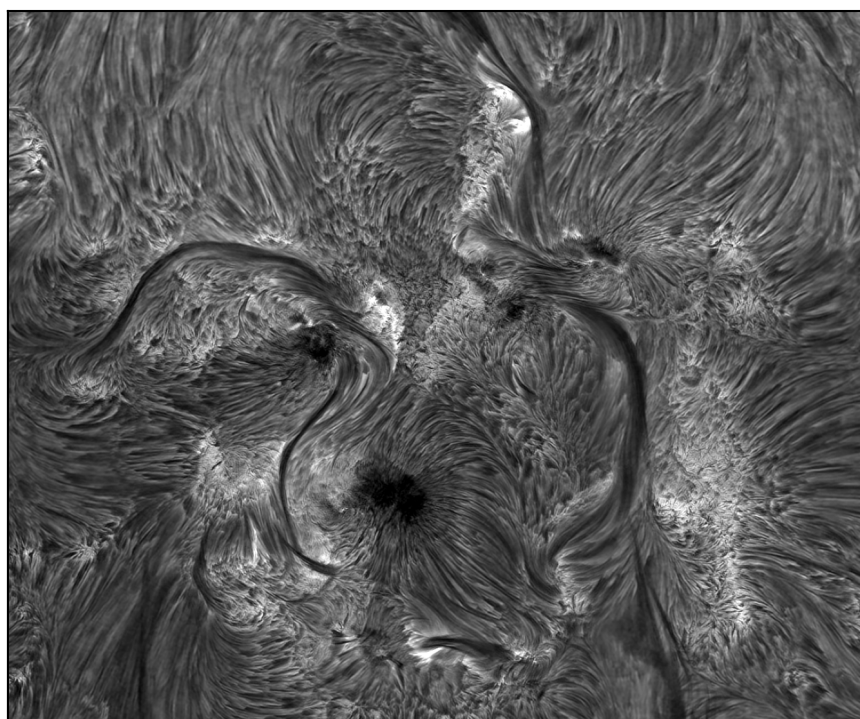
Figure 1.4. Chromospheric fibrils observed in the core of Hα line with the Dutch Open Telescope (Hammerschlag & Bettonvil 1998).

The narrow region in the solar atmosphere where the temperature and density change abruptly is called the transition region (Fig. 1.3). Due to high temperature reaching millions of degrees, the transition region is observed in lines from higher ionisation stages of elements, such as oxygen, silicon, and carbon.

The corona is the hottest region of the solar atmosphere, located above the transition region and reaching temperatures of a few million degrees. The corona is observed either during a total solar eclipse as a large bright halo that surrounds the occulted Sun, using instruments called coronagraphs that have a central obscuration mimicking a solar eclipse, or in X-ray or ultraviolet lies of highly ionized elements, such as Si VIII, Mg X, Fe XV. These spectral lines are observed in the corona due to the high energy necessary for their ionisation, supplied by the high coronal temperature. Additionally, radio observations in the frequency range of $10 - 90$ MHz are also used to study the solar corona (e.g., Vocks et al. 2018).
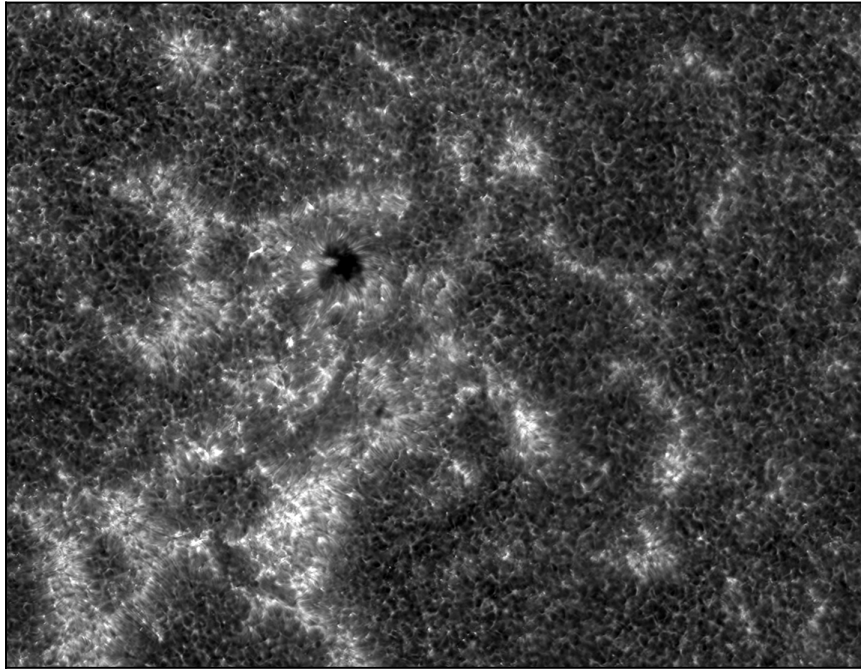
Figure 1.5. The chromospheric network and plage regions around a sunspot observed in Ca II H line with the Dutch Open Telescope (Hammerschlag & Bettonvil 1998).

Modelling the solar interior indicates that the temperature decreases towards the solar surface (Christensen-Dalsgaard et al. 1996), and this continues in the solar atmosphere until it reaches the temperature minimum (see Fig. 1.3). The temperature increase from the temperature minimum to the outer layers of the solar atmosphere is an exciting and puzzling problem to solve. The magnetic field is considered a mediator, rooted in the convective zone and extending into the corona. It can transport energy between atmospheric layers and increase the temperature in the outer layers by the dissipation of the transported energy. The probable causes for heating the solar atmosphere are either the dissipation of magneto-acoustic waves, the reconnection of magnetic field lines, or the Ohmic dissipation in the presence of a strong magnetic field gradient. The heating of the solar atmosphere is one of the reasons why many solar physicists are interested in understanding the origin of magnetic fields and their structure from the photosphere to the corona.

1.2   Radiative transfer theory

Radiation that passes through the solar atmosphere and arrives at the observer is modelled as an electromagnetic wave. It is described as an oscillation of electric and magnetic fields that are mutually perpendicular to the propagation direction of the radiation. Because of this characteristic, the wave behaviour of an electromagnetic wave can be fully described by considering only the electric field component. The specific intensity of an electromagnetic wave that falls on a detector averaged over some time interval is $I \propto \langle E_0^2 \rangle$, where E_0 is the amplitude of the electric field of a wave.

It is necessary to consider all possible interactions between electromagnetic waves and particles within stellar atmospheres to understand and analyse observed spectra of stars. In general, the spectrum is composed of a continuum upon which spectral lines are superimposed. Frequent particle collisions between the absorption and emission of radiation establish the thermodynamic equilibrium distribution of the radiation field over wavelengths represented by the Planck distribution. This picture is valid only in the stellar interiors where the radiation cannot escape freely and in the deepest layer of stellar atmospheres (photosphere). An observed stellar continuum is closely described by the Planck distribution, indicating that the radiation in the continuum is emitted from a high-density layer where collisions are frequent enough. On the contrary, absorption lines observed in stellar spectra indicate that the radiation field in the higher atmospheric layers deviates from the Planck distribution. The radiative transfer theory models the radiation field transport through the stellar atmosphere (or other absorbing and emitting media).

This section is based on the radiative transfer textbooks by Stenflo (1994), del Toro Iniesta (2003), Rutten (2003), Landi Degl'Innocenti & Landolfi (2004), Gray (2008), Hubeny & Mihalas (2014). The interested reader is encouraged to consult these textbooks for more in-depth descriptions. The following section will focus on the non-polarised radiation of specific intensity I and its interaction with atmospheric particles. In the subsequent subsections, the transfer of polarised radiation will be introduced along with the formation of spectral lines in magnetised atmospheres.

1.2.1 Radiative transfer equation (non-polarised case)

The specific intensity I is a function of the position in the atmosphere, $\mathbf{r}$, the direction of propagation, $\mathbf{l}$, the wavelength, λ, and time, t. The radiative transfer equation describes the energy exchange between radiation and particles during their interactions, conserving the total energy of the system (radiation energy plus particle energy).

Let us consider a parcel of plasma containing different particles (atoms, ions, electrons). The change of the incoming intensity along a ray, $\mathrm{d}I_\lambda(\mathbf{r}, \mathbf{l}, t)$, is equal to the difference between the intensity emitted by the parcel in the direction $\mathbf{l}$ and the amount of incoming intensity removed from the ray in the same direction. Assuming that the parcel of plasma has a thickness $\mathrm{d}s$ along the direction $\mathbf{l}$, the radiative transfer equation is:

$$\frac{\mathrm{d}I_\lambda(\mathbf{r}, \mathbf{l}, t)}{\mathrm{d}s} = \eta_\lambda(\mathbf{r}, \mathbf{l}, t) - \chi_\lambda(\mathbf{r}, \mathbf{l}, t) \cdot I_\lambda(\mathbf{r}, \mathbf{l}, t), \tag{1.1}$$

where $I_\lambda(\mathbf{r}, \mathbf{l}, t)$ is the incoming intensity, and $\eta_\lambda(\mathbf{r}, \mathbf{l}, t)$ and $\chi_\lambda(\mathbf{r}, \mathbf{l}, t)$ are the emission and extinction coefficients per unit length, respectively. The extinction coefficient takes into account the reduction in the intensity by the absorption and scattering processes (see Sec 1.2.2.1 for more details). Throughout the thesis, we will refer to $\chi_\lambda(\mathbf{r}, \mathbf{l}, t)$ simply as the absorption coefficient since we will not deal with the radiation scattering here.

Eq. (1.1) is general and can be applied to any geometry of interest. However, the usual approach in the study of radiative transfer in stellar atmospheres is to adopt the Cartesian coordinate system[1] in which the radiative transfer equation is:

---

[1]A spherical coordinate system is more appropriate for giant stars with extended atmospheres.

$$\frac{1}{c}\frac{\partial I_\lambda(\mathbf{r},\mathbf{l},t)}{\partial t} + \sin\theta\cos\Phi\frac{\partial I_\lambda(\mathbf{r},\mathbf{l},t)}{\partial x} + \sin\theta\sin\Phi\frac{\partial I_\lambda(\mathbf{r},\mathbf{l},t)}{\partial y} + \cos\theta\frac{I_\lambda(\mathbf{r},\mathbf{l},t)}{\partial z} \quad (1.2)$$
$$= \eta_\lambda(\mathbf{r},\mathbf{l},t) - \chi_\lambda(\mathbf{r},\mathbf{l},t)\cdot I_\lambda(\mathbf{r},\mathbf{l},t),$$

where θ is the polar angle with respect to the vertical direction z directed towards an observer, and Φ is the azimuthal angle in the xy plane in respect to the x axis.

For simplicity, we will assume that the specific intensity is time-independent, $\frac{\partial I_\lambda}{\partial t} = 0$. This assumption originates from the fact that the radiation propagates instantly from one side of an atmosphere to the other[2]. Leenaarts et al. (2012) showed that we have to solve a time-independent Eq. (1.2) to model chromospheric fibrils observed in the Hα line properly.

Further simplification in the radiative transfer equation is achieved by disregarding the horizontal transfer of radiation, $\frac{\partial I_\lambda}{\partial x} = \frac{\partial I_\lambda}{\partial y} = 0$ (azimuthal symmetry). This leaves only the change in the intensity along the vertical direction z and along angle θ. All these assumptions simplify the radiative transfer equation to:

$$\mu \cdot \frac{\mathrm{d}I_\lambda(z,\mu)}{\mathrm{d}z} = \eta_\lambda(z,\mu) - \chi_\lambda(z,\mu)\cdot I_\lambda(z,\mu), \quad (1.3)$$

where $\mu = \cos(\theta)$. Another form of the radiative transfer equation often used in practice is derived after dividing Eq. (1.3) by the negative absorption coefficient, which yields:

$$\mu \cdot \frac{\mathrm{d}I_\lambda(\tau,\mu)}{\mathrm{d}\tau} = I_\lambda(\tau,\mu) - S_\lambda(\tau,\mu), \quad (1.4)$$

where we introduce two new variables: optical depth τ_λ and the source function S_λ.

The optical depth measures the transparency of an atmosphere at wavelength λ where $\mathrm{d}\tau_\lambda = -\chi_\lambda \cdot \mathrm{d}z$. The outer boundary of an atmosphere is at an observer, for which $\tau = 0$[3]. The optical depth scale increases inwards into the atmosphere where $\tau_\lambda = \int_{z_1}^{z_2}\chi_\lambda\mathrm{d}z$ represents the number of interactions a photon with wavelength λ experiences on its path from z_2 to z_1, assuming that $\tau_\lambda = 0$ at z_1. The medium is said to be optically thick if $\tau_\lambda > 1$, while it is optically thin for $\tau_\lambda < 1$. A medium can be optically thick and thin at the same time, depending on the wavelength at which we observe it.

The source function is defined as the ratio of the emission to the absorption coefficient, $S_\lambda = \eta_\lambda/\chi_\lambda$, and it can be interpreted as a measure of emission per optical depth.

Assuming that the source function is known, Eq. (1.4) is solved to obtain the outgoing intensity for any direction $\mu > 0$, which is known as the formal solution:

$$I_\lambda(\tau_1,\mu) = I_\lambda(\tau_2,\mu)\cdot e^{-(\tau_2-\tau_1)/\mu} + \int_{\tau_1}^{\tau_2} S_\lambda(t_\lambda)\cdot e^{-(t_\lambda-\tau_1)/\mu}\frac{\mathrm{d}t_\lambda}{\mu}, \quad (1.5)$$

where $\tau_1 < \tau_2$. The first term represents the attenuation of the incoming intensity, $I_\lambda(\tau_2,\mu)$, at the lower boundary, τ_2, on the passage through the slab of optical thickness

---

[2]If we would travel with the speed of light, it would take us around 7 ms to escape from the atmosphere.

[3]In practice, we limit the outer boundary of an atmosphere to be at, e.g., $\log\tau = -6$. The choice of this value depends on the wavelength region and spectral lines we are modelling.

$\tau_2 - \tau_1$, while the second term represents the addition of intensity into the direction μ by the slab.

The stellar atmosphere is commonly treated as a semi-infinite medium with the deepest layer at $\tau_2 = \infty$[4] and the outer boundary at $\tau_1 = 0$. The incident intensity at the outer boundary in the semi-infinite model is assumed to be $I_\lambda(\tau_1 = 0, \mu) = 0$, while at the inner boundary, we impose that:

$$\lim_{\tau_2 \to \infty} I_\lambda(\tau_2, \mu) \cdot e^{-\tau_2/\mu} = 0. \tag{1.6}$$

This boundary condition assures that the solution of the radiative transfer equation does not depend on the intensity coming at the lower boundary of the atmosphere. In the numerical solution to the radiative transfer equation, the intensity at the lower boundary takes the value of the source function and its gradient (diffusion limit). The boundary conditions for a semi-infinite atmosphere simplify the formal solution of the radiative transfer equation to:

$$I_\lambda(0, \mu) = \int_0^\infty S_\lambda(t_\lambda) \cdot e^{-t_\lambda/\mu} \frac{dt_\lambda}{\mu}. \tag{1.7}$$

If the source function changes linearly with the optical depth, we can easily solve the integral in Eq. (1.7). This solution is known as the Eddington-Barbie solution, which is:

$$I_\lambda(0, \mu) = S(\tau_\lambda = \mu). \tag{1.8}$$

The intensity emitted at the disc centre, $\mu = 1$, equals the source function at the depth $\tau_\lambda = 1$. The optical depth at $5000\,\text{Å}$, τ_{5000}, is regularly used for atmospheric models as a reference depth scale. The depth in an atmosphere at which $\tau_{5000} = 1$ is generally considered to be the surface of the Sun. Therefore, radiation at wavelength λ is said to be emitted from the atmospheric height at which $\tau_\lambda = 1$.

The linear change of the source function is an approximation of an actual source function. We must compute the emission and absorption coefficients throughout the atmosphere to compute the source function. Once it is known, solving the radiative transfer equation is straightforward. The following subsections describe the calculation of the emission and absorption coefficients.

1.2.2   The emission and absorption coefficients

Interactions between radiation and particles define the magnitude of the intensity removed from and added to the radiation beam in a given direction. These interactions are separated into two types: continuum and line processes. This allows us to separate the contributions of the continuum and lines to the emission and absorption coefficients as $\eta_\lambda = \eta_\lambda^C + \eta_\lambda^L$ and $\chi_\lambda = \chi_\lambda^C + \chi_\lambda^L$, respectively. If we are modelling many spectral lines simultaneously, the line contribution assumes a summation over all lines that overlap for a given λ. The same also holds for all processes that contribute to the emission and absorption in the continuum.

The interactions between particles and the radiation field produce a change in the energy state of an electron. The electron being subjected to the interaction can be found

---

[4]In practice the bottom boundary is located around $\tau = 10 - 50$. Already at this depth, the radiation field is strongly coupled with the plasma and can be safely assumed to follow the Planck function.

in a bound state in an atom or as a free particle. The interactions that contribute to the continuum involve a change of an electron from a bound to a free state (and opposite) or the change between two free states. Therefore, these interactions are known as bound-free and free-free processes. Spectral lines form in an electron transition between two bound states in an atom (bound-bound processes). Thus, the continuum level is set by the bound-free and free-free processes because the energy of a free electron is unbounded. On the other hand, spectral lines are always due to bound-bound processes.

The bound-free, free-free and bound-bound processes responsible for forming a continuum and spectral lines can be of two kinds: the radiative processes caused by the radiation field and the collisional processes caused by the collisions between particles in a stellar atmosphere. In quantum mechanics, the electromagnetic wave (radiation) has a dual nature where it can be treated as a wave and as a particle (photon). In the upcoming description of radiative processes, we will treat the radiation field as an ensemble of photons with some distribution over energies.

Photon absorption is a radiative process in which a photon's energy is converted into an electron's energy (bound or free). In the case of a bound electron, if the energy of the absorbed photon is higher than the binding energy of the electron, the excess energy is converted into the kinetic energy of the free electron and an atom is ionised. Recombination occurs when an ion captures a free electron. This process causes the emission of a photon with an energy equal to the difference between the total energy of the free electron and the energy of the electron's bound state (photon-recombination process). The photon is also emitted when the bound electron de-excites from a higher energy state (radiative de-excitation process). The photon absorption and emission processes are responsible for the coupling and energy exchange between the radiation field and particles.

The primary sources of continuum absorption in the solar atmosphere from the ultraviolet to the infrared are bound-free and free-free processes of neutral hydrogen atoms and H^- ions. The H^- ion is a neutral hydrogen atom that captures a free electron removed from metals (i.e., elements heavier than helium) in bound-free processes. These H^- ions form mostly in stars that are hot enough to ionize metals but cool enough that electrons can be captured by the neutral hydrogen atoms (i.e., G and F dwarf stars; Gray 2008). The contribution of the bound-free processes of various metals to the continuum absorption coefficient must be considered at the ultraviolet wavelengths.

Since the continuum forms deep in the atmosphere where collisions are frequent, we can safely assume that the source function in the continuum is Planck's distribution in the visible and infrared regions. Knowing the absorption coefficients for each process allows us to calculate the respective emission coefficients.

1.2.2.1   Formation of spectral lines

Let us consider a group of atoms in an ionisation state k with many discrete energy levels. A bound electron can be in a lower, l, or upper, u, state due to radiative interactions or inelastic collisions of an atom with other particles (Fig. 1.6). A bounded electron is excited from l to u by absorption of a photon (radiative excitation; Fig. 1.6 A) or in an atom's collision with a particle (collisional excitation; Fig. 1.6 D). Excited electron decay into the lower state l in radiative de-excitation by the spontaneous emission of a photon (Fig. 1.6 B) or in a collisional de-excitation process (Fig. 1.6 E). Another radiative process
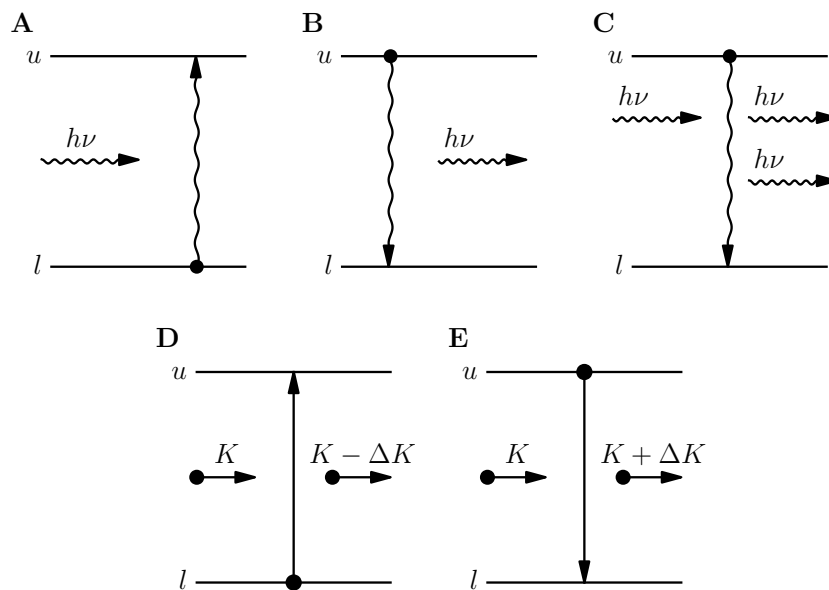
Figure 1.6. Radiative and collisional bound-bound transitions: radiative excitation (panel A), radiative de-excitation (panel B), stimulated emission (panel C), collisional excitation (panel D) and collisional de-excitation (panel E). The colliding particle's kinetic energy K changes by ΔK corresponding to $h\nu = E_u - E_l$, where h is the Plank constant. Wavy vertical lines indicate radiative transitions, while solid vertical lines represent collisional transitions.

that can de-excite an electron is stimulated emission: an excited electron is stimulated to decay into a lower level by a photon with an energy that matches the energy difference between the lower and the upper level (Fig. 1.6 C). This photon acts as a mediator that stimulates an atom to de-excite an electron to a lower state, thus emitting a new photon. The emitted photon has the same properties as the incident one, which stimulated the emission. In radiative transfer theory, the stimulated emission is usually treated as a negative absorption.

In the interaction of photons with atoms, we discern two mechanisms:

Thermal[5] absorption: a radiative excitation followed by collisional de-excitation. In this series of processes, a photon's energy is first converted into the internal energy of an atom (electron excitation), which is further converted into the kinetic energy of a colliding particle during collisional de-excitation.

Thermal emission: an electron is excited during a collision with another particle (collisional excitation), increasing atoms internal energy. The excited electron spontaneously decays to a lower state (radiative emission), converting this excess energy into a photon and thus increasing the energy of a radiation field. Similarly, the de-excitation of the electron can occur also in the stimulated emission process.

These mechanisms transfer energy from a radiation field to particles in the surrounding medium (thermal absorption) and vice versa (thermal emission).

---

[5]In some literature it is named as *true* or *pure* absorption and emission.

The photons can be removed from a radiation beam in a given direction **l** by photon absorption or by photon scattering. During the photon scattering process, a photon absorption at a wavelength λ from a direction **l** is followed by a photon emission in direction **l′** with a wavelength λ'. The scattering effectively decreases photon density in the direction **l**, but at the same time, it increases it in the direction **l′**. Since collisional processes are not involved, there is no energy exchange between particles and the radiation field in the scattering process.

The absorption coefficient in a spectral line χ^L, is proportional to the energy of the absorbed photon, $h\nu_{l,u}$, the number density of the atom in an ionisation state k whose electron is in a lower energy level l, $n_{l,k}$, and the probability of the photon's absorption $B_{l,u}$ (the Einstein coefficient for the photon absorption):

$$\chi^L = \frac{h\nu_{l,u}}{4\pi} \cdot \left(n_{l,k}B_{l,u} - n_{u,k}B_{u,l}\right).$$

(1.9)

The contribution of stimulated emission is added as a negative factor where $n_{u,k}$ is the number density of the atom in the same ionisation state k whose electron is in the upper energy level u, and $B_{u,l}$ is the Einstein coefficient for the stimulated emission. We treat the stimulated emission and absorption processes simultaneously because both affect the incoming intensity in the same way. The negative sign in front of the stimulated emission factor appears because it reduces the number of atoms available for the photon absorption process.

The line emission coefficient is:

$$\eta^L = \frac{h\nu_{l,u}}{4\pi} \cdot n_{u,k} \cdot A_{u,l},$$

(1.10)

where $A_{u,l}$ is the probability for the spontaneous emission (the Einstein coefficient for spontaneous emission).

The Einstein coefficients are intrinsic characteristics of each transition that can occur between two energy levels in an atom and are mutually dependent. The relations between the Einstein coefficients can be derived under the assumption of a detailed balance: the energy absorbed by the parcel of plasma, E_{abs}, equals the energy emitted by the same parcel, E_{em}. Additionally, we assume that the collisions between particles are frequent enough to establish the thermodynamic equilibrium in which the radiation field is described by the Planck function:

$$B_\nu(T) = \frac{2h\nu^3}{c^2} \cdot \frac{1}{e^{\frac{h\nu}{kT}} - 1}.$$

(1.11)

The absorbed energy by a parcel of plasma is $\chi^L \cdot B_\nu(T)$, while the emitted energy is η^L. From the detailed balance between the absorption and emission, we have:

$$\frac{h\nu_{u,l}}{4\pi} \cdot \left(n_{l,k}B_{l,u} - n_{u,k}B_{u,l}\right) \cdot B_\nu(T) = \frac{h\nu_{u,l}}{4\pi} \cdot n_{u,k}A_{u,l},$$

$$B_\nu(T) = \frac{n_{u,k}A_{u,l}}{n_{l,k}B_{l,u} - n_{u,k}B_{u,l}},$$

$$B_\nu(T) = \frac{A_{u,l}/B_{u,l}}{\frac{n_{l,k}B_{l,u}}{n_{u,k}B_{u,l}} - 1}.$$

(1.12)

The Boltzmann distribution gives the ratio of level populations in the thermodynamic equilibrium (see the following subsection for more details) as $n_{l,k}/n_{u,k} = g_l/g_u \cdot e^{-\frac{E_l-E_u}{k_B T}}$, where g_l and g_u represent the statistical weights of energy levels l and u that define the maximum occupancy of an energy level. Rewriting the difference of energy levels as $h\nu_{l,u} = E_u - E_l$, we have from Eq. (1.12):

$$B_\nu(T) = \frac{A_{u,l}/B_{u,l}}{\frac{B_{l,u}}{B_{u,l}}\frac{g_l}{g_u}e^{\frac{h\nu_{l,u}}{k_B T}} - 1}. \tag{1.13}$$

Connecting the terms from Eq. (1.13) with the Planck function in Eq. (1.11), we obtain the following relations between the Einstein coefficients:

$$B_{u,l} = \frac{c^2}{2h\nu_{l,u}^3}A_{u,l},$$
$$B_{l,u}g_l = B_{u,l}g_u. \tag{1.14}$$

The same relations also hold when an atmosphere is outside the thermodynamic equilibrium. The relations between the Einstein coefficients are correctly derived using quantum mechanics without any prior assumptions about the medium. Thus, when knowing one of the Einstein coefficients (usually $A_{u,l}$), the rest can be calculated from Eq. (1.14). $A_{u,l}$ is estimated in experimental measurements, from theoretical computations or from observed spectral lines (more on estimating the $A_{u,l}$ is given in Sec. 1.3.1).

1.2.2.2 Level populations

Assuming that the Einstein coefficients are known, the only missing ingredient for computing the absorption and emission coefficients is the number density of atoms in states corresponding to the energy levels (level populations) between which transitions occur. The frequent collisions between particles in dense environments, such as the stellar interior and the photospheric layers, are responsible for establishing the equilibrium distributions of particle velocities (Maxwell's distribution) and the excitation and ionisation distributions of particles (Boltzmann and Saha distributions). In these dense layers where collisions are frequent, the photon mean free path is small compared to the typical scale of temperature change. Photons carry information only between particles sensing the same plasma conditions, allowing us to assume the thermal equilibrium locally in the atmosphere. This approximation is known as local thermodynamic equilibrium (LTE). In LTE, particles can be considered to be in equilibrium only locally, and because of Kirchhoff's law, the source function in LTE is the Planck function. Meanwhile, the radiation field is not in equilibrium and is determined by solving the radiative transfer equation, which is significantly simplified in the LTE approximation. However, the absorption coefficient is still needed to compute the optical depth at each wavelength.

Considering an ensemble of particles with distinct internal energy levels E_l, the number density of atoms in ionisation state k whose outermost electron is excited to a given level l is described by the Boltzmann distribution:

$$n_{l,k} = n_k \frac{g_l}{U_k(T)}e^{-\frac{E_l}{k_B T}}, \tag{1.15}$$

where n_k is the total number density of an atom in an ionisation state k, $U_k(T)$ is known as the partition function[6] of an atom in ionisation state k, T is the temperature of the medium and k_B is the Boltzmann constant.

Eq. (1.15) shows that the number density of a level population drops exponentially with increasing level's energy. This suggests that the stimulated emission factor (in some literature also referred to as the Boltzmann factor), $e^{-(E_u - E_l)/\lambda k_B T}$, in Eq. (1.9) has an insignificant impact on the opacity in spectral lines in ultraviolet and visible wavelengths. However, the contribution from stimulated emission must be considered for infrared spectral lines. This conclusion follows from the atomic energy structure: very few low-lying and many high excitation energy levels between which infrared lines form.

The ratio of the atom's total number density in two consecutive ionisation stages $k + 1$ and k is described by the Saha distribution:

$$\frac{n_{k+1}}{n_k} = \frac{2}{n_e} \cdot \frac{U_{k+1}(T)}{U_k(T)} \cdot \frac{(\pi m_e k_B T)^{3/2}}{h^3} \cdot e^{-\frac{E_{\text{ion}}}{k_B T}}, \tag{1.16}$$

where n_e is the number density of free electrons in the medium, m_e is the electron mass and E_{ion} is the ionisation energy from state k to $k + 1$.

Using the Boltzmann and Saha distributions, assuming that the chemical composition, temperature and density of an atmosphere are known, we can calculate the number density of levels in every atom in any ionisation state at each depth in an atmosphere. These number densities are then used to compute the line absorption and emission coefficients from Eq. (1.9) and Eq. (1.10), respectively, and allow us to solve the radiative transfer equation.

Collisions between particles are less frequent in less dense layers, and radiative processes start to play a significant role in populating and de-populating atomic levels. As the density in the solar atmosphere decreases with height, the LTE approximation breaks down, and this case is known as non-LTE. The number density of levels in non-LTE is calculated from the statistical equilibrium equation, which is solved iteratively with the radiative transfer equation. The statistical equilibrium equation assumes a net-zero change of the number density of a level population in time and an equilibrium between collisional and radiative processes that populate and depopulate an atomic level. Proper modelling of a spectral line in non-LTE requires a solution of the statistical equilibrium equation for all atomic levels in an atomic model.

1.2.2.3 Broadening of spectral lines

The previous description of line formation assumed that the spectral line is formed only at a specific wavelength λ corresponding to the difference in energy levels, which implies that the line profiles have the shape of a δ function. However, observed spectra exhibit spectral lines that are not sharp but have some width. This so-called broadening of spectral lines is caused by the uncertainties in the energy of atomic levels (natural broadening),

---

[6]The partition function is given as $U_k(T) = \sum_l g_l \cdot e^{-E_l/k_B T}$, where the summation goes over all energy levels in an atom. It represents the total number of states a system can be found at a given temperature T. In general, it is complicated to calculate the partition function for atoms with a high atomic number. Many different approximations are imposed, and interpolation tables are created to compute the partition function for a desired temperature. The most recently compiled table of the partition functions for temperatures up to $10\,000\,\text{K}$ is given by Barklem & Collet (2016).

thermal motion of atoms (thermal broadening), particle collisions (pressure or collisional broadening), spatially unresolved plasma motions (micro- and macro-turbulent broadening) and the magnetic field (Zeeman broadening; more on this in Sec. 1.2.3.1). Additional broadening mechanisms of spectral lines, which are not discussed further, include isotopic and hyper-fine structure splitting.

Broadening of spectral lines also occurs due to macroscopic plasma flows, such as the one caused by convective plasma motion or by stellar rotation. These broadening mechanisms must be considered when we analyse the spatially averaged solar spectrum or stellar spectra, which are spatially integrated over the whole stellar surface.

Natural broadening. The atomic energy levels are not infinitely sharp but have some width (uncertainty), δE, that is determined by Heisenberg's uncertainty principle, which relates the uncertainty of an energy level δE to the lifetime of the level Δt. The ground state levels are characterised by an infinite lifetime, thus having an infinitely sharp energy level. The lifetime of an excited energy level u is the reciprocal sum of the Einstein coefficients for the spontaneous emission, $A_{u,l}$, from all possible transitions from the level u to levels $l < u$:

$$\Delta t_u = \frac{1}{\sum_{l<u} A_{ul}}. \tag{1.17}$$

The lifetime of excited energy levels is typically in the order of nanoseconds. An exception are the metastable levels whose lifetime can be measured even in seconds (very small probability for spontaneous de-excitation).

The natural broadening of levels allows the atom to absorb and emit photons whose energy does not correspond exactly to the energy difference between the upper and lower levels. Those transitions that occur farther from the nominal energy of the levels are much less probable (Fig. 1.7). Superimposing all these transitions broadens a line whose profile becomes a Lorentzian function. The width of this profile is determined by the width of the energy levels between which transition occurs (lifetime of levels, or $A_{u,l}$; see Fig. 1.7). On average, spectral lines have a natural width of a few picometers and require a very high-resolution spectrograph to be measured, which is only achievable for lines observed in laboratories.

Thermal broadening. The motion of particles in an atmosphere alters the photon's wavelength (Doppler effect), allowing atoms to absorb photons whose original energy did not correspond to the energy of a transition. Consequently, atoms absorb/emit photons in a broader range of energies, broadening a spectral line. The resultant line profile takes the shape of a Gaussian function, which follows from projecting the Maxwell distribution of particle velocity onto the line of sight. Since the temperature defines the velocity of particles, this broadening is known as thermal broadening, characterised by the thermal width of a spectral line given by:

$$\Delta \lambda_D = \frac{\lambda_0}{c} \sqrt{\frac{2k_B T}{m}},$$

where λ_0 is the central wavelength of a line, m is the mass of an atom of the considered species, and c is the speed of light. Thermal broadening is typically an order of magnitude larger than natural broadening, which is why it is considered a major source of broadening in spectral lines.
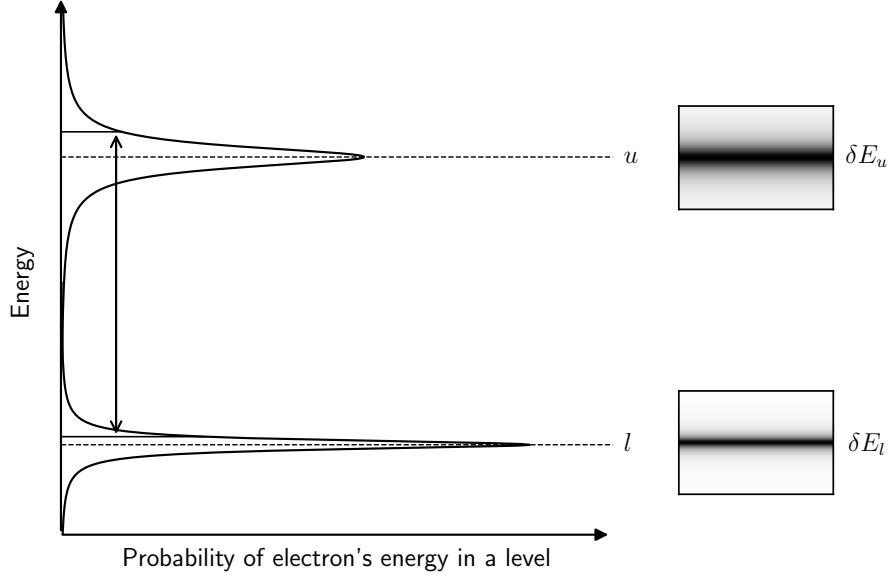
Figure 1.7. The natural broadening of energy levels due to Heisenberg's uncertainty principle. The energy of an atomic level follows a Lorentzian function. The level *l* has a larger lifetime, characterised by small δE_l, while the level *u* has a smaller lifetime and, therefore, larger δE_u.

Impact of the line of sight velocity. Similar to thermal broadening, plasma motion along the line of sight also alters the photon's energy, making it possible for atoms to absorb/emit photons whose energies did not match the energy of the transition. Contrary to thermal broadening, which only increases the line width, the line of sight velocity of plasma produces a wavelength shift of the line. When the line of sight velocity changes with height, the differential shift of the line at each depth in the atmosphere broadens the line and produces an asymmetric line profile. The asymmetries in the line profile can be very subtle (depending on the magnitude of the velocity) and are only apparent through the construction of line bisectors.

Micro-turbulent broadening. Further broadening of spectral lines in the solar atmosphere comes from turbulent motions of plasma that occur on scales smaller than the mean free path of a photon (~ 100 km). These motions are parameterized with the micro-turbulent velocity v_{mic}, and the broadening of spectral lines caused by it is known as micro-turbulent broadening. Averaging this motion of particles and projecting it along the line of sight contributes to the aforementioned thermal velocity of particles. Therefore, we include the v_{mic} as an additional term in the thermal Doppler width as:

$$\Delta \lambda_D = \frac{\lambda_0}{c} \sqrt{\frac{2 k_{\mathrm{B}} T}{m} + v_{\mathrm{mic}}^2}.$$

Micro-turbulent velocity is considered an atmospheric parameter, but it is introduced ad hoc to describe unresolved plasma motion along the line of sight. It reproduces the observed line width, which would otherwise be poorly represented when only the thermal and the line of sight velocity contributions are accounted for.

Macro-turbulent and instrumental broadening. Turbulent plasma motions on scales larger than the photon mean free path (but still smaller than the spatial scales resolved in observations) are parameterized with the macro-turbulent velocity v_{mac}. The broadening of a line caused by v_{mac} is known as the macro-turbulent broadening of spectral lines. The spectrum is convolved with a Gaussian function with width $\sigma = v_{mac}/c$. The macro-turbulent broadening preserves the equivalent width[7] of the line, thus increasing the line core intensity, the line becomes shallower and has broader wings.

The observed spectral lines undergo additional broadening caused by the spectrograph itself. This type of broadening is known as instrumental broadening, and it is characterised by the instrumental profile, which can be measured by recording the infinitesimally small light source. The recorded spectrum of an object is the convolution of the actual spectrum and the instrumental profile. Usually, the instrumental profile takes the shape of a Gaussian function of width $\sigma = 1/R$, where R is the spectrograph resolution. Even though instrumental broadening differs in nature from macro-turbulent broadening, their effect on the spectrum is the same, and in spectral modelling, they cannot be distinguished.

Collisional broadening. The energy levels in an atom are perturbed by Coulomb interaction with colliding particles, causing a shift of their energy levels E and their widths δE. This change in energy levels permits transitions that would otherwise not be possible. The broadening of a line caused by elastic collisions with other particles is described with Lorentzian. The main perturbers which cause collisional broadening are free electrons (Stark broadening) and hydrogen atoms (van der Waals broadening). Broadening caused by the hydrogen atoms is more important in the solar atmosphere owing to the large abundance of neutral hydrogen atoms. The contribution of hydrogen collisional broadening on the width of the spectral line is still often represented using the approach from Unsold (1955). This approach was later improved for lines of neutral elements by the theory developed in Anstee & O'Mara (1995), Barklem & O'Mara (1997), Barklem et al. (1998) (so-called ABO theory). This theory describes the hydrogen collisional broadening for s-p, p-d and d-f transitions. The ABO theory was later extended to spectral lines of ionised elements, which requires treatment on a line-to-line basis (Barklem & O'Mara 1998, 2000, Barklem & Aspelund-Johansson 2005).

The final profile $\phi(\lambda)$ of a spectral line accounts for all broadening mechanisms. The combined profile is a convolution of the Lorentzian and Gaussian functions known as the Voigt function. The Gaussian function dominates the core of the line profile, while the line has broad wings due to the Lorentzian part. The absorption and emission coefficients in Eq. (1.9) and Eq. (1.10) are thus multiplied by the Voigt function, $\phi(\lambda)$, which yields:

$$
\begin{aligned}
\chi_\lambda^L &= \frac{h\nu_{lu}}{4\pi} \cdot (n_{lk}B_{lu} - n_{uk}B_{ul}) \cdot \phi(\lambda), \\
\eta_\lambda^L &= \frac{h\nu_{lu}}{4\pi} \cdot n_{uk} \cdot A_{ul} \cdot \phi(\lambda).
\end{aligned}
\tag{1.18}
$$

In the previous equations, we added index λ to the coefficients to note their wavelength-dependence coming from the line profile $\phi(\lambda)$.

---

[7]The equivalent width, W, of the line is a measure of the line strength. It represents the line area between the continuum and the line profile, which is identical to a rectangle of width W and unit height.

Spectral line forms over a broad range of heights in an atmosphere because of the variations in the absorption coefficient with wavelength. This variation causes photons at different wavelengths in a line to decouple from an atmosphere at different heights, making spectral lines very useful as a diagnostic tool for inferring an atmosphere's thermodynamic and magnetic properties. The line's core has the largest opacity (highest probability of absorption) and is formed at a much higher layer in an atmosphere than the line wings. The height at which the photons at different wavelengths in a line decouple from an atmosphere is changed by altering the line absorption coefficient. We achieve this by altering either the level populations (excitation potential of a level, abundance, ionisation fraction) or the transition probability ($A_{u,l}$). Thus, the atmosphere at a central wavelength of some lines will be transparent enough, allowing photons to escape from the photospheric layers (photospheric/LTE lines). At the same time, it is very opaque for some, and photons escape from the chromospheric layers (chromospheric/non-LTE lines).

In Eq. (1.18), we assumed that the photon absorption, emission and stimulated emission processes have the same profile $\phi(\lambda)$. This assumption is valid for many spectral lines we observe in the solar spectrum. It is a consequence of the absorption and emission processes being completely independent, which happens when collisional processes dominate over scattering processes. This assumption is known as complete frequency redistribution, and it fails only for very strong lines, such as Mg II h&k, Ca II H&K, Lyα, formed in the chromosphere. Properly modelling these lines requires the partial frequency redistribution approach, in which the absorption and emission profiles are different (Hubeny & Mihalas 2014).

1.2.3   Radiative transfer of polarised light

Magnetic field permeating a stellar atmosphere establishes an anisotropy that produces a polarisation of radiation and affects its propagation differently in each direction. Analyses of the observed spectrum of the Sun require treatment of not only the intensity but also of the radiation's polarisation properties.

The oscillations of the electric field components define the polarisation state of an electromagnetic wave. Let us assume that a harmonic monochromatic plane wave propagates in the z direction and that the electric field oscillates in a plane perpendicular to it (xy plane). The electric field vector components decomposed onto the x and y axis, oscillate with the same frequency but are not necessarily in phase. A wave whose electric field components oscillate with a unique phase difference δ is said to be a polarised wave. A single harmonic monochromatic plane-parallel electromagnetic wave will always be completely polarised (has a constant δ).

A wave's most general polarisation state is an elliptically polarised wave, which occurs for $\delta \neq n\pi$, assuming that neither of the electric field components is zero and that they are not equal (Fig. 1.8). A special case of elliptical polarisation is a linearly polarised wave that takes place for $\delta = n\pi$ or when one of the electric field components vanishes. Another special case is a circularly polarised wave, which takes place for $\delta = n\pi/2$ when both electric field components have the same amplitude. Based on a phase difference δ, we discriminate between right ($\delta = \pi/2$) and left ($\delta = 3\pi/2$) handed circularly polarised waves. Fig. 1.8 summarizes different states of a wave's polarisation based on the phase difference δ and the amplitudes of the electric field components.
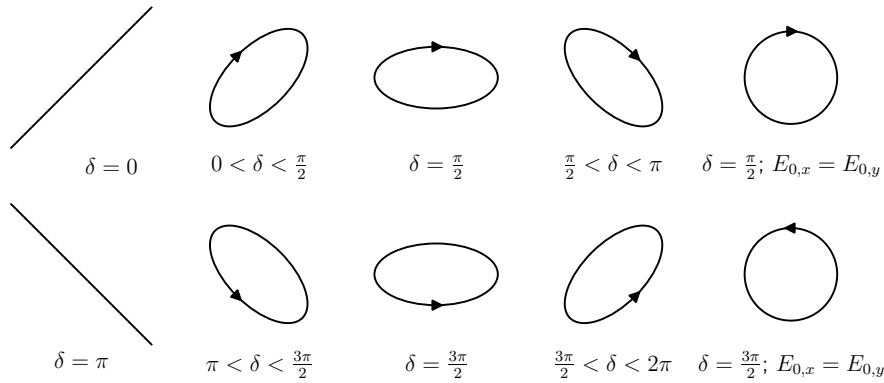
Figure 1.8. Different polarisation states of a plane-parallel monochromatic electromagnetic wave. Each panel depicts the motion of the electric field vector in a plane perpendicular to the direction of wave propagation when viewed from the observer's standpoint. δ is the phase difference between E_x and E_y components with respective amplitudes $E_{0,x}$ and $E_{0,y}$.

However, photometric detectors are sensitive to all electromagnetic waves that fall on them in some finite time interval, i.e., we are not detecting individual electromagnetic waves, but only wave packets. Each wave in this wave packet has an arbitrary phase difference δ, and the phase difference of each wave determines the polarisation state of a wave packet. Thus, the wave packet can have any degree of polarisation from completely polarised (all waves having the same δ) to the non-polarised state (each wave has an arbitrary δ). The measured wave packets have some degree of polarisation because they deviate from an ideal plane-parallel wave due to wave diffraction on the telescope entrance and reflections from optical elements inside the instrument.

There are multiple mathematical formalisms in which the polarisation can be described (e.g. Stenflo 1994, Born & Wolf 1999). The most used one in solar physics is the Stokes formalism, where the complete state of the radiation is described using the so-called Stokes vector $\mathbf{I}_\lambda = (I_\lambda, Q_\lambda, U_\lambda, V_\lambda)^{\mathrm{T}}$. Here, Q_λ and U_λ are a measure of nett linear polarisation, and V_λ is a measure of nett circular polarisation. Q_λ and U_λ differ from each other by a rotation of the plane of linear polarisation by $45°$. The amount of polarisation is quantified by the degree of polarisation p that is equal to the ratio of the total polarisation and the total intensity:

$$p = \frac{\sqrt{Q_\lambda^2 + U_\lambda^2 + V_\lambda^2}}{I_\lambda}. \tag{1.19}$$

The radiation is completely polarised for $p = 1$ while non-polarised for $p = 0$. Observed radiation is generally partially polarised, having $0 < p < 1$.

The radiative transfer equation for time-independent polarised radiation is:

$$\frac{\mathrm{d}\mathbf{I}_\lambda}{\mathrm{d}\tau_c} = \mathcal{K}_\lambda(\mathbf{I}_\lambda - \mathbf{S}_\lambda), \tag{1.20}$$

where $\mathbf{S}_\lambda$ is the source function, $d\tau_c = -\chi^{\mathrm{C}}\mathrm{d}s$ is the continuum optical depth given by the continuum absorption coefficient χ^{C} at 5000 Å and $\mathcal{K}_\lambda$ is the propagation matrix that con-

tains all the absorption and dispersion (phase modulation) properties of the interactions between radiation and particles.

The propagation matrix contains properties of both the continuum and spectral lines: $\mathcal{K}_\lambda = \mathbf{1} + \eta_0 \mathcal{K}_\lambda^{\mathrm{L}}$, with $\mathbf{1}$ standing for the 4×4 identity matrix and $\eta_0 = \chi^{\mathrm{L}}/\chi^{\mathrm{C}}$ being the ratio of line and continuum absorption coefficients. The line propagation matrix can be further split into three terms:

$$\mathcal{K}_\lambda^{\mathrm{L}} = \begin{pmatrix} \eta_I & 0 & 0 & 0 \\ 0 & \eta_I & 0 & 0 \\ 0 & 0 & \eta_I & 0 \\ 0 & 0 & 0 & \eta_I \end{pmatrix} + \begin{pmatrix} 0 & \eta_Q & \eta_U & \eta_V \\ \eta_Q & 0 & 0 & 0 \\ \eta_U & 0 & 0 & 0 \\ \eta_V & 0 & 0 & 0 \end{pmatrix} + \begin{pmatrix} 0 & 0 & 0 & 0 \\ 0 & 0 & \rho_V & -\rho_U \\ 0 & -\rho_V & 0 & \rho_Q \\ 0 & \rho_U & -\rho_Q & 0 \end{pmatrix}. \tag{1.21}$$

Each matrix element contains the line absorption profile (the Voigt function) and the line dispersion profile (Faraday-Voigt function). The Faraday-Voigt function is, similarly to the Voigt function, a convolution of a natural line dispersion profile and the Gaussian function, and it has an anti-symmetrical shape. Here, we simplified the notation by removing any wavelength dependence in these matrix elements.

The first matrix in Eq. (1.21) corresponds to the absorption of each Stokes component by the same amount. The second matrix represents the dichroism effects where each polarisation component is attenuated differently, and it effectively couples the specific intensity I with the polarisation states Q, U and V. The third matrix represents dispersion effects, also known as the magneto-optical effects, which do not alter the polarisation degree but are responsible for the modulation of the polarisation states.

The magnetic field permeating an atmosphere establishes a preferred, mutually perpendicular directions in which a radiation field is more or less strongly absorbed. One direction corresponds to the direction of the magnetic field vector, while the other two are in the plane perpendicular to it. These directions are reprojected onto the coordinate system established by the direction of radiation propagation and the plane perpendicular to it. The reprojection angles of a magnetic field vector are inclination θ and azimuth ϕ that are contained in the propagation matrix elements $\eta_{I,Q,U,V}$ and $\rho_{Q,U,V}$ (equations for these terms can be found in, e.g., del Toro Iniesta 2003).

1.2.3.1 Zeeman effect

The splitting of spectral lines in the presence of an external magnetic field was first observed by the Dutch physicist Pieter Zeeman, who received the Nobel prize for this discovery (shared with Hendrik Antoon Lorentz) and after whom this effect was named. In the simplest case, a spectral line is split into three components: one unshifted (π) component linearly polarised and two symmetrically shifted (σ_b and σ_r) components with respect to the central wavelength of the unsplit line that are elliptically polarised with the phase difference of 180° (Fig. 1.9). Laboratory measurements of the Zeeman effect have shown that most spectral lines are split into more than just three components, as each of π and $\sigma_{b,r}$ can also be split into multiple sub-components. The theoretical description of the Zeeman effect is given by quantum mechanics. A quantum description of an atom will be reviewed following the theory presented in Degl'Innocenti (2014).

The line splitting results from the interaction between an external magnetic field with the orbital angular momentum, $\mathbf{L}$ and the spin angular momentum, $\mathbf{S}$, of a bound electron.

These interactions cause the splitting of atomic energy levels, thus splitting a spectral line. The state of an electron in an atom is defined by the Dirac equation (relativistic form of the Schrödinger equation) of form:

$$\hat{H}|\psi\rangle = E|\psi\rangle. \tag{1.22}$$

In the equation above, $\hat{H}$ is the Hamiltonian of the system, and $|\psi\rangle$ is the wave function of the electron corresponding to a level with energy E. The $\hat{H}$ contains all possible interactions exerted on an electron. In the simplest case, we account only for the electrostatic interactions with the atomic nucleus, $\hat{H}_0$, and the interaction of orbital and spin momenta of an electron ($\hat{H}_{LS}$, spin-orbit interaction). This case is known as the Russel-Saunders coupling, or the LS coupling, in which $\hat{H}_{LS}$ is treated as a small perturbation to $\hat{H}_0$.

The solution of Dirac's equation in the LS coupling scheme is described with quantum numbers L and S corresponding to the **L** and **S**, respectively. The quantum numbers represent an electron's constants of motion in a vector space in which $\hat{H}$ is represented by a diagonal matrix. Each atomic level in an atom is defined by a unique set of quantum numbers L and S, represented uniquely with a term symbol ^{2S+1}L. The superscript is known as the level multiplicity and L is symbolised by letters S, P, D, F for $L = 0, 1, 2, 3$[8]. For example, an electron in a ground state of a neutral iron with a term symbol ^{5}D has the corresponding quantum numbers, $S = 2$ and $L = 2$.

The interaction of an external magnetic field with a bound electron having the atomic orbital angular momentum **L** and the spin angular momentum **S**, adds another interaction term to H in the form:

$$H_M = \mu_0(\mathbf{J} + \mathbf{S}) \cdot \mathbf{B},$$

where **B** is the magnetic field vector and $\mathbf{J} = \mathbf{L} + \mathbf{S}$ is the total angular momentum of an electron. This magnetic interaction term is treated as a perturbation to $H_0 + H_{LS}$ where the inequality $H_M \ll H_{LS} \ll H_0$ simplifies the solution of Dirac's equation. The diagonalization of H_M introduces a new quantum number J (the eigenvalue of H_M) that corresponds to **J**. An electron state is now fully described by quantum numbers L, S and J combined in the term symbol $^{2S+1}L_J$.

The energy of atomic levels, E_{LS}, obtained in the LS coupling scheme, are degenerate when there is no magnetic field. This degeneracy of an atomic level has already been introduced in Sec 1.2.2.1 where we called it the statistical weight of a level, which is equal to $2J + 1$. Atomic levels are split into $2J + 1$ sublevels when $B \neq 0$ (Fig. 1.9), each with an energy differing from E_{LS} by an amount:

$$\Delta E_M = \mu_0 B M g_J,$$

where μ_0 is Bohr's magneton. g_J is the Landé factor of a level defined by the quantum numbers J, L and S, which can be explicitly computed only in the LS coupling scheme as:

$$g_J = \frac{3}{2} + \frac{S(S+1) - L(L+1)}{2J(J+1)}.$$

The quantum number M is the magnetic quantum number of J_z, which is a projection of **J** onto the direction of the magnetic field (assumed to be along the z-axis). It can take

---

[8]The complete list of letters identifying a term with $L > 3$ can be found in, e.g., Degl'Innocenti (2014).
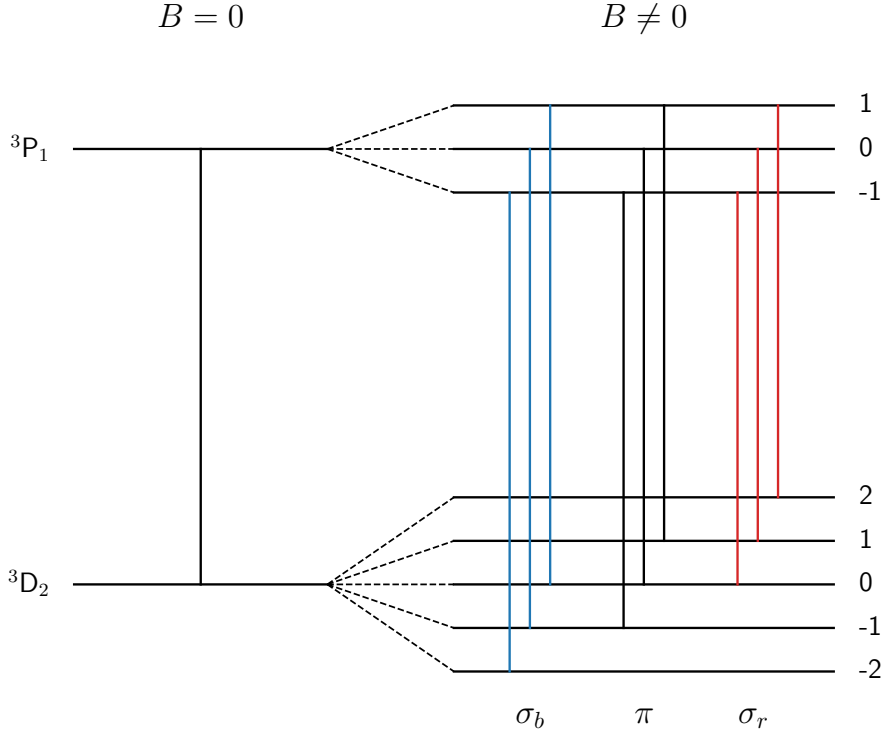
Figure 1.9. Splitting of the atomic levels involved in a transition due to the magnetic field. Spectral line for $B = 0$ is split into three components for $B \neq 0$ each obeying the selection rule $\Delta M = 0, \pm 1$ (π and $\sigma_{b,r}$ components). In the presented example, each Zeeman component comprises the three spectral subcomponents.

values $-J, -J + 1, ..., J - 1, J$. For a level with $J = 0$, we have only one sublevel with $M = 0$ and thus no level splitting (corresponds to term symbol ${}^1S_0$).

The selection rules define transitions that are possible between two split terms. For the Zeeman splitting, only transitions with $\Delta M = M_u - M_l = 0, \pm 1$ are possible, where M_u and M_l correspond to the magnetic quantum numbers of upper and lower levels of a transition, respectively. Above these rules, we have selection rules for dipolar electric transitions which impose restrictions on the changes of quantum numbers in the LS coupling scheme that are: $\Delta L = \pm 1$, $\Delta S = 0$ and $\Delta J = 0, \pm 1$ ($0 \leftrightarrow 0$). Most of the lines observed in solar and stellar spectra follow these rules, which come from the multipole expansion of the interaction Hamiltonian and keeping only the dipolar term of the electric field vector (more on this in Sec. 1.3.1.2).

The three transitions with $\Delta M = 0, \pm 1$ correspond to the previously introduced line components: π for $\Delta M = 0$ and $\sigma_{b,r}$ for $\Delta M = \pm 1$, respectively. The wavelength shift of each line component in Angstrom is:

$$\Delta \lambda_B = 4.67 \times 10^{-10} \lambda_0^2 B(g_l M_l - g_u M_u),$$

when B is given in Gauss and λ_0 in Angstrom.

As expected, multiple line components appear from level splitting (Fig. 1.9). However, in observations, we have effectively three components corresponding to the selection rules imposed on M. The final line and dispersion profiles included in the propagation matrix elements are weighted sums of line and dispersion profiles for each component of an

unsplit line. The weighting coefficients are determined from the quantum numbers of levels between which each line component is formed. This is a valid assumption if each sublevel is equally populated (the collisions between particles dominate over the photon scattering).

When a spectral line is observed from a viewing direction parallel to the magnetic field lines, only $\sigma_{b,r}$ components exist and are circularly polarised. When observed in a direction perpendicular to the magnetic field vector, all three components are observed and are linearly polarised. The π component is polarised parallel to the magnetic field, whereas $\sigma_{b,r}$ components are polarised perpendicularly to the magnetic field.

1.3   The atomic line parameters

In the previous section, we described the formation of spectra through interactions between radiation and atmospheric particles. Assuming that atmospheric parameters are known (temperature, density, velocity and magnetic field), we can compute the polarised absorption and emission coefficients in the atmosphere at each depth, compute the source function and optical depth, and thus solve the radiative transfer equation to obtain a spectrum. However, the computation of the absorption and emission coefficients (specifically, level populations) relies on the known atomic parameters of levels between which a spectral line we are modelling is formed. Throughout the thesis, we will always consider that the line is formed in the LTE approximation where the Boltzmann and Saha distributions give level populations.

The atomic parameters that are relevant for the line formation in LTE are the electronic configuration of atomic levels (quantum numbers), the energy of the lower level of the transition, the central wavelength of the line, transition probability $A_{u,l}$, Landé g-factors, collisional broadening (i.e., coefficients of the ABO theory) and abundance. The abundance of a chemical element is actually a characteristic of an atmosphere (its chemical composition). However, throughout the thesis, we will refer to it as an atomic parameter since it does not depend on the underlying physical conditions in an atmosphere, which is true for any other atomic parameter listed above. All these atomic parameters alter the absorption in the spectral line changing the layers in the atmosphere to which the spectral line is sensitive, and so its diagnostic potential for inferring the atmospheric parameters (for more on the line sensitivity to atmospheric parameters and the inference methods, see Sec. 2.2). The inference of atmospheric parameters from observed spectra using the wrong or inaccurate values of atomic parameters introduces an error in the inferred atmospheric parameters. We need to have reliable atomic parameters to be able to determine the physical structure of the solar atmosphere accurately.

Many atomic and molecular line databases contain all the necessary data for modelling spectral lines. Some of the most comprehensive and widely used ones in solar/stellar physics are the NIST[9] (Kramida et al. 2022), Kurucz[10] (Kurucz & Bell 1995) and VALD[11] (Piskunov et al. 1995) databases. There are three approaches for determining atomic parameters: experimental measurements of line intensity in laboratory setups, theoretical

---

[9] https://www.nist.gov/pml/atomic-spectra-database
[10] http://kurucz.harvard.edu/
[11] http://vald.astro.uu.se/

computations of an atomic structure, and inference from observed solar and stellar spectra.

We will first review how the transition probability parameter, $A_{u,l}$, is determined in each of the approaches. This will aid in understanding the limitations of each approach, developments achieved over the years of research and the diversity of methods that complement each other. After a discussion regarding the $A_{u,l}$ parameter, we will discuss the determination of the central wavelength of a spectral line. The knowledge of the precise central wavelength of a line is essential for revising the energy levels of atoms (Borrero et al. 2003), identifying new energy levels in atoms (Peterson & Kurucz 2022), accurate identification of spectral lines in line-rich spectra, especially of iron-group elements (Nave et al. 2017), and for the determination of the line of sight velocity stratification in the solar atmosphere.

1.3.1 The transition probability

An alternative way of expressing the transition probability $A_{u,l}$ is using a dimensionless parameter called the oscillator strength f. It is introduced as a quantum correction to a classically derived transition probability. The oscillator strength effectively decreases the classically derived probability of photon absorption or emission. Usually, the oscillator strength is a very low number, and only for a few strong lines it reaches unity. This parameter is poorly known and calculated for many spectral lines mainly using the theoretical approach, prone to significant uncertainties (see Sec. 1.3.1.2 for more details). We have accurate oscillator strengths measured in laboratories only for a small number of lines.

The oscillator strength, f, is related to $A_{u,l}$ by (Degl'Innocenti 2014):

$$A_{u,l} = \frac{2\pi e_0^2 \nu_{l,u}^2}{\epsilon_0 m_e c^3} \cdot \frac{g_u}{g_l} f,$$

where e_0 is the electron charge, ϵ_0 is vacuum electric permittivity, and g_l and g_u are the statistical weights of the lower and upper levels, respectively. The oscillator strength is commonly multiplied by the statistical weight of an energy level to form a gf factor. Because the gf factor is a very small number, in atomic line databases, it is usually given as $\log(gf)$.

Accurate $\log(gf)$ values for many spectral lines are of significant importance for measuring the chemical composition of the Sun to which we scale the composition of all other astronomical objects (e.g., Asplund et al. 2009). Furthermore, the chemical composition of other stars is essential to understand the evolution of stars and test the current theories of stellar evolution (Asplund et al. 2009). Thus, we are motivated to contribute to this effort and provide the wider astronomical community with accurate $\log(gf)$ values that would allow us to understand the Universe better.

1.3.1.1 Experimental measurements

Atomic physics laboratories are invaluable for providing scientists with atomic parameters of spectral lines with low uncertainties. Low uncertainties are achieved by precise control of the physical conditions in spectroscopic furnaces that produce emission or absorption lines of an element for which we want to measure the $\log(gf)$ parameter (Blackwell & Collins 1972). The most precise results are achieved by measuring the relative $\log(gf)$

values based on the ratios of line strengths either by measuring the line core intensities (in emission spectra) or the equivalent widths (in absorption spectra; e.g., Wiese 1970, Blackwell & Collins 1972). Based on which kind of spectrum we are using, we differentiate between the absorption and emission methods, which are expected to provide the same results. The precise measurement of absolute $\log(gf)$ values is achieved by measuring the lifetime of an energy level.

The absorption method produces the spectrum by passing light from a continuous source through a vapour created by heating a plate made from the element of interest. The plate must be in the purest form to ensure that the observed lines are produced only by the element for which we are measuring $\log(gf)$ values. As the source of light, for example, Blackwell & Collins (1972) used a high-pressure xenon gas lamp (Collins et al. 1970).

The strength of the observed line depends on the furnace's physical conditions, its length, and the $\log(gf)$ parameter. Very weak lines are observed only in long enough furnaces so that enough photons are absorbed at the wavelength of the line (Blackwell & Collins 1972). The proper measurement of the equivalent width assumes a constant temperature and pressure along the furnace. The relative $\log(gf)$ values are calculated from the ratio of equivalent widths of two spectral lines, thus removing any temperature and pressure dependence. This approach is valid only if both lines originate from the same lower level. Otherwise, the relative $\log(gf)$ will depend on the Boltzmann factor, $e^{-(E_{l,1}-E_{l,2})/kT}$, which is temperature dependent and contains the difference between the lower level energies of the two lines, $E_{l,1}$ and $E_{l,2}$.

The measured relative $\log(gf)$ values are set on an absolute scale by the absolute $\log(gf)$ value of another line, which is determined using some other method (e.g., measurement of the lifetime of a level; see below for more details). The reference line used for setting the absolute $\log(gf)$ scale of iron lines is the line at 371.994 nm (e.g., Bridges & Wiese 1970, Klose 1971). Iron lines are important in solar physics because they are the most numerous, from ultraviolet to infrared wavelengths. A group at Oxford made a considerable effort to accurately measure experimentally the relative $\log(gf)$ values of many iron lines originating from low excitation levels in a series of papers that started with Blackwell et al. (1975). They report the accuracy of the absolute $\log(gf)$ values to be 0.02, which corresponds to the relative error of around 5%. Later, they included the measurements of titanium (Blackwell et al. 1982) and nickel lines (Blackwell et al. 1989), the other two elements with many lines in the solar spectrum. These elements, iron, titanium and nickel, have many of lines in the solar spectrum because they have many energy levels between which lines are formed and have relatively high abundance in the solar atmosphere (e.g., Asplund et al. 2009).

The measured line core intensity in the emission method is assumed to be directly proportional to the transition probability and the number density of emitting atoms. The spectral lines are produced by directly heating the plate made from the element for which we are measuring $\log(gf)$ values. Assuming that the plate is uniformly heated, the ratio of line core intensities of two spectral lines will be proportional to the difference between respective $\log(gf)$ values. The same Boltzmann factor as in the absorption method would need to be included for computing the relative $\log(gf)$ values unless these two lines originate from the same upper level. The problem with the emission method is in the accurate measurement of the background continuum, contamination of the line core intensity by

the wings of nearby lines, and the reduction of the line core intensity by self-absorption in the evaporated gas from the heated plate (Wiese 1970). The advantage of the emission method is that it can reach higher excitation levels, which are otherwise not accessible to the absorption method (Blackwell et al. 1975).

The absorption and emission methods can be used to measure the absolute $\log(gf)$ values. However, the uncertainties of the absolute $\log(gf)$ values are much larger than for the relative $\log(gf)$, determined either using the absorption or emission method. The reason behind this is the difficulty of maintaining a constant temperature and pressure along the furnace. Any slight deviation in temperature along the furnace will cause inhomogeneity in the number density of atoms and thus propagate into the uncertainty of determined $\log(gf)$ value. The number densities are computed under the LTE approximation using the Boltzmann-Saha distribution, which is a reasonable assumption. Any deviations from LTE will contribute to the error in the result both for the absolute and the relative $\log(gf)$ value. The accuracy of determined $\log(gf)$ values can be examined by analysing the spread in the inferred abundance of an element from each line in the solar spectrum (Blackwell & Collins 1972, Blackwell et al. 1976). For this purpose, a proper atmospheric model is used to compute a spectrum which is compared with the observed one.

The lifetime method used to measure the absolute $\log(gf)$ values does not depend at all on the physical conditions inside the furnace. It is an ideal method for providing the absolute $\log(gf)$ values with low uncertainty. The method is based on measuring an excited state's decay rate by observing the emission line intensity decay. The upper level is populated in the collisional excitation by a pulsed beam of electrons (Klose 1971) or in the radiative excitation using a laser (den Hartog et al. 1987). Assuming that the decay of the excited electron to the lower levels occurs only by the spontaneous de-excitation (Wiese 1970), the lifetime of the excited level, Δt, is the time in which e number of atoms are de-excited and given by Eq. (1.17). The decay of line intensity over time is fitted with an exponential function plus the constant continuum (describing the background intensity) to determine the lifetime of a level (Klose 1971).

To determine the transition probability of a specific transition in this decay, we have to calculate the rate of each transition between the upper and lower levels. This rate is known as branching fraction, $BF_{u,l}$, and it is given by:

$$BF_{u,l} = \frac{A_{u,l}}{\sum_{l<u} A_{u,l}}, \tag{1.23}$$

where the branching fractions satisfy $\sum_l BF_{u,l} = 1$. The branching fractions are estimated from the ratio of line transition probabilities determined using either the absorption or the emission method.

Substituting the expression for lifetime from Eq. (1.17) in Eq. (1.23), we obtain the transition probability of a specific transition as:

$$A_{u,l} = \frac{BF_{u,l}}{\Delta t_u}.$$

However, computing the absolute $\log(gf)$ of lines by measuring the decay rate of a level is hindered by different processes that depopulate and populate a given level (Wiese 1970). The excitation of the level is hard to control, and the higher levels could also be

excited simultaneously. Any spontaneous decay from these higher levels can populate the level of interest, thus increasing the lifetime of the level (cascade effect). Additionally, the collisions between particles can induce electron transitions that cannot be disregarded. This problem is overcome by keeping the low density in the furnace by lowering the pressure, thus reducing the collisional (de-)excitation. Nevertheless, the improvements in laser physics achieved over the years allow us to populate only the level for which we are measuring the lifetime. This allows for the determination of precise absolute $\log(gf)$ values for many different elements using the lifetime measurement method in combination with branching fractions (see, e.g., Den Hartog et al. 2014).

The experimental measurements of $\log(gf)$ values are not limited to the methods described above, which are the most widely used methods whose results are cited in atomic line databases and are of the highest relevance for solar physics. The review of other methods and comparisons between them and their limitations are given in Huber & Sandeman (1986).

1.3.1.2 Theoretical determination

Theoretical computation of atomic structure allows for determining the transition probability between any two energy states in an atom in its interaction with the radiation field. The transition probability corresponds to the decay rate of an electron's energy averaged over the interaction time, which we already introduced as the Einstein coefficient for spontaneous emission $A_{u,l}$, given as:

$$A_{u,l} = \frac{2\pi}{\hbar} |\langle \psi_u | \hat{H}_\mathrm{I} | \psi_l \rangle|^2 \delta \left(h\nu_{l,u} - \Delta E_{u,l} \right), \tag{1.24}$$

where $\hat{H}_\mathrm{I}$ is the interaction Hamiltonian between the electron and the radiation field, $\hbar$ is the reduced Planck's constant ($h/2\pi$), and ψ_l and ψ_u are the wave functions for the lower and the upper level of the transition, respectively. **Dirac's delta function allows only interactions between the radiation field and an atom in which a photon is emitted or absorbed whose energy $h\nu_{l,u}$ corresponds to the energy difference between energy levels $\Delta E_{u,l} = E_u - E_l$.**

For a single electron system, the interaction Hamiltonian is proportional to $\mathbf{p} \cdot A_R(\mathbf{r})$, where $\mathbf{p}$ is the momentum of the electron at the position $\mathbf{r}$ that interacts with the radiation field having a vector potential A_R. The computation of the matrix element $|\langle \psi_u | \hat{H}_\mathrm{I} | \psi_l \rangle|^2$ is generally done by expanding the term in a series. The first expansion term, the electric dipole term, gives the strongest lines (with the largest transition probability). Most of the lines observed in the solar and stellar spectra are dipole transitions (allowed lines indicated as E1 in atomic line databases). Spectral lines originating from higher order expansion terms (magnetic dipole, electric and magnetic quadrupole) do appear in solar spectra (e.g., Mg I 4571 Å; Mauas et al. 1988), as well as in other astrophysical objects such as emission nebulae.

It is apparent from Eq. (1.24) that we need to know the wave functions and energy of corresponding levels between which transitions occur to compute the transition probability. These terms are obtained as a solution to Dirac's equation Eq. (1.22). The Hamiltonian must contain all possible interactions exerted on the electron in the atom. Hence, the Hamiltonian has the kinetic term due to the electron's motion around the nucleus, potential energy from electron-nucleus interaction, the potential energy of electron-electron

interaction (in multielectron atoms) and the spin-orbit interaction (magnetic interaction between electrons spin and orbital angular momenta). The solution of Dirac's equation can be explicitly obtained only for hydrogenic systems (hydrogen atom and hydrogen-like ions). For any other system with two or more electrons, only approximate solutions can be obtained (see, e.g., Cowan 1981).

The most regularly used approximate solution to Dirac's equation is the one given by Slater-Condon theory, where the wave functions are considered to be a linear combination of the basis functions (Cowan 1981). These basis functions correspond to the different electron configurations that are determined by the principal quantum number n and the angular quantum number l. These configurations are degenerate systems consisting of many substates that are defined by their own sets of quantum numbers that depend on the strength of the electron-electron interaction and the spin-orbit interaction terms (electron coupling). The energy of a configuration is calculated as the centre of gravity of each substate's energy.

The basis functions are determined in a numerical solution of Dirac's equation using either the perturbative or the variational method (Cowan 1981, Fischer et al. 2016). These basis functions are then used to construct the wave functions of each substate using the single-configuration or multi-configuration approximation. In the case of the single-configuration, the substate wave function is a linear combination of basis functions corresponding to the single configuration to which a substate belongs. This approximation is very useful for low-lying levels with no overlap in energy of different configurations. However, there is significant overlap for higher energy configurations, and the substate wave function is a linear combination of basis functions of all configurations that overlap in energy (multi-configuration approximation). The energies of substates in multi-configuration approximation are obtained as perturbations to energies determined in the single-configuration approximation. If some configuration substates have experimentally measured energies, these are used to fit theoretically determined ones, improving the accuracy of determined basis wave functions.

The nature of the basis functions depends on the chosen coupling scheme, simplifying their determination. The suitability of the coupling scheme is dependent on the problem at hand, and it is related to the strength of the electron-electron and spin-orbit interactions. In the case of strong spin-orbit interaction, we can treat the atom in the JJ coupling scheme, which is suitable for heavy atoms. In the JJ coupling, the orbital angular momentum **l** and the spin angular momentum **s** of a single electron are coupled to give a total angular momentum **j**, which then further interacts with the total angular momentum of other electrons. In the case of the weak spin-orbit interaction, we use the LS coupling scheme (Cowan 1981, already introduced in Sec. 1.2.3.1), which proved to be a good approximation for lower ionisation stages and light atoms and ions (Fischer et al. 2016).

Tremendous efforts have been made to compile the most extensive and comprehensive list of atomic lines that would be used to compute the absorption in stellar atmospheric models. Significant contributions are made by Kurucz & Peytremann (1975) (Kurucz database) as well as by Seaton (1987) (Opacity Project). The relative error of calculated $\log(gf)$ values can be smaller than 5% (0.02 in absolute value) for lines which are formed between levels with experimentally measured energies. However, for the theoretically predicted levels, the uncertainty of calculated $\log(gf)$ values can be greater than 25% (around 0.1 in absolute value; Pradhan & Saraph 1977).

Detailed explanations of different numerical approaches used to calculate the wave functions and corresponding level energies and their limitations are given in Cowan (1981) and Hibbert (1975). For a more modern review, see Fischer et al. (2016).

1.3.1.3   Inference from observed spectra

Determining the atomic line parameter from observed solar spectra requires a match of the synthetic spectra computed from an atmospheric model to the observed spectra. The accuracy of this approach is limited by the spectral resolution of the observations necessary to resolve all the spectral lines (line blending), normalisation of the spectrum (exact continuum level), treatment of spectral lines using either LTE or NLTE, treatment of collisional broadening, the quality of the atmospheric model to represent the physical conditions in the solar atmosphere realistically, and on the chemical composition of the atmosphere.

The $\log(gf)$ values determined from observed solar spectra are meaningless without specifying the abundance of chemical elements. This comes from the fact that the abundance, ϵ, and the $\log(gf)$ are coupled in the line absorption coefficient as $\log \chi^L \propto \epsilon + \log(gf)$. Thus, the same absorption coefficient in the line is achieved if we increase the abundance and decrease the $\log(gf)$ by the same amount (or vice versa). Nevertheless, if the abundances are updated, we can easily correct the $\log(gf)$ values allowing us to compare them to those of other research groups that used different abundances.

The determination of the $\log(gf)$ parameter for many spectral lines from the near ultraviolet to the infrared was first carried out by analysing the spatially-averaged disc-center quiet-sun spectrum. The $\log(gf)$ values were inferred from the line central intensity (Gurtovenko & Kostik 1981, 1982), whole line profile (Thevenin 1989, 1990) and the equivalent width of a line (Shchukina & Vasil'eva 2013). These works used some predetermined 1D solar atmospheric model to compute the synthetic spectrum. These atmospheric models are constructed to reproduce the continuum and spectral lines with experimentally measured $\log(gf)$ values from the spatially averaged spectrum. However, widely used 1D atmospheric models of the quiet Sun, such as HSRA (Gingerich et al. 1971), HOLMUL (Holweger & Müller 1974), VAL-C (Vernazza et al. 1981) and FAL-C (Fontenla et al. 1993), differ in temperature structure which results in different line profiles and thus impact the inferred $\log(gf)$ values (see a discussion in, e.g., Thevenin 1989).

Using the line core depth for determining $\log(gf)$ values is limited to lines which do not show saturation in the line core, are adequately modelled in LTE, and are free of blends. The requirement for the line core to be unsaturated means that the equivalent width of the line is directly proportional to the $\log(gf)$. Otherwise, the broadening of the line caused by collisions and micro-turbulent velocity can severely impact the inference of the $\log(gf)$ parameter. The line blending is overcome by analysing a whole blend simultaneously (Borrero et al. 2003) or deblending the spectral line of interest (Shchukina & Vasil'eva 2013).

Even if we analyse an unblended spectral line, it shows a broader profile than the computed line from a 1D atmospheric model. The recovery of an observed line width requires broadening the modelled line profile by the ad-hoc added macro-turbulent velocity parameter, v_{mac}. The macro-turbulent broadening preserves the equivalent width of the line, thus weakening the line core intensity and broadening the wings. If we use the line core depth to determine the $\log(gf)$ parameter, the additional macro-turbulent broadening

will induce coupling between the $\log(gf)$ and v_{mac}. Thus, we must carefully choose the correct value for v_{mac}, which is a line-independent parameter. This problem does not exist if we use the equivalent width of the line to determine the $\log(gf)$ parameter.

An improvement over using the 1D atmospheric model is achieved by Borrero et al. (2003) who used a two-component 1D model (Borrero & Bellot Rubio 2002) constructed by reproducing the observed infrared spectral lines with experimentally measured $\log(gf)$ values. The two-component model is composed of the granular and the intergranular 1D atmospheric models with a line of sight plasma flow that reproduces the observed line asymmetry (a consequence of unequal brightness, area coverage and opposite flow directions in granules and intergranular lanes in the quiet-sun region). This was a vital aspect for reproducing the observed line profiles and determining the $\log(gf)$ values in Borrero et al. (2003). Failure to reproduce the line asymmetry will result in the wrong line width, affecting the inference of the $\log(gf)$ value. Borrero et al. (2003) estimated the absolute error of $\log(gf)$ parameter to be around 0.06. On the other hand, Shchukina & Vasil'eva (2013) reported a relative error in their measurement, dominated by the measurement of the equivalent width of the line, of around 3% (0.013 in absolute value), but reaching 10% (0.043 in absolute value) for ultraviolet lines.

The shortcoming of using 1D atmospheric models for reproducing the spatially averaged spectra to determine the $\log(gf)$ values is in the non-linearity of the radiative transfer equation. Uitenbroek & Criscuoli (2011) showed that the spatially averaged spectrum from a 3D atmosphere is not the same as that from a horizontally averaged 3D atmospheric model. Additionally, the 1D atmospheric models (including the two-component model) are unable to realistically reproduce the shape of different spectral lines, the spectrum from the near ultraviolet to the infrared wavelengths, as well as their center-to-limb variation simultaneously (Uitenbroek & Criscuoli 2011). All of this points to the problem of using simple 1D atmospheric models to determine the $\log(gf)$ values from the spatially averaged spectrum.

Bigot & Thévenin (2006) removed the problem of choosing the correct atmospheric model by using a 3D radiation-hydrodynamical atmospheric model of the solar atmosphere. They determined the $\log(gf)$ values by matching the observed line profile to the temporally and spatially averaged line profile from the 3D model. The 3D atmospheric model can reproduce the observed line asymmetry and removes the necessity for applying macro-turbulent broadening. Also, the 3D models proved necessary for the solar elemental abundance determination from the spatially averaged spectrum (Asplund et al. 2021). Of course, this method requires using 3D atmospheric models with sufficient physics to reproduce the observed solar spectrum well.

Trelles Arjona et al. (2021) took a different approach and determined the $\log(gf)$ values for 15 infrared lines at $1.56\,\mu$m using the spectropolarimetric inversion method (for more on inversions, see Sec. 2). The authors simultaneously determined the atmospheric and $\log(gf)$ parameters by matching the synthetic spectra to the spatially resolved spectra of the quiet-sun region. In this approach, each pixel in the observed field of view is characterised with a $\log(gf)$ value for each line. A line's final $\log(gf)$ value is the average of all values retrieved from pixels with the best match of the synthetic spectrum to the observed one.

The shortcoming of this method is in the degeneracy of the absorption coefficient in the line due to the cross-talk between atmospheric parameters and the $\log(gf)$: the
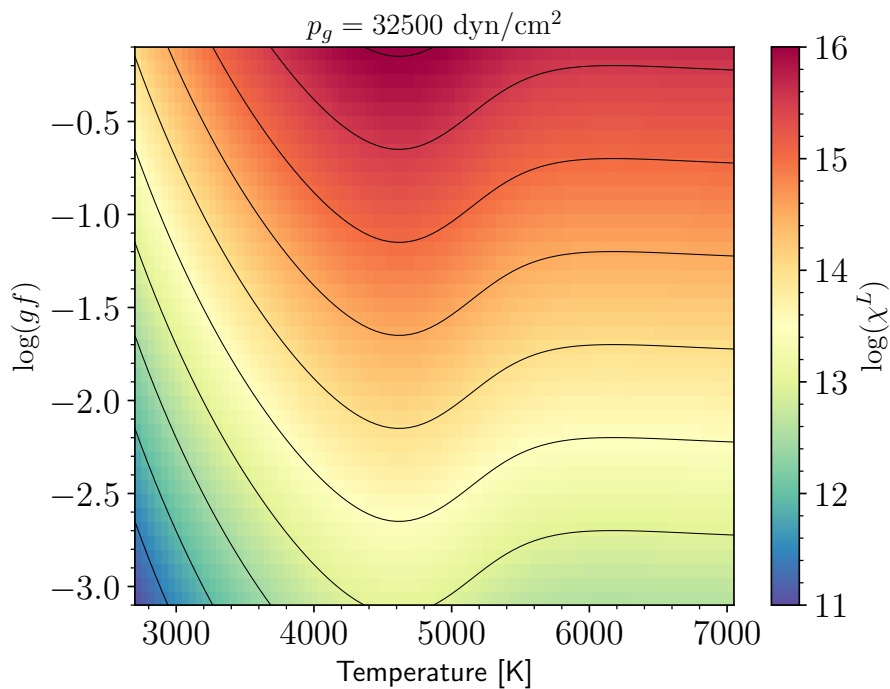
Figure 1.10. The absorption coefficient for the Fe I spectral line at 4016.419 Å for a gas pressure of 32 500 dyn/cm^2. The black lines represent constant χ^L.

same absorption coefficient can be recovered by having a different set of temperature and $\log(gf)$ values. Fig. 1.10 shows the absorption coefficient in the line for different sets of the temperature and the $\log(gf)$ parameter at a constant gas pressure. The same absorption coefficient can be reproduced at lower temperatures (below 4500 K) if we increase the temperature and decrease the $\log(gf)$ parameter; for temperatures above 5800 K, the absorption coefficient shows no dependency on the $\log(gf)$ parameter. Between these two regimes, an increase in the temperature increases the $\log(gf)$ while maintaining a constant absorption coefficient. It must be mentioned that not every spectral line will show exactly the same behaviour between the temperature and the $\log(gf)$. However, they all exhibit a similar cross-talk between them.

This shows that the same fit quality can be achieved with diverse sets of temperature and $\log(gf)$. Even a small difference in the temperature in the order of 100 K results in the change of $\log(gf)$ parameter by 0.01. It points to the weakness of a method from Trelles Arjona et al. (2021) in decoupling the contribution of the temperature and the $\log(gf)$ parameter to the absorption coefficient and, thus, to the resultant line profile. However, the authors have developed a three-step procedure to overcome this cross-talk and obtain reliable results.

Similar to the inference of the $\log(gf)$ values from the spatially averaged disc-center quiet-sun spectrum, the disc-integrated spectra of distant stars are also used to infer $\log(gf)$ values (e.g., Boeche & Grebel 2016, and references therein). This method determines the $\log(gf)$ parameter from the equivalent width of observed lines in the visible and infrared wavelength regions that are useful for determining stellar parameters: effective temperature, surface gravity and elemental abundances (Bigot & Thévenin 2006,

Boeche & Grebel 2016). They use 1D atmospheric models of different benchmark stars (such as Sun, Arcturus, and Vega) to synthesize the spectra for different sets of $\log(gf)$ values and match the synthetic to the measured equivalent width of the line. They employ a grid search algorithm (Laverick et al. 2019, with seven benchmark stars), or a statistical method called the cross-entropy method (Martins et al. 2014, with three benchmark stars). The final result is the average $\log(gf)$ retrieved from all benchmark stars.

The grid search and the cross-entropy methods are only applicable for measuring the $\log(gf)$ parameter of unblended spectral lines, as was the case for the $\log(gf)$ inference from the spatially averaged disc-centre quiet-sun spectrum. Boeche & Grebel (2016) proposed measuring the equivalent width of a blended line pair in multiple spectra of different benchmark stars to decouple each line's contribution to the blended profile. This is possible if the number of blended lines is equal to or lower than the number of benchmark stars and assuming that stellar parameters and line-broadening contributors are well-known. A similar argument for decoupling the contribution of many lines in a blend is given by Laverick (2019).

In the spatially resolved observations of the solar surface, individual pixels are characterised by different thermodynamic and magnetic structures, producing diverse spectra. These various spectra can be viewed as spectra observed from benchmark stars with different effective temperatures and surface gravity. This thesis aims to use these diverse solar spectra and determine the $\log(gf)$ values for isolated and blended lines. We approached this problem by developing a new inversion method that is described in Sec. 2.4.1.

1.3.2 The central wavelength

The central wavelength is an important parameter used to identify spectral lines. Misidentifying the line could cause a wrong inference of $\log(gf)$ not only from the observed spectra, but also from the experimental measurements. The determination of the central wavelength of a line directly follows from the knowledge of the energy of levels between which the line originates. In the theoretical approach, when one of these levels has an experimentally measured energy, the calculated wavelength is called the Ritz wavelength.

Accurate experimental measurements of the central wavelength of iron lines, with an uncertainty of 2 mÅ at 1000 nm, can be achieved by the Fourier-transform spectrometer (e.g., Nave et al. 1994). The central wavelengths are computed by matching the observed wavelength of a line with the Ritz wavelength. Unidentified lines are verified by identifying the energy levels between which they are formed. A new energy level is determined, requiring that at least four observed lines originate from this level (see, e.g., Peterson & Kurucz 2022).

The central wavelength of a line is usually simultaneously inferred with the $\log(gf)$ from the observed spectra (Borrero et al. 2003). This is because these two parameters are coupled, and the poor results for $\log(gf)$ would be obtained if we do not account for the uncertainty in the line central wavelength. This is especially important for blended spectral lines because the inference algorithm can easily mix up the contribution of each blended line to the final profile, thus leading to the wrong inference of $\log(gf)$. Additionally, any uncertainty in the wavelength position of spectral lines in the spectra introduces an error in the inferred height variation of the line of sight velocity in the atmosphere.

2   Spectropolarimetric inversions

The previous chapter briefly introduced radiative transfer theory and explained the formation of spectral lines in a magnetized atmosphere. The physical conditions in the solar atmosphere are encoded into spectral lines. The line absorption coefficient varies strongly with wavelength within a spectral line, which causes photons to decouple from atmospheric particles at different heights in the atmosphere[1]. Observations taken at different wavelengths in a spectral line show atmospheric structures at different heights. This is why spectral lines are an invaluable diagnostic tool for studying the stratification of physical parameters in the solar atmosphere.

The observations of the Stokes vector $\mathbf{O}_\lambda(x, y)$ for every point (x, y) in the field of view and at every wavelength λ (containing one or many spectral lines), are transformed into the 3D stratification of physical parameters using a spectropolarimetric inversion method (or for short, inversion). The inversion method infers the physical parameters of an atmospheric model by matching a synthetic spectrum computed from this model with the observed one. To obtain the best match, we have to iteratively adjust physical parameters because of the non-linearities in the polarised radiative transfer equation. The physical parameters of the solar atmosphere that can be adjusted in each inversion step are temperature T, line of sight velocity v_{LOS}, magnetic field strength B, magnetic field inclination θ, magnetic field azimuth ϕ and micro-turbulent velocity v_{mic}. Some additional parameters that are depth-independent can also be inferred, such as the macro-turbulent velocity v_{mac} or the filling factor[2].

Currently, available inversion codes are well optimised for inference of the atmospheric parameters assuming the line formation in LTE or in non-LTE (for an extensive list of inversion codes, see del Toro Iniesta & Ruiz Cobo 2016). However, not many of these codes can also infer the atomic parameters, which play an essential role in the computation of the line absorption coefficient, altering the sensitivity of a line to the atmospheric parameters. Well-known inversion codes that are also capable of inferring the atomic parameters along with the atmospheric parameters are SIR (Ruiz Cobo & del Toro Iniesta 1992, Trelles Arjona et al. 2021), SPINOR (Solanki 1987, Frutiger et al. 2000) and NICOLE (Socas-Navarro et al. 2015).

---

[1] Over the wavelength range of a given spectral line, we can safely assume that the continuum absorption coefficient does not change with the wavelength and that it is much smaller than the absorption coefficient in the line core.

[2] The filling factor defines the contribution of the magnetized atmosphere in the two-component atmospheric models where the other one is non-magnetized. This parameter is used in low spatial-resolution observations where the magnetic elements are not resolved well. With the advances in the instruments for solar observations, we are approaching the resolution of the individual magnetic elements, and hence, the filling factor is becoming obsolete.

The aforementioned codes infer the atomic parameters for every resolution element (henceforth pixel) in the observed field of view individually. However, the atomic parameters are intrinsic characteristics of atoms, independent of the underlying atmospheric parameters in that pixel. In this thesis, we develop a new inversion method for inferring spatially coupled atomic parameters and pixel dependent atmospheric parameters. This new inversion method infers a single set of atomic parameters per spectral line that reproduces line profiles from different pixels simultaneously. We will focus on the inference of the $\log(gf)$ parameter and the $\Delta\lambda$ parameter, a correction to the central wavelength of a spectral line. Nevertheless, the method is nowhere restricted only to these two parameters, and it can be extended to fit for elemental abundances, Landé g-factors, energy of the lower level in a transition (energy of the upper level is computed simply as $E_l + h\nu_{l,u}$), collisional broadening parameter, etc. Simultaneous inference of all these parameters still has to be investigated, along with the optimal inversion strategy in each case. In Sec. 4.4, we briefly discuss the possibility for simultaneous inference of abundance and $\log(gf)$.

The following sections review the mathematical background and techniques used for inversions. These will be used later to describe the new method for a coupled inference of the $\log(gf)$ and $\Delta\lambda$ parameters. A review of the inversion method and many approaches used to optimise the atmospheric and atomic parameters is given in del Toro Iniesta & Ruiz Cobo (2016).

2.1   Pixel-by-pixel method

An important part of every inversion method is to define a merit function to be minimized through the iterative correction of free (inversion) parameters. Spectropolarimetric inversion algorithms generally use χ^2 as a merit function, which is defined for each pixel as (del Toro Iniesta 2003):

$$\chi^2(\mathbf{p}) = \frac{1}{N-n} \sum_{i=1}^{N} \frac{w_i^2}{\sigma_i^2} \cdot (\mathbf{O}_i - \mathbf{I}_i(\mathbf{p}))^2 \,, \qquad (2.1)$$

where the index i goes over each wavelength point for all four Stokes parameters ($N = 4N_\lambda$, N_λ being the number of wavelength points), and n is the number of free parameters. The factor w_i is the weight given to each wavelength, and σ_i is the corresponding noise at this wavelength[3]. $\mathbf{O}_i$ denotes the observed Stokes vector, and $\mathbf{I}_i(\mathbf{p})$ denotes the synthetic Stokes vector, with $\mathbf{p}$ representing an n-element vector of inversion parameters (atmospheric and atomic parameters).

The inversion of spectropolarimetric observations is a non-linear optimisation problem. For this kind of problem, a regularly used optimisation scheme is the Levenberg-Marquardt algorithm (Levenberg 1944, Marquardt 1963, henceforth LM), which is a combination of the gradient descent and the Gauss-Newton methods for minimizing a merit function.

The LM algorithm uses the first derivative of a model function to minimize the merit function that defines a hypersurface in the inversion parameter space. The χ^2 hypersurface

---

[3]In some equations for χ^2, the noise and weight factors are given as a single quantity that is simply referred to as weight.

may have many local minima and usually only one global minimum corresponding to the best inversion parameters set. However, some local minima can be almost as deep as the global minimum because of the cross-talk between different inversion parameters (see a discussion in Sec. 2.2). The LM algorithm efficiently finds a minimum of the merit hypersurface but does not guarantee that the found minimum corresponds to the global one. By adjusting the weights w_i of different wavelengths in the spectrum, it is possible to change the shape of the merit hypersurface. Such an adjustment can produce a more pronounced global minimum and increase the efficiency of finding the global minimum of the merit function. Finding the best fit to the observed spectrum depends on how close the initial solution is to the optimal one, the complexity of the model function and the employed weights.

In the LM algorithm, an initial guess for the inversion parameters is assumed to be close to the global minimum. Expanding the merit function around the global minimum in parameter space using a second-order Taylor polynomial yields (Press et al. 2007):

$$\chi^2(\mathbf{p}) = \chi^2(\mathbf{p_j}) + \Delta\mathbf{p_j}^T \cdot \nabla\chi^2(\mathbf{p_j}) + \frac{1}{2}\Delta\mathbf{p_j}^T \cdot \mathcal{H} \cdot \Delta\mathbf{p_j}, \tag{2.2}$$

where $\Delta\mathbf{p_j} = \mathbf{p} - \mathbf{p_j}$ is a correction for the parameter vector $\mathbf{p_j}$ in the j–th iteration, $\mathcal{H}$ is the Hessian matrix of the system, and T indicates the matrix transpose. Based on our assumption being at the minimum, we expect the gradient of χ^2 to be zero, $\nabla\chi^2(\mathbf{p}) = 0$. Thus, taking a gradient of Eq. (2.2), we obtain:

$$0 = \nabla\chi^2(\mathbf{p_j}) + \mathcal{H} \cdot \Delta\mathbf{p_j}, \tag{2.3}$$

where $\frac{d\Delta\mathbf{p_j}}{d\mathbf{p}} = 1$. In this derivation, we have used the identity:

$$\frac{d\left(\Delta\mathbf{p_j}^T \cdot \mathcal{H} \cdot \Delta\mathbf{p_j}\right)}{d\mathbf{p}} = \left(\mathcal{H} + \mathcal{H}^T\right) \cdot \Delta\mathbf{p_j} = 2\mathcal{H} \cdot \Delta\mathbf{p_j},$$

where we applied the symmetry property of the Hessian matrix, $\mathcal{H} \equiv \mathcal{H}^T$. Solving Eq. (2.3) gives the correction $\Delta\mathbf{p_j}$ for the initial parameter vector that minimizes χ^2.

Here we have implicitly assumed that the correction of the inversion parameters produces a linear change in the model, which produces quadratic change in the χ^2. Precisely this linearisation of the non-linear model requires an iterative correction of inversion parameters. This way of deriving Eq. (2.3) is more suitable when regularisation functions are added to the merit function (see Sec. 2.4.2 for more on regularisation), which are not necessarily linear with respect to parameters.

The gradient of the merit function from Eq. (2.3) is:

$$-\frac{\partial\chi^2}{\partial p_k} = \frac{2}{N-n} \sum_{i=1}^{N} \frac{w_i^2}{\sigma_i^2} \cdot (\mathbf{O}_i - \mathbf{I}_i(\mathbf{p})) \cdot \frac{\partial\mathbf{I}_i}{\partial p_k}, \tag{2.4}$$

where the term $\frac{d\mathbf{I}_i}{dp_k}$ is the response function of the Stokes spectrum to the k–th inversion parameter at wavelength i (del Toro Iniesta 2003, see also Sec. 2.2). With further differentiation of Eq. (2.4) with respect to parameter p_l, we obtain the Hessian matrix elements:

$$\mathcal{H}_{l,k} = \frac{\partial\chi^2}{\partial p_l \partial p_k} = \frac{2}{N-n} \sum_{i=1}^{N} \frac{w_i^2}{\sigma_i^2} \cdot \left[\frac{\partial\mathbf{I}_i}{\partial p_k} \cdot \frac{\partial\mathbf{I}_i}{\partial p_l} - (\mathbf{O}_i - \mathbf{I}_i(\mathbf{p})) \cdot \frac{\partial^2\mathbf{I}_i}{\partial p_l \partial p_k}\right]. \tag{2.5}$$

The second term under square brackets in Eq. (2.5) is usually disregarded in LM inversions (del Toro Iniesta 2003, de la Cruz Rodríguez et al. 2019). This is reasonable since it was assumed that the initial solution was close to the minimum. Therefore, $\mathbf{O} - \mathbf{I}(\mathbf{p_j})$ should be zero and the second-order derivatives will not influence the proposed parameter steps. Disregarding second-order derivatives ensures that the Hessian matrix is positive definite, and the step in parameter space leads to the minimisation of χ^2. In some occasions, the second-order derivatives can even lead to corrupted behaviour (Press et al. 2007).

Substituting Eq. (2.4) and Eq. (2.5) into Eq. (2.3), and identifying new terms, we obtain:

$$\mathcal{H} \cdot \Delta\mathbf{p_j} = \mathcal{J}^{\mathrm{T}} \cdot \mathbf{\Delta}, \tag{2.6}$$

where $\mathbf{\Delta}_i = \sqrt{\frac{2}{N-n}} \cdot \frac{w_i}{\sigma_i} \cdot \left(\mathbf{O}_i - \mathbf{I}_i(\mathbf{p_j})\right)$ and $\mathcal{J}$ is the Jacobian matrix of the system whose elements are given as:

$$\mathcal{J}_{i,k} = \sqrt{\frac{2}{N-n}} \frac{w_i}{\sigma_i} \frac{\partial \mathbf{I}_i}{\partial p_k}.$$

The linearisation of the Hessian matrix allows us to express it through the Jacobian matrix as $\mathcal{H} = \mathcal{J}^{\mathrm{T}}\mathcal{J}$.

Fitting non-linear models to observed data can lead to poor parameter corrections. To address this issue, the diagonal elements of the Hessian matrix are multiplied with a factor λ_{M} and added to the Hessian, yielding $\mathcal{H} = \mathcal{J}^{\mathrm{T}}\mathcal{J} + \lambda_{\mathrm{M}} \cdot \mathrm{diag}(\mathcal{J}^{\mathrm{T}}\mathcal{J})$. This factor is known as the Marquardt parameter and regulates the magnitude of the parameters correction (i.e., $\Delta p_k \propto 1/\lambda_{\mathrm{M}}$). For fast convergence, the Marquardt parameter should be small enough (e.g., $\lambda_{\mathrm{M}} < 10^{-2}$) but not too small to overstep the global minimum. The Hessian matrix is diagonalised for large values of the Marquardt parameter, and the parameter corrections are obtained from the gradient descent method. Approaching the χ^2 minimum, λ_{M} is smaller, allowing off-diagonal terms in the Hessian matrix to influence the parameter correction. These corrections are obtained then using the Gauss-Newton method, which ensures faster convergence to the minimum.

The iterative procedure for finding the χ^2 minimum and obtaining the best set of inversion parameters is the following. Start from an initial solution $\mathbf{p_0}$, which is assumed to be close to the global minimum. For this initial solution, Eq. (2.6) is solved to get the parameter correction $\Delta\mathbf{p_j}$. The new spectrum is computed for $\mathbf{p_j} = \mathbf{p_0} + \Delta\mathbf{p_j}$ and compared with the observed spectrum. If the proposed parameter correction yields a lower χ^2, the new parameter vector $\mathbf{p_j}$ is accepted and the λ_{M} parameter is lowered. However, if the new parameter values $\mathbf{p_j}$ deliver a larger value of χ^2, we reject them, raise the λ_{M} parameter, and calculate a new correction. This process is repeated until the desired accuracy or a maximum number of iterations is reached. Change in the Marquardt parameter is done by multiplying it or dividing it by a factor of 10.

Applying the LM algorithm to each pixel individually retrieves a single set of values for inversion parameters that reproduce the observed Stokes profiles in a given pixel. This method of inferring the inversion parameters is called the pixel-by-pixel method, and it is the most used approach for the inversion of solar observations.

2.2   Response functions

The response functions are a necessary part of the LM inversion algorithm since they are used to construct the Jacobian and Hessian matrices that regulate the magnitude of parameter corrections, minimising the χ^2 value. The response functions describe the response of the Stokes vector due to a small perturbation of physical parameters. Strictly mathematically speaking, we can write the response function for a parameter q as:

$$\mathbf{R}_q(\tau, \lambda) = \frac{d\mathbf{I}_\lambda(\tau)}{dq}, \tag{2.7}$$

at the optical depth τ at the wavelength λ. For a single atmospheric model, the response function is a four-dimensional vector in the space of the inversion parameters, atmospheric depth points, wavelengths and Stokes components.

Eq. (2.7) suggests that when we have the solution for $\mathbf{I}_\lambda(\tau)$, we can differentiate it over each inversion parameter and obtain the equation for the response functions. In general, the polarized radiative transfer equation does not have an analytical solution, and it is solved by applying a numerical method. Consequently, the response functions must also be calculated using some numerical method. The analytical solution of the polarized radiative transfer equation (and so for the response functions) exists only in exceptional cases, such as the weak-field approximation and the Milne-Eddington solution (we will not consider these solutions here; for more details, see, e.g., Sanchez Almeida 1992, Landi Degl'Innocenti & Landolfi 2004).

The simplest and most straightforward way for computing the response functions is using a numerical central difference method (see, e.g., Quintero Noda et al. 2016). From the initial value of a parameter, we make a positive perturbation by a small amount δq and compute the resulting Stokes vector $\mathbf{I}^+$. Next, starting from the same initial value, we repeat the process with a negative perturbation of the same magnitude and compute the corresponding Stokes vector $\mathbf{I}^-$. The response function of a given parameter is computed as $\frac{\mathbf{I}^+ - \mathbf{I}^-}{2\delta q}$. This numerical method allows us to compute the response function for arbitrarily complex atmospheric stratifications.

Another way of computing the response functions is using the linear perturbation method: inducing a small perturbation, δq of an inversion parameter produces a linear response in the Stokes vector (Landi Degl'Innocenti & Landi Degl'Innocenti 1977, Sanchez Almeida 1992). For simplicity, we shall consider here only the specific intensity I_λ and write:

$$\mu \cdot \frac{d(I_\lambda + \delta I_\lambda)}{dz} = -(\chi_\lambda + \delta\chi_\lambda) \cdot (I_\lambda + \delta I_\lambda) + (\eta_\lambda + \delta\eta_\lambda), \tag{2.8}$$

where δI_λ is a resultant small perturbation of the specific intensity I_λ, $\delta\chi_\lambda$ and $\delta\eta_\lambda$ are the small perturbations of the absorption and emission coefficients. After multiplying the brackets and ignoring the second-order term, $\delta\chi_\lambda\delta I_\lambda$, we recognize the terms from Eq. (1.3) that cancel each other. The leftover terms yield:

$$\mu \cdot \frac{d\delta I_\lambda}{dz} = -\chi_\lambda \cdot \delta I_\lambda - \delta\chi_\lambda \cdot I_\lambda + \delta\eta_\lambda. \tag{2.9}$$

If we group the last two terms in a single term labeled as η'_λ and divide the whole equation

by $-\chi_\lambda$, we end up with the equation:

$$\mu \cdot \frac{\mathrm{d}\delta I_\lambda}{\mathrm{d}\tau_\lambda} = \delta I_\lambda - Z_\lambda, \qquad (2.10)$$

which has the same form as Eq. (1.4) and its solution for δI_λ can be written as Eq. (1.7). In Eq. (2.10), the Z_λ term is the source function for the perturbation defined as $Z_\lambda = \eta'_\lambda/\chi_\lambda$.

If we have already developed a numerical method to solve the polarized radiative transfer equation, we can use the same one to obtain the response functions. The only thing missing are the perturbations of the absorption and emission coefficients, where all the dependencies on the atmospheric and atomic parameters are hidden. The strength of this method is that the response functions are computed synchronously with the Stokes vector, with a few additional terms that need to be computed. The convenience of this method for calculating the response functions of inversion parameters, its complexity, limitations and usefulness, and comparison with the central difference method is thoroughly described in Milić & van Noort (2017). The method is general enough to be applied to spectral lines modelled in the LTE or non-LTE approximation. However, currently, it is developed only for lines that can be realistically modelled using the complete frequency redistribution approximation. We have to remark here that even though Eq. (2.10) is convenient to calculate the response functions, it is still an approximation, assuming that the perturbation of a parameter produces a linear response of the Stokes vector.

Fig. 2.1 displays the response functions for temperature, line of sight velocity, magnetic field strength, inclination and azimuth and $\log(gf)$ for the Fe I line pair at 6301.5 Å and 6302.5 Å. Each panel that displays the response function for atmospheric parameters shows its variation with wavelength and depth in the atmosphere, where the colour corresponds to the magnitude of the response function. Since the $\log(gf)$ is an atomic parameter, it is depth-independent, and its response function thus varies only with wavelength. Hence, in the last row of Fig. 2.1, the y–axis represents the magnitude of the response function for $\log(gf)$.

The response functions are computed using the central difference numerical method with spectra normalized to unity. The spectrum's normalisation shifts the response of the continuum to the temperature perturbation into the line core (blue region in the top-left panel). We interpret this as follows: if we increase the temperature around the depth point $\log(\tau) = 0$, the continuum intensity will increase, thus making the line stronger by increasing its depth (the observed intensity in the line core would be smaller; hence, a negative sign for the response). The reverse situation happens if the temperature is increased around the height with the largest response in the line core. This increase causes the line to be weaker, which is observed as an increase in the line core intensity.

A negative value of the response function for $\log(gf)$ in Stokes I indicates that the increase in $\log(gf)$ increases the strength of the line, more in its wings than in the core. Similarly, we interpret all other panels that clearly show how valuable the response functions are in inferring the atmospheric and atomic parameters from the observed Stokes vector. The panels for the response functions for temperature and $\log(gf)$ in Fig. 2.1 indicate the aforementioned cross-talk between these two parameters, which impacts the proper retrieval of both. Simultaneous inference of these two parameters requires an approach that would decouple their impact on the Stokes vector by imposing additional constraints.
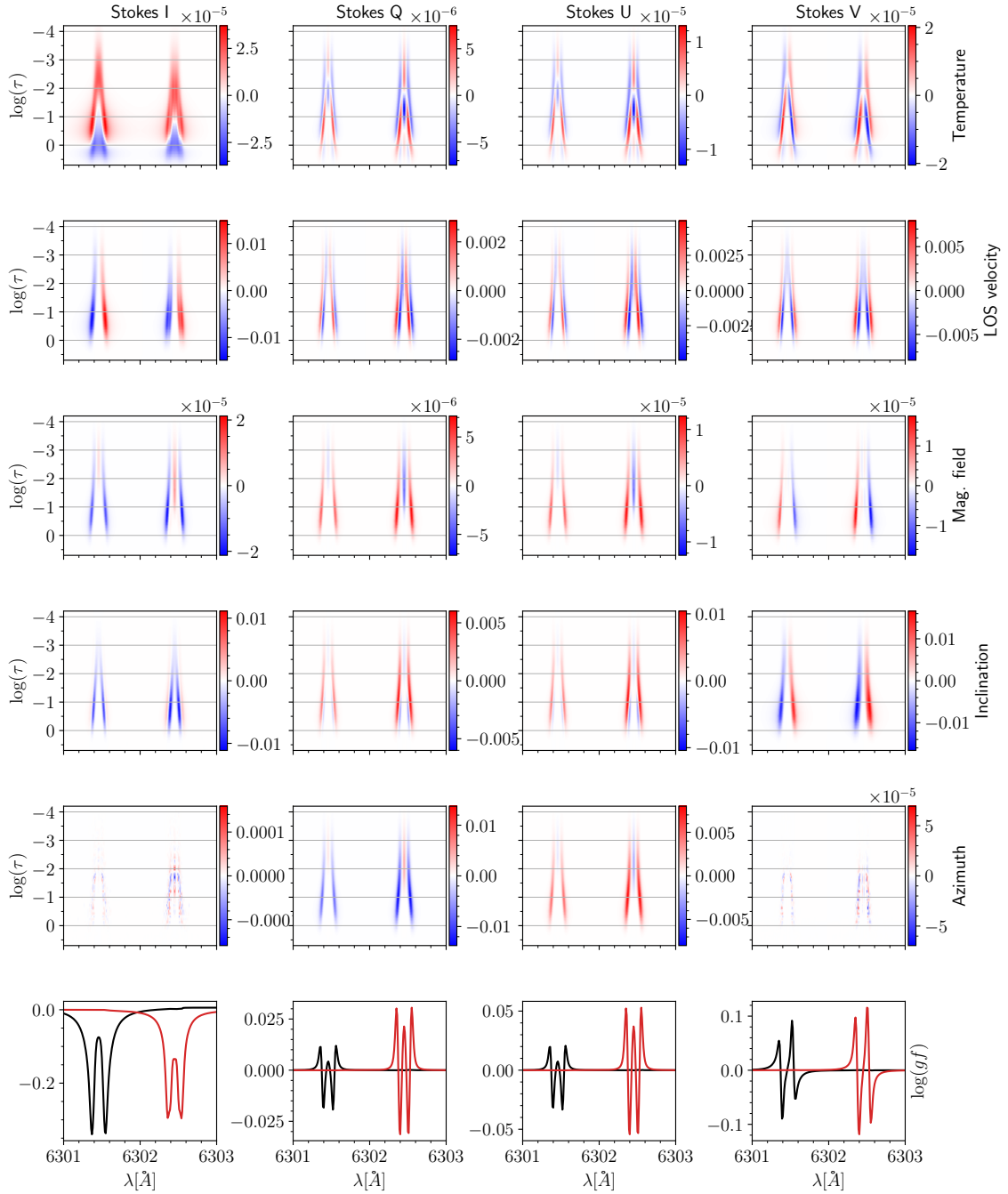
Figure 2.1. The response functions for temperature (first row), line of sight velocity (second row), magnetic field strength (third row), inclination (fourth row), azimuth (fifth row) and the $\log(gf)$ parameter (sixth row) for the Fe I line pair at 6301.5 Å and 6302.5 Å. The $\log(gf)$ response functions are computed for each line separately where black lines correspond to the 6301.5 Å line, and red lines to 6302.5 Å. The response functions are computed from the FAL-C atmospheric model with added magnetic field vector of $B = 800\,\mathrm{G}$, $\theta = 60°$ and $\phi = 30°$. The vertical columns correspond to each Stokes component respectively.

Another fact evident from Fig. 2.1 is the broad range of the Stokes vector sensitivity to perturbations in different parameters. We must remember that the response functions have a unit, which is an inverse of the unit of the parameter. The change of the unit system used in the inversion algorithm will also change the magnitude of the response functions for different inversion parameters. One way to approach this is to normalize the response functions and make them unitless by choosing a proper normalisation value. A suggestion by de la Cruz Rodríguez et al. (2019) is to use typical values of inversion parameters estimated in the solar atmosphere as a normalisation factor. Even this normalisation allows for smaller variations between the response functions for different parameters. The same type of normalisation is also implemented in the SNAPI code (Milić & van Noort 2018). We will discuss another way of normalising the response functions in Sec. 3.1.2.3.

Spectropolarimetric inversion is a degenerate ill-posed problem where different sets of atmospheric parameters can result in very similar spectra (for a review see del Toro Iniesta & Ruiz Cobo 2016). This implies that a certain degree of cross-talk exists between the atmospheric parameters even when the atomic parameters are well known. The parameters cross-talk is evident from the response functions in Fig. 2.1 where the Stokes vector shows a similar response to perturbations in different parameters. The response functions give us qualitative information that this cross-talk exists and can impact the inference of inversion parameters but do not indicate the strength of the cross-talk. The best way of examining the strength of the parameters cross-talk is to analyze the shape of the χ^2 hypersurface.

In the case of magnetic field inference, the linear polarisation signals, Q and U, are characterized by $180°$ ambiguity in azimuth, ϕ. This aspect is evident from equations for the elements of the propagation matrix, where absorption elements for Q and U are:

$$\begin{aligned} \eta_Q &\propto \cos\left(2\phi\right), \\ \eta_U &\propto \sin\left(2\phi\right). \end{aligned} \tag{2.11}$$

The exact proportionality also holds for the dispersive elements ρ_Q and ρ_U. Changing ϕ by $180°$ produces the same Stokes vector (Stokes Q takes the shape of Stokes U, and vice versa), and the inversion code cannot differentiate between these two cases since both provide an equally good fit. Magnetic field disambiguation can be done by, e.g., the minimum energy ambiguity resolution method (Metcalf 1994) or, since the launch of the Solar Orbiter (Müller et al. 2020), by the stereoscopic disambiguation method (Valori et al. 2022).

When the atomic parameters are also inverted, the parameters cross-talk becomes even more significant, especially between those quantities that affect a given spectral line similarly, for example, between T and $\log(gf)$ (see Fig. 1.10), and between v_{LOS} and $\Delta\lambda$. For example, the change in the central wavelength of Fe I 6301.5 Å line by 15 mÅ causes a shift in v_{LOS} by 0.95 km/s. The simultaneous inference of v_{LOS} and $\Delta\lambda$ requires at least one spectral line with a fixed central wavelength, which is used as an anchor point to which the central wavelengths of other lines and v_{LOS} are measured.

The previous discussion shows that the computation of the response functions is more demanding than computing a single Stokes vector. The inversion of observed spectra requires calculating the response functions for each inversion parameter in each iteration step, significantly increasing the computational complexity. We aim to simplify our at-

mospheric models to reduce the computations and, simultaneously, have complex enough models that reproduce the observed spectra.

2.3 Parametrization of atmospheric stratification

To minimize the impact of a numerical error on the computed Stokes vector, we require the stratification of inferred atmospheric parameters from photospheric up to chromospheric layers to be specified on a fine grid. This makes inference of each atmospheric parameter at every height intractable and computationally demanding. Therefore, a feasible inference of atmospheric parameters requires an approximation for their stratification. One kind of approximation is to parametrize the atmospheric stratification using a few points at properly chosen depths and interpolate between them to obtain values on a finer grid as needed for the spectral synthesis (Ruiz Cobo & del Toro Iniesta 1992, del Toro Iniesta 2003). These points are called nodes and are placed over the range over which the line and its nearby continuum respond to changes in the atmospheric parameters.

There exist two types of node parametrization. The first one assumes that nodes contain the corrections to the initial values of atmospheric parameters. Interpolation between the nodes gives a correction, added to the initial fine stratification of atmospheric parameters. This type of node parametrization requires the node's placement at the top and bottom boundaries of an atmospheric model. Choosing a different number of nodes will impose different corrections to the atmospheric parameters. In the case of a single node, we apply a constant correction at every depth; with two nodes, we have a linear correction; with three nodes, we have a quadratic correction and so on. This type of node parametrization is implemented in inversion codes `SIR` and `DeSIRe` (Ruiz Cobo et al. 2022).

The second type of node parametrization assumes that nodes contain absolute values of the atmospheric parameters. Interpolation between these nodes provides a fine stratification of atmospheric parameters. This type of node parametrization allows us to place nodes throughout the atmosphere over heights at which spectral lines are formed. It is implemented in many codes such as `SPINOR`, `NICOLE`, `STiC` (de la Cruz Rodríguez et al. 2019) and `SNAPI`.

However, choosing the correct positions of nodes is an art in itself. There has yet to be an explicit way for computing the required node positions. An intelligent way of node placement could be based on the response functions in each iteration, allowing for variable node placement. For now, it is left to a user to choose node positions (and number of nodes) based on the inverted observations (observed spectral lines, complexity of observed line profiles, wavelength sampling, noise level) and the user's experience in inverting data. A rule of thumb for choosing the node positions is based on the response functions computed assuming a representative 1D solar atmosphere model (such as FAL-C). We tend to place nodes in a range of heights where the response of a Stokes vector to parameter perturbations is the largest. Even then, a user must remember that the response functions differ for different atmospheric models: the height range in which a line is sensitive to atmospheric parameters is altered between various solar features.

Using any of the node approximations significantly simplifies the inversion of observations and inference of the atmospheric parameters. Since the computation of response

functions is very computationally heavy, lowering the number of atmospheric parameters improves the tractability of an atmospheric model.

2.4 The coupled inversion

An observed spectrum from a single pixel contains contributions from other nearby pixels because of the light diffraction and scattering by telescope and instrument elements, modelled by the point spread function (PSF). If the observations are taken from the ground, additional degradation of observations is caused by the refraction of light in the Earth's atmosphere. These effects are removed from observations by deconvolving them with the PSF of a telescope. This deconvolution recovers the original spectrum in each pixel but, at the same time, significantly increases the noise level in data. Inverting these observations with the pixel-by-pixel method described in Sec. 2.1 can produce results severely impacted by the noise. Thus, the inferred atmospheric parameters from a given pixel do not necessarily relate to the actual physical state of an atmosphere which emitted the observed spectrum.

To improve the quality of inferred parameters, we can follow a reversed approach: the synthetic spectra computed for each pixel in an observed field of view are first convolved with the PSF of a telescope and then matched to the observed spectra. The convolution of spectra from individual pixels introduces a spatial coupling between pixels and requires simultaneous match in all pixels to infer the inversion parameters. This inversion idea, named spatially coupled inversion, is presented by van Noort (2012). The convolution of spectra with the PSF of a telescope produces line profiles that should resemble the observed line profiles better than the profiles computed from a single atmospheric model. In van Noort et al. (2013), the method is extended to infer the atmospheric parameters on a sub-pixel scale, which is no smaller than the resolution limit of a telescope. This improvement increases the spatial resolution of the inferred atmosphere and maintains a robust inference of the inversion parameters (see, e.g., van Noort et al. 2013, Tiwari et al. 2013, 2015, Castellanos Durán et al. 2023).

Later, de la Cruz Rodríguez (2019) introduced a spatial regularisation method that limits the spatial variation of inversion parameters (for more details, see Sec. 2.4.2). Because of the energy exchange in the solar atmosphere between plasma parcels enclosed within each pixel, the neighbouring atmospheres are expected to have very similar physical parameters. That way, neighbouring pixels are effectively coupled, and it imposes a global optimisation for inversion parameters.

Both of these techniques were mainly concerned with retrieving atmospheric parameters, whereas in this thesis, we focus on the inference of atomic parameters. We have chosen to follow the approach of van Noort (2012) and to infer any global, field-of-view independent parameters, and in this thesis, the atomic parameters are $\log(gf)$ and $\Delta\lambda$.

2.4.1 Coupling of atomic parameters

In the pixel-by-pixel method, the Jacobian and the Hessian matrices are constructed for every pixel where Eq. (2.6) provides a parameters correction independently from other pixels. In the method for coupled inference of atomic parameters, a global parameter has

a uniform value in all pixels whose retrieval requires a coupling between the pixels. This coupling is introduced by requiring a simultaneous match of synthetic Stokes profiles to the observed ones from all the pixels. In this method, which we named the coupled method, inversion parameters are obtained by minimizing the sum of χ^2 of all the pixels:

$$\chi^2_{\text{global}}(\mathbf{p}) = \frac{1}{N - N_{\text{p}}} \sum_{a=1}^{N_{\text{atm}}} \sum_{i=1}^{N} \frac{w_i^2}{\sigma_i^2} \cdot (\mathbf{O}_{i,a} - \mathbf{I}_{i,a}(\mathbf{p}))^2 \, , \tag{2.12}$$

where the index a goes over every pixel in the observed field of view containing the total number of pixels N_{atm}, and N_{p} is the total number of free parameters summed over all pixels. Here, the parameter vector $\mathbf{p}$ contains inversion parameters from every pixel in the field-of-view $\mathbf{p} = (\mathbf{p}_1, \mathbf{p}_2, \ldots, \mathbf{p}_{N_{\text{atm}}})$.

The merit function for the coupled method is similar to the one given for the pixel-by-pixel method, except for the addition of a summation which runs over all pixels (atmospheres). Therefore, following the same procedure as in the pixel-by-pixel inversion, we derive an equation for the correction of the inversion parameters in the coupled method:

$$\mathcal{H}_{\text{global}} \cdot \Delta \mathbf{p_j} = \mathcal{J}_{\text{global}}^{\text{T}} \cdot \boldsymbol{\Delta} \tag{2.13}$$

where $\mathcal{H}_{\text{global}}$ and $\mathcal{J}_{\text{global}}$ are the global Hessian and Jacobian matrices of the system, respectively. The global Hessian and Jacobian matrices are connected in the same manner as in the pixel-by-pixel method. Therefore, to explain how the coupled method works, it would be sufficient to derive the global Jacobian matrix.

In the pixel-by-pixel method, column k in the Jacobian matrix contains the response function $\mathbf{R}_k$ of the Stokes vector to the k–th inversion parameter, where $\mathbf{R}_k$ is a vector of length $4N_\lambda$. In the case of n inversion parameters, the Jacobian matrix for a single pixel has a dimension $(4N_\lambda, n)$ and can be written as $\mathcal{J} = (\mathbf{R}_1, \mathbf{R}_2, \ldots, \mathbf{R}_n)$.

The global Jacobian matrix of the system is constructed by placing the Jacobian matrix of each individual pixel on the diagonal:

$$\mathcal{J}_{\text{global}} = \begin{pmatrix} \mathcal{J}_1 & 0 & \cdot & \cdot & \cdot & & & 0 \\ 0 & \mathcal{J}_2 & & & & & & \\ \cdot & & \cdot & & & & & \cdot \\ \cdot & & & \cdot & & & & \cdot \\ \cdot & & & & \cdot & & & \cdot \\ & & & & & \mathcal{J}_{N_{\text{atm}-1}} & 0 & \\ 0 & & \cdot & \cdot & \cdot & 0 & \mathcal{J}_{N_{\text{atm}}} \end{pmatrix} . \tag{2.14}$$

This block-diagonal matrix represents the uncoupled inference of parameters for each pixel. The transposed form of a block-diagonal matrix is a block-diagonal matrix of transposed sub-matrices, resulting in a block-diagonal global Hessian matrix. The global Jacobian matrix corresponds to the model with $n \cdot N_{\text{atm}}$ number of inversion parameters and has a dimension $(4N_\lambda N_{\text{atm}}, \, n \cdot N_{\text{atm}})$.

The global Jacobian matrix's block-diagonal form must be disrupted to achieve a coupled inversion. In the spatially coupled method of van Noort (2012), the diagonal form of the global Jacobian matrix is disrupted by convolving it with the PSF of the telescope (see Fig. 2.2). For the coupled inference of atomic parameters only, we need to couple

only those parts of the global Jacobian matrix that contain the response functions to the atomic parameters.

Let us assume that out of n parameters for each pixel, we have l local (atmospheric) and g global (atomic) parameters ($n = l + g$). The atmospheric parameters vary between pixels due to the different physical structures of each underlying atmosphere, while atomic parameters are the same for every pixel. In the coupled method, the total number of inversion parameters is, therefore, $N_{\text{atm}} \cdot l + g$, whereas, in the pixel-by-pixel method, this number is $N_{\text{atm}} \cdot (l + g)$. Additionally, we assume that the inversion parameters in the vector $\mathbf{p}$ are ordered from atmospheric to atomic.

Substituting the Jacobian sub-matrices with the response functions yields:

$$
\mathcal{J}_{\text{global}} =
\begin{pmatrix}
\mathbf{R}_1^1 \ldots \mathbf{R}_l^1\, \mathbf{R}_{l+1}^1 \ldots \mathbf{R}_{l+g}^1 & 0 & \cdot\ \cdot\ \cdot & 0 \\
0 & \mathbf{R}_1^2 \ldots \mathbf{R}_l^2\, \mathbf{R}_{l+1}^2 \ldots \mathbf{R}_{l+g}^2 & & \cdot \\
\cdot & & \cdot & \cdot \\
\cdot & & \cdot & \cdot \\
\cdot & & \cdot & 0 \\
0 & & \cdot\ \cdot\ \cdot & \mathbf{R}_1^{N_{\text{atm}}} \ldots \mathbf{R}_l^{N_{\text{atm}}}\, \mathbf{R}_{l+1}^{N_{\text{atm}}} \ldots \mathbf{R}_{l+g}^{N_{\text{atm}}}
\end{pmatrix},
\quad (2.15)
$$

where the upper index in the response function corresponds to the pixel number.

We have to reorder the response functions in this matrix to achieve the coupled inference of atomic parameters. For a single global parameter, we take its response functions for all the pixels and form a single column. Consequently, for the k–th parameter we have $\left(\mathbf{R}_k^1, \mathbf{R}_k^2, ..., \mathbf{R}_k^{N_{\text{atm}}} \right)^{\text{T}}$. Further, we repeat this process for each global parameter in the inversion. This results in a total of g columns that contain only the response functions to the global parameters. Then, we move these columns to the right side of the matrix. The rest of the matrix contains only the response functions to the local parameters. These response functions form a sub-matrix, which has a block-diagonal form. Therefore, the global Jacobian matrix after the reordering of the response functions is:

$$
\mathcal{J}_{\text{global}} =
\begin{pmatrix}
\mathbf{R}_1^1 \ldots \mathbf{R}_l^1 & 0 & \cdot\ \cdot\ \cdot & 0 & \mathbf{R}_{l+1}^1 \ldots \mathbf{R}_{l+g}^1 \\
0 & \mathbf{R}_1^2 \ldots \mathbf{R}_l^2 & & \cdot & \mathbf{R}_{l+1}^2 \ldots \mathbf{R}_{l+g}^2 \\
\cdot & & \cdot & & \cdot \\
\cdot & & \cdot & & \cdot \\
\cdot & & \cdot & 0 & \cdot \\
0 & & \cdot\ \cdot\ \cdot & \mathbf{R}_1^{N_{\text{atm}}} \ldots \mathbf{R}_l^{N_{\text{atm}}} & \mathbf{R}_{l+1}^{N_{\text{atm}}} \ldots \mathbf{R}_{l+g}^{N_{\text{atm}}}
\end{pmatrix}.
\quad (2.16)
$$

The block-diagonal form of the global Jacobian matrix is retained only for the local parameters, and the coupling is introduced only for the inference of global parameters. Corrections of global parameters are determined from spectrum differences in all pixels, while corrections for local parameters are determined from the spectral difference in a given pixel. This reordering keeps the pixel-by-pixel inference of atmospheric parameters and introduces the coupling of, e.g., atomic parameters.

The dimension of the global Jacobian matrix with coupling in atomic parameters is $(4N_\lambda N_{\text{atm}}, N_{\text{atm}} l + g)$, which is lower in comparison to a global Jacobian matrix for uncoupled inversion due to the grouping of the response functions of the global parameters. This coupling lowers the number of free parameters in the inversion, resulting in a χ^2 hypersurface that should produce fewer local minima. In the coupled method, we invert the same number of data points as in the pixel-by-pixel method with fewer parameters.

This adds more constraints to the inversion parameters and aids the inversion algorithm in finding the global minimum.

In the coupled method, a single value of the Marquardt parameter controls the step sizes for all parameters. In contrast, each pixel has its own Marquardt parameter in the pixel-by-pixel method. This difference has consequences in effectively locating the global χ^2 minimum. A similar set of equations is solved in the spatially coupled method of van Noort (2012). The author argues that to achieve convergence to the global minimum effectively, the inversion should be run for a small number of iterations (~10), after which the parameters are perturbed and used as initial values for the following inversion run. This way, the LM algorithm is kicked from any local minimum it may have strayed into to locate the global minimum.

2.4.2 Inversion parameters regularisation

The solution of ill-posed problems is susceptible to minor changes in the input parameters or the quality of observed data that can cause a very divergent solution, as is the case for spectropolarimetric inversions. The stabilisation of inferred parameters is achieved by imposing a regularisation of the inversion parameters. One type of regularisation is Tikhonov regularisation (Tikhonov & Arsenin 1977) which adds a quadratic penalizing term, $\Omega(\mathbf{p}, \mathbf{c})$, into the merit function as:

$$\chi^2_{\mathrm{reg}} = \chi^2 + \Omega(\mathbf{p}, \mathbf{c}), \tag{2.17}$$

where $\mathbf{c}$ is a regularisation weight that controls the strength of the regularisation imposed on each inversion parameter.

The regularizing function is chosen based on what kind of penalisation we want to achieve either in the horizontal or vertical direction: improving the smoothness of the inversion parameters and penalizing the gradients or deviations from some constant value. For the aforementioned spatial regularisation, de la Cruz Rodríguez (2019) suggests penalizing for strong oscillations in the inversion parameters between neighbouring pixels using the penalizing functions:

$$\begin{aligned} \mathcal{P}_{0,k}(i, j) &= p_k(i, j) - p_k(i - 1, j) \\ \mathcal{P}_{1,k}(i, j) &= p_k(i, j) - p_k(i, j - 1). \end{aligned} \tag{2.18}$$

This type of spatial regularisation couples the pixels above and to the left of the current pixel position (i, j), leading to a smooth spatial distribution of k–th inversion parameter p_k. The regularisation function Ω in this example has the following form:

$$\Omega(\mathbf{p}, \mathbf{c}) = \sum_{k=1}^{n_{\mathrm{pen}}} c_k \cdot \left(\mathcal{P}_{0,k}^2 + \mathcal{P}_{1,k}^2 \right), \tag{2.19}$$

where n_{pen} is the number of penalized inversion parameters, and we already summed the penalizing functions $\mathcal{P}_0$ and $\mathcal{P}_1$ over all pixels.

With the additional regularisation function, Eq. (2.13) is slightly modified. Owing to the nature of derivatives, it is sufficient to compute the Jacobian matrix of the regularisation function, $\mathcal{L}$, whose (l, m)–th element is the first derivative of the regularisation function for parameter p_l to the parameter p_m. Following the same procedure as in Sec. 2.1,

the correction of inversion parameters $\Delta \mathbf{p}$ using the LM method with the regularisation function yields:

$$\mathcal{H}_{\text{global}} \cdot \Delta \mathbf{p} = \mathcal{J}_{\text{global}}^{\text{T}} \cdot \Delta - \mathcal{L}^{\text{T}} \mathcal{P}. \qquad (2.20)$$

Assuming that the penalizing functions are linear with respect to the inversion parameters, the global Hessian matrix, before applying the Marquardt correction, is constructed as $\mathcal{H}_{\text{global}} = \mathcal{J}_{\text{global}}^{\text{T}} \mathcal{J}_{\text{global}} + \mathcal{L}^{\text{T}} \mathcal{L}$ (for non-linear penalty functions see Appendix B in de la Cruz Rodríguez et al. 2019). The elements of the $\mathcal{L}$ matrix and the penalizing functions vector $\mathcal{P}$ contain a multiplicative factor $\sqrt{c_k}$.

The difficult part of the regularisation method is to find the correct regularisation weight $\mathbf{c}$. Imposing strong regularisation to the inversion parameters causes the regularized merit function to be insensitive to the physical model. Thus, inferred values may not describe the actual physical nature of the solar atmosphere. Conversely, the inversion is hardly regularised if the regularisation weight is low. Specifying the regularisation weight a priori to the inversion is pointless because it depends on the data and the chosen physical model (node positions). It is suggested by de la Cruz Rodríguez et al. (2019) to perform an inversion on a small number of pixels from an observed field of view with different sets of regularisation weights. The regularisation weight for which the penalizing term $\Omega(\mathbf{p}, \mathbf{c})$ and χ^2 are comparable allows for the reliable regularized inference of inversion parameters. In the first few iterations, the minimisation of χ^2_{reg} must be driven by a physical model, while in later iterations, we should also allow for the minimisation of the regularisation function.

The coupled method retrieves the self-consistent solution for the atmospheric and atomic parameters simultaneously without imposing additional approximations not already used in other inversion methods. Due to the method design, it is straightforward to extend it to account for the spatial coupling method from van Noort (2012) and the spatial regularisation from de la Cruz Rodríguez (2019). Fig. 2.2 shows the structure of the global Hessian matrix in an uncoupled case, and in the case of the spatial coupling, spatial regularisation and the coupling in atomic parameters.

Applying the spatial coupling or the spatial regularisation to the atmospheric parameters in the coupled method should also provide a more reliable inference of atmospheric and atomic parameters. However, these extensions will come with significant computational costs and will slow down the inversions significantly. Nevertheless, the primary purpose of the coupled method is to provide reliable atomic parameters, which could be used to infer the atmospheric parameters using any other inversion method.

The coupling of pixels, imposed either using the spatially coupled or the spatial regularisation method, causes the weakening of the inversion parameters cross-talk (de la Cruz Rodríguez 2019). We have arrived at the same conclusion using the coupled method: the coupling of pixels for the inference of atomic parameters improves the reliability of the inferred parameters, not only of atomic parameters but atmospheric ones as well (the results from this test are presented in Sec. 3.2). Coupling of any kind limits the possible values of inversion parameters that are needed to reproduce the observed spectra.
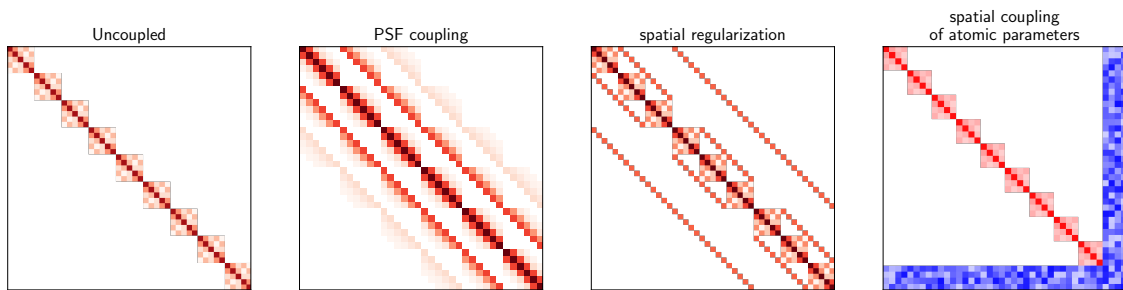
Figure 2.2. Structure of Hessian matrices for different global optimisation methods. *First panel:* The global Hessian matrix in uncoupled case (the pixe-by-pixel method). *Second panel:* Hessian for the PSF coupling of individual pixels from a 6×6 field of view. Each matrix element represents the Jacobian matrix of individual pixels. The shading of each matrix element depicts the strength of the coupling: far-away pixels are much less coupled. *Third panel:* Hessian for the spatial regularisation case. Off diagonal elements represent coupling in inversion parameters using the penalisation functions from Eq. (2.18). Shading depicts the correlation between inversion parameters. *Forth panel:* Hessian for the coupling in atomic line parameters coloured in blue, while atmospheric parameters are coloured in red. Shading of matrix elements has the same meaning as for the spatial regularisation case.

3 `globin`: spectropolarimetric inversion code for the spatially coupled inference of atomic line parameters

The coupled method described in Sec. 2.4.1 is implemented in the new inversion code, named after the method itself as `globin`, which is written in Python and uses the RH code (Uitenbroek 2001) for the spectral synthesis that solves the polarized radiative transfer equation for non-LTE line formation using the multilevel accelerated lambda iteration scheme (Rybicki & Hummer 1991). We opted for the RH code because of its versatility in treating non-LTE line formation, partial frequency redistribution and continuum opacity fudge correction (Bruls et al. 1992). All these features will be necessary for future spectral analysis of many spectral lines (for future application ideas, see Sec. 4).

This chapter describes the necessary input data for the synthesis and inversion of observed data using `globin` and setting the atmospheric parameters on a fine grid and the inversion strategy. We will not discuss in depth the spectral synthesis since it is based on the RH code. The focus will be on `globin` specific parameters, and interested readers and users are advised to consult the RH documentation instead. At the end of the chapter, we present a comparison between the pixel-by-pixel method and the coupled method for retrieving the proper values of atomic parameters from a synthetic spectrum in $4015 - 4017$ Å wavelength range, which contains 18 spectral lines.

3.1   Implementation

The modified version of the RH code used in `globin` is imported as a separate module that uses `Cython` to compile the C files of RH as a Python module. The modifications of the RH code are intended to speed up the spectral synthesis by eliminating all output file creation, allocating the space in the working memory to save the emission and absorption coefficients instead of using files and rewriting the function for computing the spectrum for a specific direction μ (`solveray` executable in RH). All these modifications are performed to preserve all the functionalities of the original RH code and target only the 1D spectral synthesis mode.

The modified version of RH is part of a separate module, which we named `pyrh`. Even though it can be used as a stand-alone Python module for spectral synthesis using RH, it is primarily created to be used within `globin` as a synthesis module.

The `globin` code utilises the multi-threading of PCs and cluster machines using the `multiprocessing` module[1]. The user specifies the number of threads used for spectral synthesis. We have opted for parallelisation of the spatial domain of observations, as it is usually done in all the inversion codes. The RH code parallelises the wavelength domain to speed up spectral synthesis. This feature is obsolete in `pyrh` by hard-coding the number of threads to unity.

The `globin` code has four different modes of operation: synthesis, pixel-by-pixel inference of atmospheric parameters only, pixel-by-pixel inference of atmospheric and atomic parameters, and pixel-by-pixel inference of atmospheric parameters with spatially coupled inference of atomic parameters. We will first introduce the synthesis mode describing the atmospheric model structure and required `globin` input parameters. We will only discuss the necessary parameters for LTE spectral synthesis since the code has yet to be extensively tested for modelling non-LTE spectra. After describing the synthesis mode, we will describe inversion input parameters and inversion-specific methods for constructing the atmospheric model and inferring the inversion parameters.

In synthesis or inversion mode, the control of `globin` is performed through different files with the extension `.input`. Since the `pyrh` is a wrap around the RH code, `globin` still relies on the same input files as RH does. The additional input file named `params.input` contains all the keywords used to control `globin`. A list of all keywords specific to `globin` that can be specified in the `params.input` file is given in Appendix A along with their default values and short descriptions. Throughout the description of synthesis and inversion modes, we will refer only to the most relevant keywords.

3.1.1 Spectral synthesis mode

The spectral synthesis, in general, requires a user to provide an atmospheric model, a list of spectral lines to be synthesized and the wavelength range over which the spectrum is to be computed. The line list is provided in Kurucz format using the keyword `linelist`. The wavelength range is controlled either using keywords `wave_min`, `wave_max` and `wave_step` in Å or providing a file name containing the wavelength grid using a keyword `wave_grid`.

The `globin` code supports reading a 1D model atmosphere in MULTI format (Carlsson 1986) from a text file with an extension `.atmos` or 3D atmospheric model in a FITS file format. Here, we will only describe the atmospheric model given in FITS file format, unique to `globin`, while the 1D MULTI type model is described in the RH documentation.

The default structure of atmospheric model in `globin` has atmospheric parameters in the following order: depth scale, temperature T, electron number density n_e (in cm^{-3}), line of sight velocity v_{LOS} and micro-turbulent velocity v_{mic} (both in km/s), magnetic field strength B (in Gauss), magnetic field inclination θ and azimuth ϕ (both in radians), and the total hydrogen number density (sum of neutral and ionized hydrogen number density; n_H^{tot} in cm^{-3}). The depth scale of the atmospheric model used in RH to compute a spectrum must be either a height scale (in km), a column mass density (in cm^2/g) or the optical depth at 5000 Å[2]. The type of depth scale used for atmospheric parameters stratification

---

[1] https://docs.python.org/3/library/multiprocessing.html

[2] The wavelength of a given optical depth scale can be specified by a user in RH. However, in the following, we will always assume it is set to 5000 Å.

is specified in the header of the FITS file using the keyword SCALE. The shape of an atmospheric model array in the FITS file format is assumed to be (n_x, n_y, n_p, n_z), where n_p is the number of atmospheric parameters.

The globin code also supports the atmospheric models of SPINOR and SIR types that are used accordingly in SPINOR and SIR inversion codes. These atmospheric types can be specified as a 1D model in a text file or using the FITS file with the same shape as globin default type, except having different n_p. The type of atmospheric model provided to globin is specified using the keyword atm_type. When globin loads the atmospheric model, it is internally converted to its default type.

The class Atmosphere() handles all the operations performed on the atmospheric model. It controls the input and output of an atmospheric model, converts between different model types, computes spectra and response functions for given parameters, sets the atmospheric parameters on a finer grid and many less significant operations. By default, globin has access to FAL-C and HSRA atmospheric models that can be used for a quick spectral synthesis. An example of how simple it is to synthesise the spectrum using globin (assuming that the RH specific input files are correctly configured) is given in Listing 3.1.

Listing 3.1. Synthesis example for Hinode lines using globin. This example does not require the use of params.input file.

```
1  import globin
2
3  # read in the atmosphere; we take internally loaded FAL-C
4  atmos = globin.falc
5  # set up the wavelength grid for which to compute spectrum
6  atmos.set_wavelength(lmin=6301, lmax=6303, dlam=0.010, unit="A")
7
8  spec = atmos.compute_spectrum()
```

The computed spectrum is, by default, given in absolute units of W/m^2/Hz/srad. There are three different types of spectral normalisation implemented in globin that are controlled with the keyword norm:

norm = 1: the spectrum continuum is set to unity, where the reference intensity is taken at the first wavelength point in the given pixel.

norm = hsra: the spectrum is normalized with respect to the continuum intensity (at the first wavelength point) from the HSRA atmospheric model.

norm = I_c: the provided I_c value normalizes the synthetic spectra.

The minimal required params.input file for spectral synthesis is shown in Listing 3.2 and the corresponding Python code to synthesise spectra in Listing 3.3.

Listing 3.2. Minimal `params.input` file needed for spectral synthesis.

```
1  # number of threads
2  n_thread = 1
3  # synthesis: mode = 0
4  mode = 0
5  # Gaussian noise level to be added
6  noise = 1e-3
7  # macro-turbulent broadening [km/s]
8  vmac = 1.2
9  # type of spectral normalisation
10 norm = 1
11
12 # \mu value for which to compute the spectrum
13 mu = 1
14 # spectrum output file name
15 spectrum = spec_mu1_hinode_falc.fits
16
17 linelist = hinode_lines
18 wave_min = 6301
19 wave_max = 6303
20 wave_step = 0.010
21
22 # atmospheric model and type
23 cube_atmosphere = falc.dat
24 atm_type = spinor
```

Listing 3.3. Spectral synthesis using the `params.input` file from Listing 3.2

```
1  import globin
2
3  inverter = globin.Inverter(verbose=True)
4  inverter.read_input(run_name="synthesis",
5                      globin_input_name="params.input",
6                      rh_input_name="keyrwords.input")
7  spec = inverter.run()
```

3.1.2   Inversion mode

3.1.2.1   Interpolation of atmospheric parameters

The atmospheric model is parametrized using nodes that contain the absolute values of atmospheric parameters. The node positions must be specified in the optical depth scale only. `globin` currently does not support the node specification on height or column mass scale. The atmospheric parameters inferred from observations and for which the nodes can be specified are T, v_{LOS}, v_{mic}, B, θ and ϕ. The n_e and $n_{\mathrm{H}}^{\mathrm{tot}}$ are calculated assuming that the atmosphere is in hydrostatic equilibrium (more about it in Sec. 3.1.2.2).

   `globin` supports three different methods for the interpolation of atmospheric parameters between nodes: cubic spline interpolation and quadratic and cubic Bézier interpolation (see for example de la Cruz Rodríguez & Piskunov 2013). The usual problem with any interpolation routine is its behaviour at the boundaries of the interpolation domain or in the presence of strong gradients at the node location. The behaviour of both spline and Bézier interpolation at the boundaries is controlled by specifying the first or the second
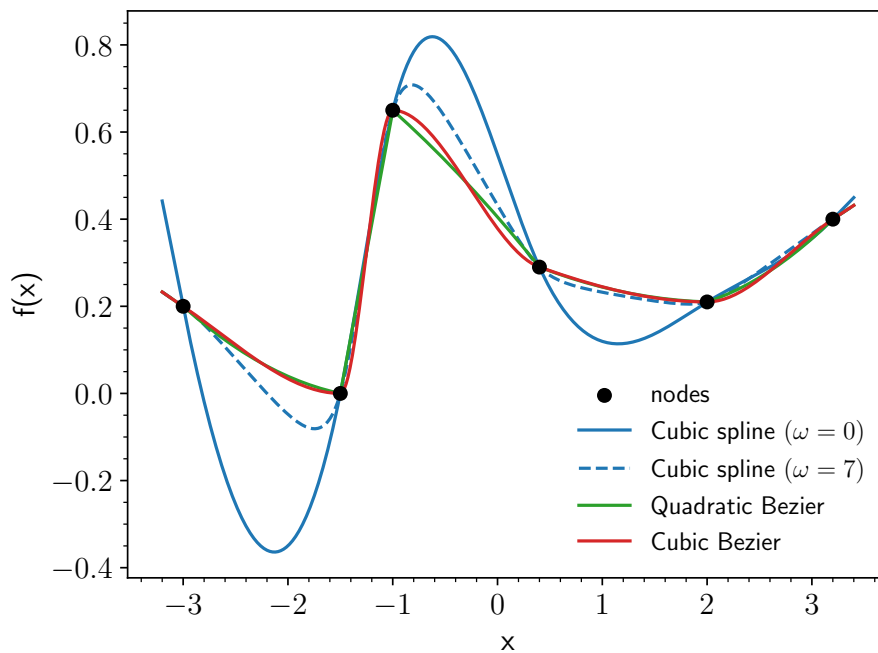
Figure 3.1. Comparison between different interpolation methods implemented in globin.

derivative. The Bézier interpolation is known to be non-overshooting: it does not allow for spurious values when two interpolation nodes are very close and differ significantly. The Bézier interpolation thus handles strong gradients that occur in different atmospheric parameters, characteristic of shocks in the solar atmosphere.

The user can apply the tension factor ω to the cubic spline interpolating polynomial (Schweikert 1966, Cline 1974). The tension factor limits the polynomial overshooting, where the original cubic polynomial is recovered for $\omega = 0$. When the tension factor takes large values (larger than 50), the interpolating polynomial takes the shape of a linear function.

The comparison of different interpolating routines implemented in globin is demonstrated in Fig. 3.1. The overshooting is evident for the cubic spline interpolation when there is a strong gradient in the function $f(x)$, even when a tension factor $\omega = 7$ is applied. We see how all interpolation methods are similar for the nodes at the far right position, which is to be expected when the nodes are well-behaved (far from strong gradients). Also, the quadratic and cubic Bezier interpolation polynomials are comparable in this example.

The interpolation of atmospheric parameters between the nodes is insufficient to construct the atmospheric model and properly synthesize a spectrum. We need to extend our atmospheric model stratification to deeper layers to get the correct continuum intensity and extend the top layers to avoid boundary effects on the line core intensity. Both requirements are related to satisfying the assumption of the semi-infinite atmosphere for the formal solution of the polarized radiative transfer equation. Simply setting nodes at atmospheric boundaries would not help because there is not enough information in a spectrum to determine the atmospheric parameters at these heights accurately.

Extending the atmospheric model to higher and deeper layers requires an extrapolation of atmospheric parameters to the top and bottom boundary of the atmosphere, respectively. By default we assume that the atmosphere spans from $\log \tau_{5000} = 1$ to $\log \tau_{5000} = -6$ at a step size of 0.1. The user can change these values through keywords `logtau_bottom`, `logtau_top` and `logtau_step`. The step size is assumed to be constant throughout the atmosphere.

The atmospheric parameters are linearly extrapolated from the highest node to the top boundary, where electron density and total hydrogen density are estimated assuming the hydrostatic equilibrium. The same procedure is also applied from the deepest node to the bottom boundary. The linear extrapolation assumes the gradient equals the first derivative at the boundary nodes. The only exception is the temperature extrapolation to the bottom boundary, for which we use the temperature gradient from the FAL-C model (Fontenla et al. 1993) at the depth of the deepest node. The same temperature extrapolation routine is implemented in the inversion code `SNAPI`. The temperature extrapolation to the higher layers has a lower limit of 2800 K at the highest point in the atmosphere. The same limit is also imposed on all temperature nodes. For lower temperatures, most hydrogen atoms form H^2 molecule, significantly reducing the population of neutral hydrogen atoms. This affects the continuum opacity contributions, such as from H^- ion, which produces a significantly different continuum level compared to the observed one.

The `globin` code allows for a variable number of nodes to be specified for each atmospheric parameter, and this number can differ from parameter to parameter. There is no exact rule on how many nodes should be chosen for each parameter, and it depends on the type of observations set to be inverted. We expect low polarisation signals for quiet-sun spectra, limiting the information they contain and making it difficult to infer the depth-dependent magnetic field vector. To simplify our models and still have feasible inversions in such a case, we assume that the magnetic field vector is constant with height. Meanwhile, we can set many nodes (say more than 7) for temperature to get the best possible temperature stratification, which significantly impacts the spectral shape of Stokes I. However, the large number of nodes, along with the interpolation routines, can lead to an unrealistic oscillatory solution. Therefore, this problem can be overcome by imposing a depth-dependent regularisation on atmospheric parameters, which allows for increases in the number of nodes and retrieves a better representation of the stratification of atmospheric parameters (de la Cruz Rodríguez et al. 2019). The depth-dependent regularisation term is added to the merit function as was the case for the spatial regularisation in Sec. 2.4.2. Different types of depth-dependent regularisation for the atmospheric parameters are listed and discussed in de la Cruz Rodríguez et al. (2019). The same regularisation type is also implemented in the `SNAPI` code. However, `globin` currently only supports spatial regularisation but not depth-dependent regularisation; the user should be careful about how many nodes are specified for each parameter.

3.1.2.2 Hydrostatic equilibrium

The atmospheric parameters for which we specify nodes are insufficient to compute the spectrum. We also require n_H^{tot} and n_e, which establish the ionisation balance between different atmospheric chemical elements. RH by default considers only those elements for which the abundance is specified in a separate file (using keyword `ABUND_FILE` in

keyword.input file). The n_e is then calculated from the equation of state, and globin uses the ideal gas equation $p_g = (N + n_e)k_BT$ where N is the total number density of atoms (neutral and ionized) that is related to the n_H^{tot} as:

$$n_H^{tot} = \frac{N}{\sum_X 10^{\epsilon_X - 12}}, \tag{3.1}$$

where the summation goes over all atomic elements X that we have in the atmosphere, ϵ_X is the abundance of the chemical element X given in logarithmic scale with respect to the hydrogen abundance ($\epsilon_H = 12$) and the summation is assumed to start from hydrogen atoms. The ideal gas equation contains two unknown and necessary parameters for spectral synthesis, n_e and n_H^{tot}. We assume that the atmosphere is in hydrostatic equilibrium to close the system and solve for them. The gas pressure balance in the atmosphere in the optical depth scale at 5000 Å is:

$$\frac{dP_g}{d\tau^C} = \frac{g\rho}{\chi^C}, \tag{3.2}$$

where ρ is the mass density, χ^C is the continuum absorption coefficient at 5000 Å and g is the surface gravity acceleration. Considering that our atmospheric model includes only the photospheric and chromospheric layers, it is safe to assume that g is constant throughout the solar atmosphere because it is very thin compared to the solar diameter. Also, Eq. (3.2) assumes that the radiation pressure does not contribute significantly to the pressure balance because of the comparatively low solar luminosity. Thus, the radiation pressure is important for much brighter stars of spectral classes O, B and A (Gray 2008). We also chose to ignore the contribution of turbulent and magnetic pressure, which would significantly increase the complexity of inversions. The magneto-hydrostatic equilibrium is solved in the FIRTEZ-dz inversion code (Pastor Yabar et al. 2019). It is currently the only inversion code that infers the atmospheric parameters on a height scale. Every other code uses either the optical depth scale or column mass density.

The atmospheric density is given by the equation:

$$\rho = m_0 \sum_X A_X n_X, \tag{3.3}$$

where m_0 is the atomic mass unit, A_X is the atomic mass of an element X, and n_X is its total number density (sum of neutral and all possible ionisation states). Under the LTE approximation, n_X is computed from the Saha equation by considering all possible ionisation stages of the element X.

The hydrostatic equilibrium equation (HSE) is solved by integration from the top, assuming that the atmospheric temperature is known. Given the p_g^{top} at the top of the atmosphere, we calculate the initial n_H^{tot} from the ideal gas equation assuming that $n_e = 0$. With the initial n_H^{tot}, we calculate the n_e to satisfy the ionisation balance based on the specified chemical composition of the atmosphere. With the updated value for n_e, we recalculate the n_H^{tot} with the same p_g^{top} and repeat the process until the relative change of n_H^{tot} drops below 10^{-2}. With the updated n_H^{tot} and n_e, we calculate the ρ and χ^C at the top of the atmosphere.

The n_e and n_H^{tot} in the next atmospheric depth are calculated from the HSE, and the n_e and n_H^{tot} from the previous depth point, or to be exact from the ρ and χ^C since they appear

in Eq. (3.2). The HSE integration is then performed on the logarithmic optical depth scale using the trapezoid integration method:

$$
\begin{aligned}
\beta_1 &= \frac{\rho_{k-1}}{\chi_{k-1}^c} \tau_{k-1} \\
\beta_2 &= \frac{\rho_k}{\chi_k^c} \tau_k \\
p_{g,k} &= p_{g,k-1} + \ln(10) \cdot g \cdot \frac{\beta_2 + \beta_1}{2} \cdot \log\left(\frac{\tau_k}{\tau_{k-1}}\right),
\end{aligned}
\tag{3.4}
$$

until the relative change of $p_{g,k}$ is smaller than 10^{-2}. The k index indicates the depth position and the atmospheric parameters in `globin` are stratified from the top of the atmosphere ($k = 0$) to the deepest layers ($k = N_d$). Integrating the HSE on the logarithmic optical depth scale increases the stability of the iterative method, and only a few iteration steps (2-3) are needed for convergence (Gray 2008).

3.1.2.3 Parameters response functions

`globin` uses the central difference numerical scheme to compute the response functions of parameters in the nodes. The perturbations are applied to the node values, which require us to re-interpolate and re-extrapolate atmospheric parameters to solve the polarized radiative transfer equation. The magnitude of the perturbation applied to each inversion parameter is given in Tab. 3.1. These perturbation values are chosen to be small enough to approximate the response functions as a first-order perturbation of the Stokes profiles but large enough to produce differences in the spectra that are significantly larger than any numerical uncertainty. With much larger perturbations of the physical parameters, we would reach a non-linear perturbation of the Stokes profiles due to the non-linearity of the polarized radiative transfer equation.

Table 3.1. The parameter perturbations δp used for computing numerical response functions.

parameter	perturbation
T	1 K
v_{LOS}	1 m/s
v_{mic}	1 m/s
B	1 G
θ	0.01 rad
ϕ	0.01 rad
$\log(gf)$	0.001
$\Delta\lambda$	1 mÅ

The values of the response functions for different physical parameters span several orders of magnitude (see Fig. 2.1), which impacts the convergence properties of the LM algorithm. To improve the convergence of the inversion, Marquardt (1963) suggested

scaling the k–th column of the Jacobian matrix (in our case, the response functions to the k–th inversion parameter) with:

$$s_k = \sqrt{\sum_{i=1}^{N} \mathcal{J}_{i,k}^2}, \qquad (3.5)$$

where the index i goes over all data points (in our case, wavelengths for all four Stokes components). Dividing the computed response function with this scaling parameter yields a dimensionless response function. The Hessian matrix becomes a matrix of parameter correlation coefficients (diagonal elements equal $1 + \lambda_{\mathrm{M}}$). The parameter correction Δp_k can be converted back to proper units by multiplying it with the s_k.

The response functions for atomic parameters are also computed similarly to those for the atmospheric parameters using the central difference numerical scheme. However, their computation using the perturbation method is much simpler than the atmospheric parameters because the atomic parameters are height-independent. In the case of the $\log(gf)$ parameter, the perturbations of the absorption and emission coefficients are simply $\delta\chi_\lambda = \chi_\lambda^L \cdot \ln(10) \cdot \delta\log(gf)$ and $\delta\eta_\lambda = \eta_\lambda^L \cdot \ln(10) \cdot \delta\log(gf)$. In future versions of `globin`, we intend to implement the perturbation method for computing the response functions of atomic line parameters, which should decrease the inversion time.

3.2 Comparison of the pixel-by-pixel and the coupled methods for atomic line parameters inference

Material from this section is presented in the paper Vukadinović et al. (2023) that is submitted to A&A journal. I have conducted all the tests, compiled all the figures and wrote the manuscript draft that has been corrected by all co-authors.

To test the capabilities of the coupled method in comparison to the pixel-by-pixel method, we analyse synthetic Stokes profiles sampling different features. We extract atmospheres of an umbra, penumbra, granule and intergranular lane from a snapshot of a 3D MHD simulation containing a sunspot (Rempel 2012, see the continuum image in Fig. 3.2d) simulated using the MURaM code (Vögler et al. 2005). This selection guarantees a diverse sample of temperature, line of sight (LOS) velocity and magnetic field strength stratifications (Fig. 3.2a-c) resulting in very different Stokes profiles (Fig. 3.2e-h). This diversity leads to line profiles, especially of weaker lines, that are prominent in some features but not visible in others. In particular, the response of lines to a change in the atomic parameters is different for the different atmospheres, naturally reducing the cross-talk between atomic and atmospheric parameters in the coupled method.

We will test the applicability of the pixel-by-pixel method and the coupled method to determine the atomic parameters $\log(gf)$ and to correct for possible errors in the central wavelength ($\Delta\lambda$) of spectral lines in the 4015–4017 Å range, containing several blended lines. This spectral region was chosen because it is within the range of the Hamburg atlas spectrum (Neckel & Labs 1984), has many blended spectral lines, and is accessible to the SUSI instrument.

Spectral line information for the considered spectral region is taken from the Kurucz line list (Kurucz & Bell 1995). Many lines in the Kurucz line list are relatively weak

Table 3.2. Atomic line parameters from 4015–4017 Å range. The columns represent line number in the spectral region used for analysis, chemical element, central wavelength λ_0, energy of lower level (E_i), blending factor b, effective Landé factor (g_{eff}), element abundance α and $\log(gf)_0$ parameter. All atomic data are from Kurucz's database, except for the Landé factor and abundances. The effective Landé factors are taken from the VALD database, where only line 10 is computed assuming LS coupling. [a]Grevesse & Anders (1991) [b]Asplund et al. (2000) [c]Anders & Grevesse (1989).

No	element	λ_0 [Å]	E_i [eV]	b [%]	g_{eff}	α	$\log(gf)_0$
1	Fe I	4015.139	4.1631	4.3	0.666	7.44[b]	-2.172
2	Co I	4015.219	2.7849	33.3	0.484	4.92[a]	-1.806
3	Ti I	4015.373	2.0850	20.7	0.515	4.99[a]	-0.084
4	V I	4015.398	2.0618	98.4	0.995	4.00[a]	-0.857
5	Fe I	4015.465	4.0434	33.1	1.407	7.44[b]	-0.781
6	Ni II	4015.474	3.9028	99.4	0.619	6.25[a]	-2.419
7	Nd II	4015.545	1.6766	94.1	0.886	1.50[c]	0.080
8	Fe I	4015.605	4.0434	5.1	1.394	7.44[b]	-0.515
9	Ce II	4015.875	1.0083	21.7	0.881	1.55[c]	-0.087
10	Fe I	4015.986	4.1235	3.8	2.000	7.44[b]	-1.928
11	Ni I	4016.068	3.9735	20.1	1.388	6.25[a]	-1.870
12	Ti I	4016.274	2.0658	5.8	1.762	4.99[a]	-0.714
13	Fe I	4016.419	3.1775	0.1	0.682	7.44[b]	-1.600
14	Fe I	4016.541	2.6399	5.5	1.197	7.44[b]	-3.513
15	Mn I	4016.658	4.1926	53.5	0.035	5.39[a]	-1.160
16	Co II	4016.685	3.0177	41.6	1.293	4.92[a]	-2.905
17	Fe I	4016.792	4.1195	65.9	2.002	7.44[b]	-2.576
18	Co I	4016.793	3.5124	39.5	1.213	4.92[a]	-0.547

and are expected to have an insignificant effect on the spectrum. Including all of them will only extend the computing time. We consider only those spectral lines with a line core depth of at least 1% of the local continuum intensity. We found 18 such lines in this region. Their parameters are given in Tab. 3.2. The blending factor for each line is estimated using the method in Laverick et al. (2017). This factor quantifies the extent of overlap between a given absorption line's core and its neighbouring lines. The smaller the blending factor is, the smaller the amount of overlap.

The Stokes profiles are computed at disk centre ($\mu = 1$) under the LTE approximation using `globin`. The computed spectra are normalized using the continuum intensity computed from the HSRA atmospheric model[3] (Gingerich et al. 1971). The differences between the coupled and pixel-by-pixel methods are tested under ideal conditions by disregarding observational effects such as stray light, the finite resolving power of spectrographs and noise.

In the inversion, we fitted for the height stratification of the atmospheric parameters:

---

[3]Any other mean atmospheric model, such as FAL-C or HOLMUL, could be used to compute the continuum intensity.
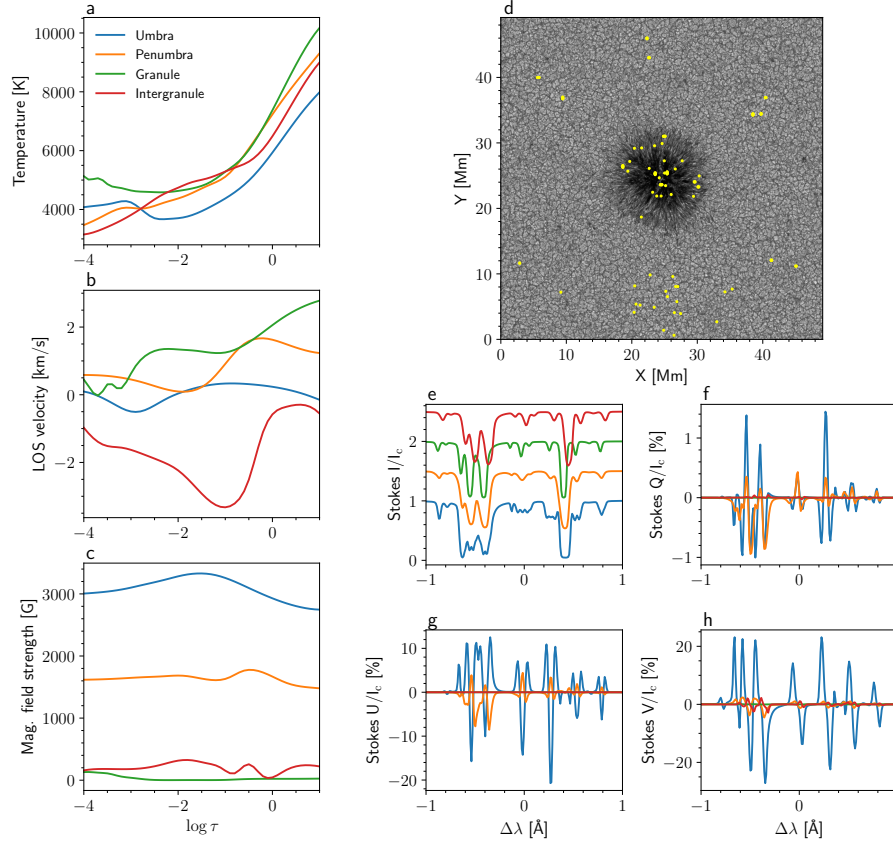
Figure 3.2. *Panels a-c:* Stratifications of the temperature (a), LOS velocity (b), and
magnetic field strength (c) from one pixel for each atmospheric feature taken from
the sample of extracted atmospheres. *Panel d:* the continuum intensity from the
MHD cube at 4015 Å. Yellow dots represent selected pixels of the umbra, penumbra,
granule and intergranular lanes used for testing the coupled method. *Panels e-h:*
Stokes parameters in the 4015–4017 Å spectral range from the atmospheres displayed
in panels a-c. Wavelengths are given with respect to 4016 Å. For easier comparison,
the Stokes profiles are normalized to the local continuum intensity I_c and the Stokes
I/I_c profiles from different features are shifted vertically.

temperature, LOS velocity, and magnetic field vector. The temperature is inferred using
four nodes placed at optical depth values of $\log \tau = (-2.5, -1.5, -0.5, 0.4)$ while the re-
maining atmospheric parameters are inferred at three nodes, $\log \tau = (-2.2, -1.1, 0)$. Here
and in the rest of the paper, the optical depth scale is computed at the reference wave-
length of 5000 Å. The initial values for the atmospheric parameters are uniform across all
pixels.

We considered $\log(gf)$ and the central wavelength shift $\Delta\lambda$ of all lines as free pa-
rameters, except for line 13, whose parameters were kept fixed during inversions in both
the pixel-to-pixel method and the coupled method. Line 13 is the strongest and the least
blended within the spectral range. Fixing the atomic parameters of one spectral line is nec-
essary to infer both the absolute wavelength and LOS velocity accurately. Additionally,
it improves the inference reliability of atomic parameters for other lines in the spectral
region.

Initial atomic parameter values are randomized with a Gaussian distribution around the exact values (i.e., the values used for computing the synthetic spectra from the simulations) with a standard deviation of 0.2 for $\log(gf)$ and 5 mÅ for the $\Delta\lambda$ parameter. We limit the allowed ranges for $\log(gf)$ and $\Delta\lambda$ to $[-2.0, 1.5]$ and $[-30, 22]$ mÅ with respect to the exact values, respectively. These limits are in the range of the expected uncertainties in the atomic databases and can be independently adjusted for each spectral line.

To compare results from the coupled method with the pixel-by-pixel method, we performed the inversions in three different modes:

Mode 1: Only atmospheric parameters are inverted for each pixel individually. The atomic parameters are fixed to the values used to compute the reference spectra. This inversion allows us to retrieve the best possible stratification of atmospheric parameters with the given node settings and initial parameter values since all atomic parameters are assumed to be accurately known.

Mode 2: For each pixel individually, atomic and atmospheric parameters are inferred (pixel-by-pixel method). Here, the inversion retrieves different atomic parameters for every spectral line and at every pixel.

Mode 3: Atmospheric parameters vary between pixels, while atomic parameters are inverted globally (i.e. the coupled method). Only one set of atomic parameters ($\log(gf)$ and $\Delta\lambda$) is obtained per spectral line.

Mode 1 inversion results are used as a reference to which the inversion results from mode 2 and 3 are compared. Any significant deviations in the retrieved atmospheric parameters in mode 2 and 3 compared to the retrieved atmospheric parameters in mode 1 can likely be attributed to the poor atomic parameters in these two modes, resulting in poor convergence.

All three modes were run with the same initial values of the atmospheric parameters and the same initial atomic parameters in mode 2 and 3. For mode 2 and mode 3 inversions, we observed that the LM algorithm converges in more pixels when a large value of the Marquardt parameter ($\lambda_M = 10$) is used at the start. This leads to small changes in the free parameters at the start of the inversion, thus improving the convergence properties of the algorithm.

The χ^2 values for all selected atmospheres (referred to as pixels from now on) from all three modes are displayed in Fig. 3.3. For a direct comparison, χ^2 is calculated as:

$$\chi^2 = \frac{1}{N} \sum_{i=1}^{N} w_i^2 \, (\mathbf{O}_i - \mathbf{S}_i)^2 \,, \tag{3.6}$$

where N is the number of wavelengths (running over each Stokes parameter), w_i is the weighting of each Stokes component and each wavelength, $\mathbf{O}$ is a synthetic Stokes spectrum from selected pixels and $\mathbf{S}$ is an inverted Stokes spectrum. Both $\mathbf{O}$ and $\mathbf{S}$ are normalized to the local Stokes I continuum value. The exact weights were used in all three modes.

Note that pixels in Fig. 3.3 are not spatially connected (yellow dots in Fig. 3.2d). Inversion mode 1 shows a low χ^2 value for pixels within the granules, whereas the umbral
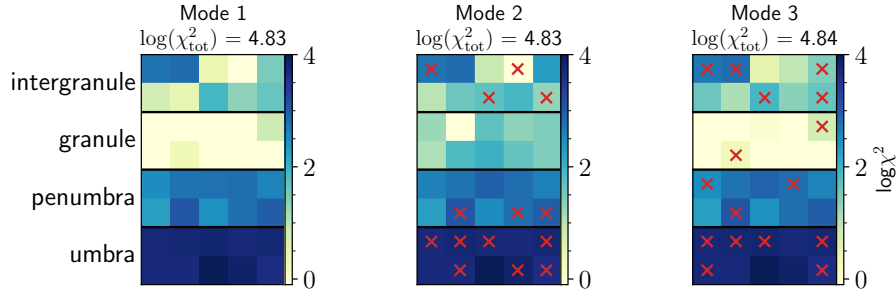
Figure 3.3. χ^2 values for all three modes on a logarithmic scale. The total χ^2 value, the sum of the χ^2 values from all pixels, is displayed at the top of each panel. Pixels marked with a red cross in panels of mode 2 and 3 correspond to pixels with a lower χ^2 than the χ^2 value in mode 1.

and penumbral pixels show higher values. The convergence to lower χ^2 in these pixels could be improved by changing the initial parameters or the LM algorithm's parameters. However, this does not guarantee that the χ^2 value in other pixels would also improve simultaneously.

The inversion mode 2 and 3 show a very good fit to the Stokes spectra, comparable to mode 1, with slight differences in individual pixels. Those pixels in mode 2 and 3 with χ^2 value lower than in mode 1 are marked with red crosses in Fig. 3.3. With a larger number of inversion parameters, the inversion algorithm has much more freedom to find the best match of spectra, thus lowering the χ^2 hypersurface.

The quality of the inferred atmospheric parameters for all three inversion modes is quantified using the root-mean-square-deviation (RMSD). The parameter's RMSD (P_{RMSD}) is defined as the root-mean-square difference between the retrieved parameter stratification (P_{inv}) and the original parameter stratification in the MHD cube (P_{MHD}) at all depths between the highest and lowest nodes on the interpolated $\log \tau$ grid:

$$P_{\mathrm{RMSD}} = \sqrt{\frac{1}{N_{\mathrm{d}}} \sum_{i=1}^{N_{\mathrm{d}}} (P_{\mathrm{inv}_i} - P_{\mathrm{MHD}_i})^2}, \tag{3.7}$$

where N_{d} is the number of fine grid points in the atmosphere between the lowest and the highest node of the parameter P. The extrapolated depth points above the highest and below the deepest node were excluded from the computation of the P_{RMSD} to focus on the region of the atmospheres where the lines are formed.

The P_{RMSD} values for the temperature, LOS velocity and magnetic field strength for each pixel are displayed in Fig. 3.4. The first column shows the P_{RMSD} for mode 1 while the last two columns display the differences in P_{RMSD} for mode 2 and 3 relative to mode 1 (ΔP_{RMSD} value). Negative differences indicate a better retrieval of atmospheric parameters in mode 2 and 3 compared to the atmospheric parameters retrieved in mode 1. Overall, mode 3 shows a better retrieval of atmospheric parameters (despite the fact that mode 3 has fewer free parameters!) compared to mode 2 and the values retrieved are comparable to mode 1 inversion results.

In the case of granular and intergranular pixels in mode 2, the achieved fit quality is comparable to mode 1, but the temperature stratification differs significantly from the
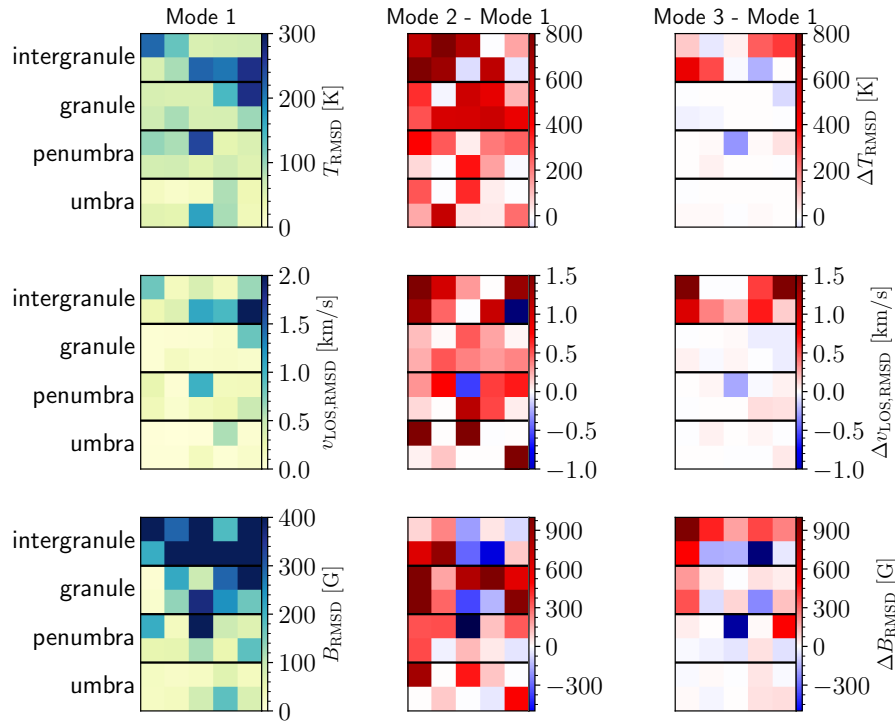
Figure 3.4. The root-mean-square deviation of the inverted atmospheric parameters calculated from the highest to the lowest nodes in each inversion mode. The first column shows the P_{RMSD} for mode 1, while the other two columns display differences in P_{RMSD} from mode 2 and mode 3 from mode 1. The P_{RMSD} measures are given for temperature (first row), LOS velocity (second row) and the magnetic field strength (third row).

reference case (mode 1). The temperature offset can be compensated for by adjusting the $\log(gf)$ value (and to a minor extent also any other inversion parameter), resulting in large errors in the inversion parameters but still maintaining a satisfactory fit to the Stokes profiles or even producing a better one. This is possible because the four-node representation of the temperature used in the inversions cannot accurately represent the more complex height stratification in the MHD atmospheres. The comparison of retrieved parameter stratifications in all three modes to the MHD stratification for a granule atmosphere is displayed in Fig. 3.5. This figure exemplifies the highly complex stratifications typically found in MHD simulations. The corresponding synthetic Stokes spectra and the best fit for the three modes are displayed in Fig. 3.6, where mode 3 shows the best fit to the observed spectra.

To illustrate the quality of the temperature and $\log(gf)$ retrieval for mode 2 and 3 inversions, we present scatter plots of the ΔT_{RMSD} values for every atmosphere and the difference between the inverted and exact values of the $\log(gf)$ parameter for every line in Fig. 3.7. The large scatter of retrieved $\log(gf)$ values in mode 2 is evident. There are two reasons for this behaviour. The first one is a consequence of the blending of spectral lines. In the case of line blends, the mode 2 inversions cannot differentiate the contributions of each blended line to the final profile. This example illustrates the demerits of assuming a statistically averaged value of $\log(gf)$ from all the pixels to be the right one for the given
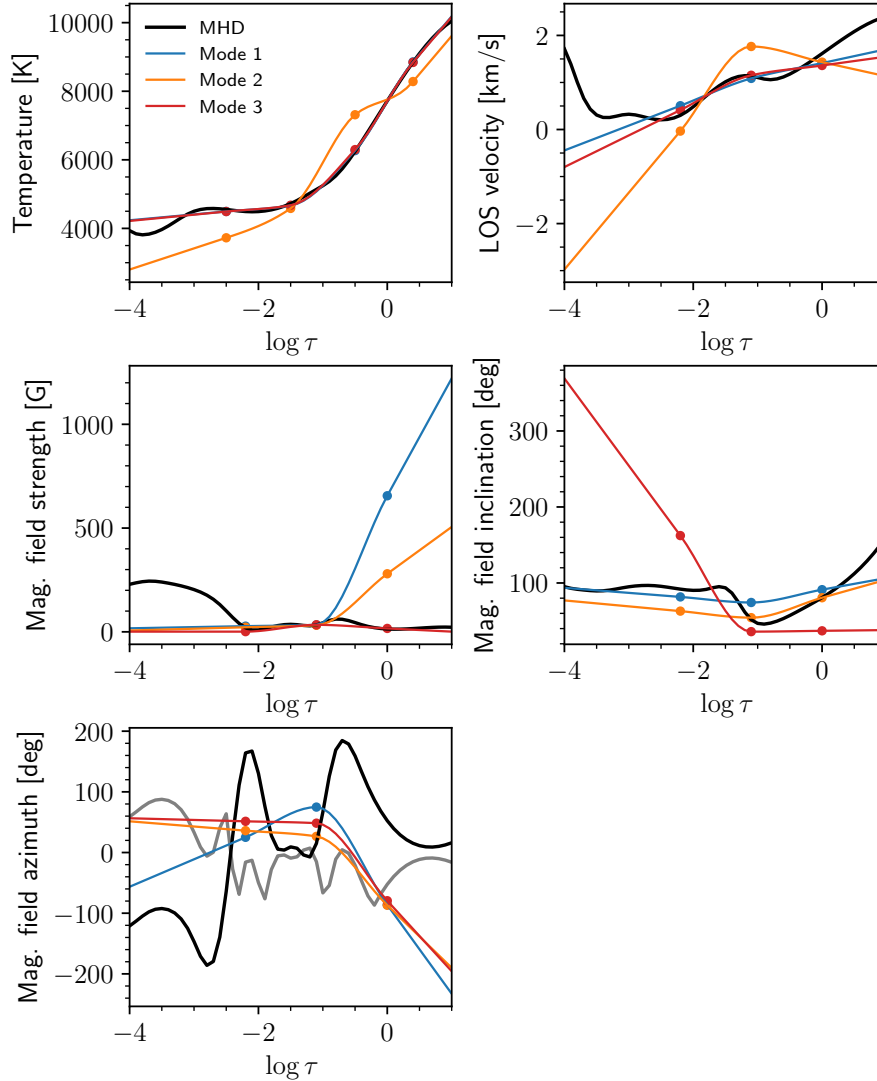
Figure 3.5. Stratifications of various atmospheric parameters for a granule atmosphere. Curves with different colours represent the stratification of the original MHD simulation and different inversion modes (see legend in the top-left panel). Circles represent the node positions. The grey line in the azimuth panel shows the azimuth in MHD simulation shifted by 180°.
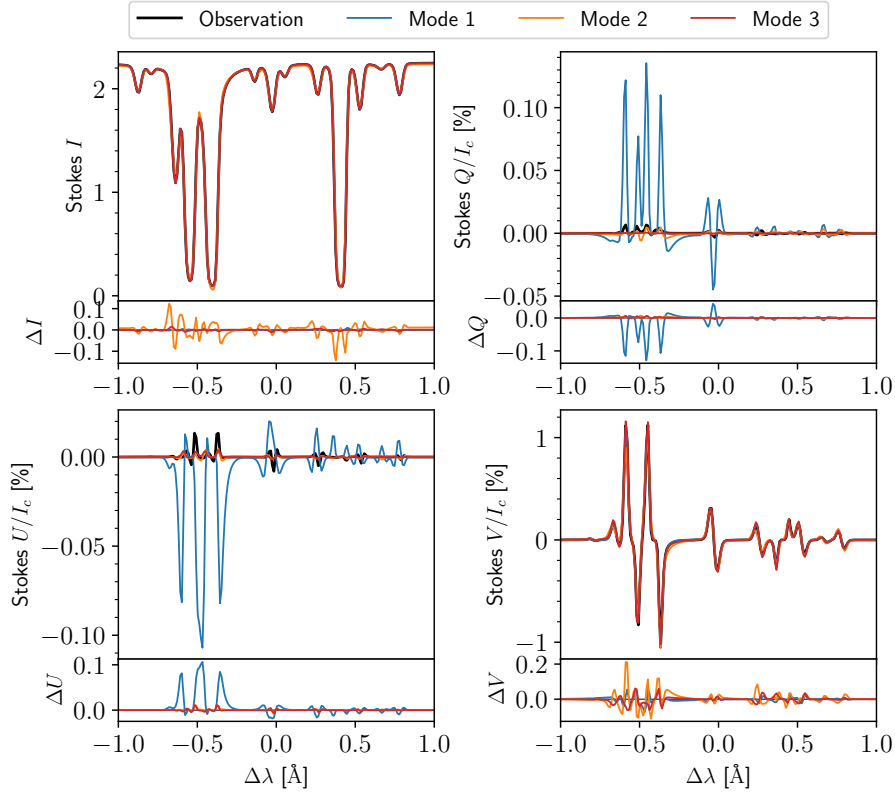
Figure 3.6. The comparison of Stokes spectra in all inversion modes for a granule atmosphere whose atmospheric stratification is displayed in Fig. 3.5.

spectral line in the pixel-by-pixel method. The second possible explanation could be because of the degeneracy in mode 2 between the temperature and $\log(gf)$ retrieval: the $\log(gf)$ values for all the spectral lines can be freely modified along with the atmospheric parameters in every pixel individually and thus relaxes the constraints on the temperature. The magnitude of this degeneracy on the retrieved inversion parameters is unclear from this test since all the lines are somewhat blended. However, using the same inversion setup, mode 3 manages to overcome these difficulties and retrieve $\log(gf)$ values very close to the exact values for all spectral lines and stratification of atmospheric parameters in each pixel.

The comparison between retrieved $\log(gf)_{\mathrm{inv}}$ in mode 2 and 3 and the $\log(gf)_0$ is shown in Fig. 3.8. The mode 2 results represent the mean value from the $\log(gf)$ values of all considered pixels. This improves the statistical significance for the mode 2 results and allows for a fair comparison with the mode 3 results, which always considers all the pixels. A preliminary analysis shows that an insignificant improvement in the results from mode 2 is achieved by increasing the number of pixels. Also, the optimal number of pixels required for each mode will depend on the number of lines for which the atomic parameters are to be determined and the amount of line blending. The influence of the chosen number of pixels on the results from both modes, 2 and 3, will be investigated in detail in a follow-up study.

As a measure of the quality of the $\log(gf)$ inference for mode 2, we use the mean and the standard error of the $\log(gf)_{\mathrm{inv}}$ - $\log(gf)_0$. The mode 2 inversion manages to retrieve
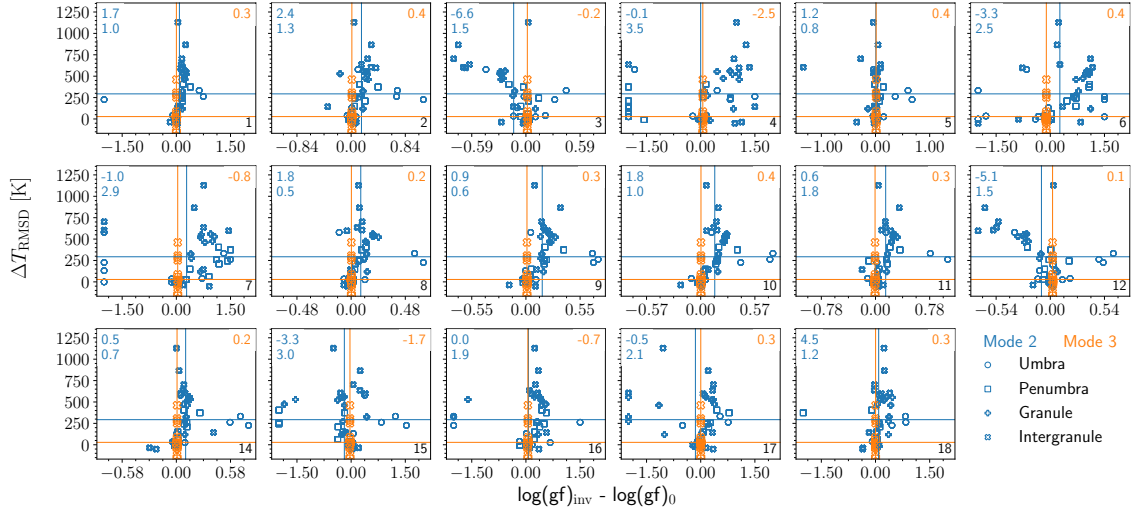
Figure 3.7. Scatter plots of the $\log(gf)_{\text{inv}}$-$\log(gf)_0$ (x-axis) versus ΔT_{RMSD} values (y-axis) for mode 2 (in blue) and mode 3 (in orange). Each subplot corresponds to one spectral line with the line number from Tab. 3.2 given in the lower-right corner. The values from each pixel are represented with different symbols: circle (umbra), square (penumbra), plus (granule) and cross (intergranule). Horizontal and vertical lines mark the average of ΔT_{RMSD} and $\log(gf)_{\text{inv}}$-$\log(gf)_0$ in each inversion mode, respectively. The values in the upper left corner of each panel are the mean and standard error of $\Delta\lambda$ in mode 2, and in the upper right corner is the inferred $\Delta\lambda$ in mode 3 in units of mÅ. The standard error of $\Delta\lambda$ is zero in mode 3 since it retrieves a unique global value.

the $\log(gf)$ values to an accuracy of 0.032 of the exact value, while mode 3 performs better, with an accuracy of only 0.009. The standard error of $\Delta\lambda$ is below 1 mÅ for both modes.

Spectral line 4 has the largest standard error of $\log(gf)$ in mode 2 and the mean $\log(gf)$ close to the expected value (Fig. 3.8, see also Fig. 3.7). This is likely a result of the severe blending with line 3: changes in $\log(gf)$ of line 4 will not produce a significant signature in the spectrum, which hinders the inversion in retrieving a reliable value. A similar situation also holds for line 7, which forms a blend with line 8. Fig. 3.7 shows that the uncertainty of the central wavelength of the spectral line can have a significant impact on the retrieval of the exact $\log(gf)$ value, seen especially in line 4.

The problem in retrieving atomic parameters caused by the blending of spectral lines is illustrated by comparing the results for lines 15 and 16. Fig. 3.8 shows that line 15 is weaker while line 16 is stronger than expected in mode 2. However, line 15 also shifts to shorter wavelengths, further away from line 16. R The inversion algorithm decreases the $\log(gf)$ of line 15 and increases it for line 16 to reproduce the synthetic profile. This interplay between the $\log(gf)$ values of these lines is visible in Fig. 3.7. This problem is alleviated in mode 3, where no such significant difference in retrieved $\log(gf)$ or $\Delta\lambda$ is observed. A similar explanation for the strongly blended pair of lines 17 and 18 also holds. This result clearly shows the benefits of using the coupled method to retrieve reliable atomic parameters compared to the pixel-by-pixel method for blended lines.

The coupled method retrieved atmospheric parameters, $\log(gf)$ and $\Delta\lambda$ with high pre-

cision, whereas the pixel-by-pixel method shows a significant deviation in the temperature and $\log(gf)$ from the reference values. This deviation is due to the blending of spectral lines and, to some extent, to the cross-talk between inversion parameters (mainly between temperature and $\log(gf)$ and $\log(gf)$ and $\Delta\lambda$). The pixel-by-pixel method cannot decouple line contributions to blended profiles, thus inferring erroneous parameter values.

The coupled method can separate contributions of blended line profiles and retrieve accurate $\log(gf)$ values for every line, including heavily blended lines. This result is significant for analysing many-line spectropolarimetric observations, such as the near ultraviolet spectra expected from the SUSI instrument of the Sunrise III observatory. The high density of lines in this spectral region results in line blending. Additionally, many of them have considerable uncertainties in the knowledge of the atomic parameters.
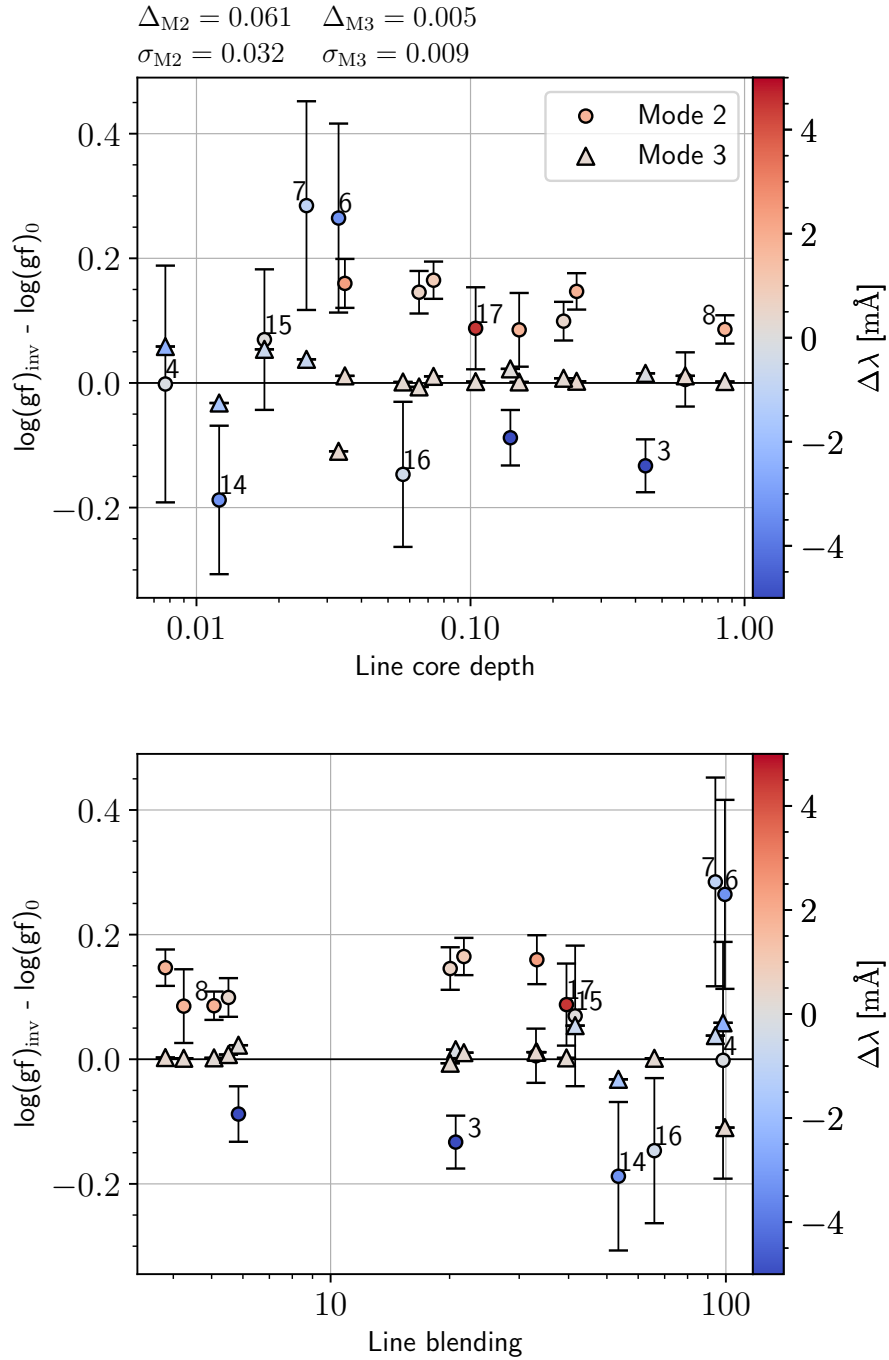
Figure 3.8. Comparison of the atomic parameters $\log(gf)$ and $\Delta\lambda$ for mode 2 and 3 inversions. *Top panel:* The *y*-axis shows the difference between inferred $\log(gf)_{\text{inv}}$ and exact $\log(gf)_0$ values where on the *x*-axis we plotted the line core depth. The averaged values in mode 2 are marked in circles, and the values from mode 3 are in triangles. Markers are coloured based on the $\Delta\lambda$ parameter. The top of the panel lists mean Δ and standard error σ of $\log(gf)_{\text{inv}}$ - $\log(gf)_0$ for each mode. The error bars are displayed only for mode 2, marking 1σ level. Mode 3 retrieves a unique global value for each line, and we do not have any measure of error in this case. *Bottom panel:* The comparison of $\log(gf)_{\text{inv}}$-$\log(gf)_0$ with the line blending factor listed in Tab. 3.2. The markers' shape and colour have the same meaning as in the top panel.

4 Applications of the coupled method

This section presents preliminary results from a test phase of the `globin` code. During these tests, we aimed to verify the reliability of the coupled method and optimize for the best approach which would provide reliable atomic parameters. Some new ideas for applying the coupled method also came into perspective, which are also discussed here.

4.1 The $\log(gf)$ parameter of Fe I 6301.5 Å and 6302.5 Å lines

The first test of the `globin` code, as well as of the coupled method on spatially resolved observations, was conducted on a dataset recorded by the Hinode spacecraft (Kosugi et al. 2007) using the onboard spectropolarimeter (SP; Ichimoto et al. 2008). The Hinode/SP instrument records the Stokes profiles in two Fe I lines at 6301.5 Å and 6302.5 Å with a spectral sampling of 21.5 mÅ. The analyzed data were recorded close to the disc centre with the centre of the scan at $(-28.36'', 7.34'')$ on the 12th of September 2013 from 10:26 to 10:37 UT in fast mode with a spatial sampling of $0.32''$. We selected a region of 20×20 pixels from this dataset with the lowest total polarisation signal and a size of ~ 4.6 Mm (Fig. 4.1).

The atomic parameters of the observed two iron lines are given in Tab. 4.1. The $\log(gf)$ values listed in this table are used as initial values for the inversions. As a first assumption, we presume that both lines can be modelled correctly in LTE even though Smitha et al. (2020) showed that line scattering and UV-overionisation of iron significantly influence the line absorption coefficient and that NLTE solution is preferred.

Table 4.1. Atomic parameters of the two iron lines observed by the Hinode/SP, taken from the VALD database. Listed from left to right are the line central wavelength, the energy of the lower transition level, $\log(gf)$ and the effective Landé factor. We assume a value of 7.44 for the iron abundance (Asplund et al. 2000).

λ [Å]	E_i [eV]	$\log(gf)$	g_{eff}
6301.5002	3.6536	-0.718	1.67
6302.4936	3.6863	-0.968	2.49

For the inversion of Hinode/SP observations, we chose to infer the atmospheric parameters and the $\log(gf)$ parameter, assuming that the central wavelengths of the lines are known. The atmospheric model is parametrized using three nodes at $\log \tau = (-2.0, -0.8, 0.0)$ for temperature, LOS velocity, and magnetic field strength, inclination and azimuth. Even
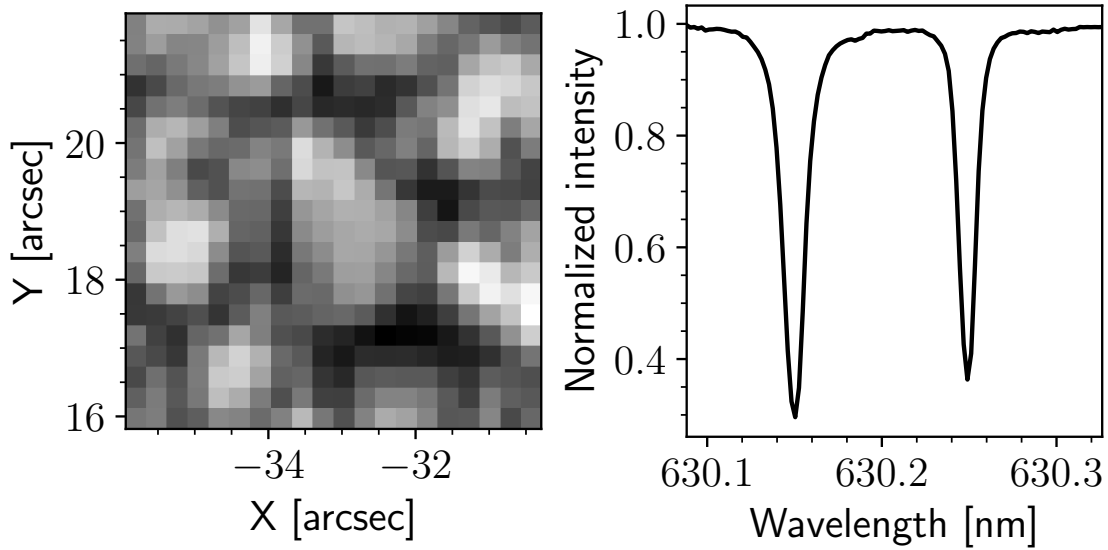
Figure 4.1. *Left panel:* The continuum image of the selected 20×20-pixel region from the quiet-sun disc centre observations by the Hinode/SP instrument on the 12th of September 2013. *Right panel:* The spatially averaged Stokes *I* spectrum from the region in the left panel.

though the observed region is expected to have a weak magnetic field, we opted to infer the depth-dependent magnetic field vector. The Stokes profiles measured in some pixels show polarisation signals above the noise level, and disregarding the magnetic field and its gradient will hinder the inversion algorithm from finding a good fit. Also, the magnetic field can still affect the line profiles in Stokes *I* through the Zeeman effect.

Here, we decided to disregard the micro-turbulent velocity because it causes a poorer fit quality. A similar behaviour was also found to be true when the same data were analyzed using the SPINOR code to which we have benchmarked globin's performance. To carry out a meaningful comparison of inversion results from SPINOR and globin, we had to ensure that both codes use the same node positions, interpolation routine, atomic parameters and the continuum intensity used to normalize the spectra. Therefore, we opted for cubic spline interpolation, also implemented in SPINOR, with the tension factor of $\omega = 5$. In this benchmark test, both codes use the pixel-by-pixel method to optimize for the inversion parameters, assuming constant atomic parameters given in Tab. 4.1. From the comparison of inferred atmospheres in Fig. 4.2, we conclude that both codes show a comparable spatial distribution of inversion parameters in each node. This indicates that the physics implemented in globin is correct and behaves as expected. Even though the spatial regularisation is implemented in globin, we are not using it in these inversions because it is unavailable in SPINOR and could cause larger discrepancies between retrieved atmospheres from these two codes.

Next, we apply the coupled method to the same dataset to infer the $\log(gf)$ values of both lines. The $\log(gf)$ parameter of the 6301.5 Å line has been measured in the laboratory using the emission measure technique with a relative error of 7% (Bard et al. 1991). Even though it is experimentally measured, we assumed that it is unknown and tested whether the coupled method can reliably retrieve this value along with the $\log(gf)$
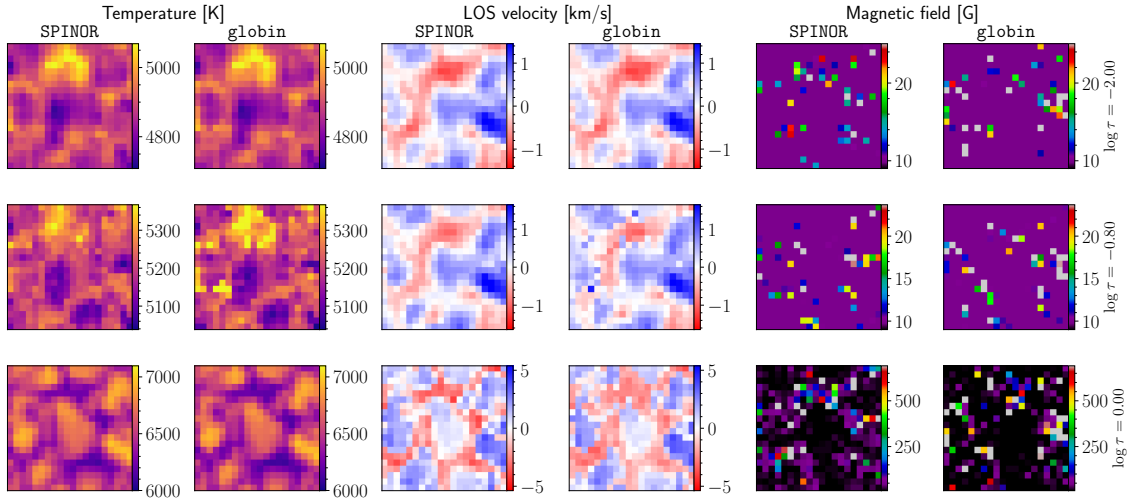
Figure 4.2. Comparison of inferred values for temperature (first two columns), LOS velocity (third and fourth columns) and magnetic field strength (last two columns) from SPINOR and globin. Each row represents the spatial distribution of inferred values at a given node.

parameter of 6302.5 Å line. Therefore, we have performed three different inversions:

I1: both lines are assumed to have free log(gf)

I2: only 6301.5 Å line has a free log(gf), while the other line has a fixed one

I3: only 6302.5 Å line has a free log(gf), while the other line has a fixed one

In each of these inversions, we also inferred the atmospheric parameters.

In Fig. 4.3, we show the comparison between inferred atmospheric parameters from SPINOR that has fixed atomic parameters and those from globin for the **I1** inversion run using the coupled method. The magnetic field strength and LOS velocity are comparable to results from SPINOR, indicating that the log(gf) parameter has a low cross-talk with these atmospheric parameters and, therefore, an insignificant influence on their retrieval. However, the panels for temperature indicate a more significant deviation from what is retrieved using SPINOR. This shows the cross-talk between the temperature and log(gf) parameters, primarily to the temperature around the formation height of the observed lines (node at $\log \tau = -0.8$). A very similar result is obtained for inversion run **I2**, while the retrieved temperature at $\log \tau = -0.8$ for inversion run **I3** is lower compared to the result from SPINOR.

The retrieved values of the log(gf) parameter obtained from the three inversions are presented in Tab. 4.2. These values are somewhat distant from the values in Tab. 4.1. However, the difference between retrieved log(gf) values is very similar in all three inversions. This indicates that the coupled method tends to keep the difference of log(gf) values fixed throughout the inversion to reproduce the observed line profiles. Inverting the observations of multi-line spectra and assuming that all lines have unknown log(gf), we can retrieve correct relative log(gf) for each line, but not the absolute values. In the inversion example from Sec. 3.2, we had to fix the log(gf) parameter of one spectral line.
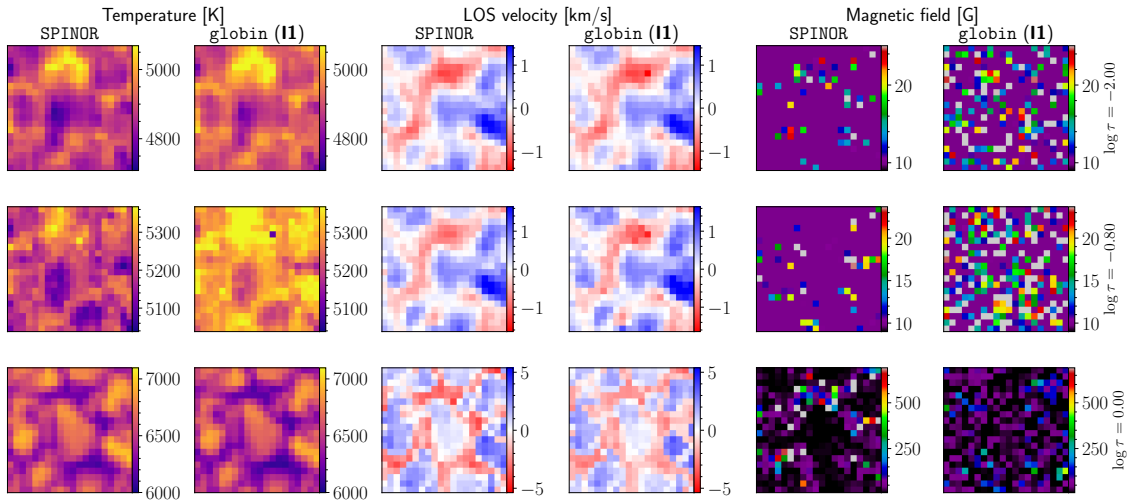
Figure 4.3. Similar comparison as in Fig. 4.2 between SPINOR and globin for the **I1** inversion run. All colour maps have the same scaling as in Fig. 4.2.

Table 4.2. The retrieved $\log(gf)$ values of Fe I 6301.5 Å and 6302.5 Å lines using the coupled method. The Δ parameter is a difference in $\log(gf)$ values of the two lines.

run	$\log(gf)_{6301.5}$	$\log(gf)_{6302.5}$	Δ
I1	-0.509	-0.980	0.471
I2	-0.493	-0.968	0.475
I3	-0.718	-1.196	0.478

We must be cautious in interpreting these results because we do not have an absolute truth to which we can compare the atmospheric and/or $\log(gf)$ parameters. The result from Fig. 4.3 indicates that we can trust the inferred LOS velocity and magnetic field strength at all depths even with significantly different $\log(gf)$ values for the two iron lines. The same trust can also be given, to some degree, to the temperature in the highest and deepest nodes but not to the temperature at the formation height of these lines (middle node).

Lastly, but very important for future analysis of Hinode/SP observations, this result indicates that $\log(gf)$ value for 6302.5 Å line listed in the VALD database is poorly determined. Trusting the experimentally estimated $\log(gf)$ value for 6301.5 Å line implies that the $\log(gf)$ value for 6302.5 Å line should be around -1.196. From fitting the central depth of a line in the spatially averaged spectrum of the quiet-sun region, Thevenin (1990) has determined that $\log(gf)$ of 6302.5 line is -1.16. The same value is determined by Socas-Navarro (2011) fitting the whole line profile from the same spectrum. These results support the retrieved $\log(gf)$ value for 6302.5 Å line that we obtain by applying the coupled method to the Hinode spectra from the quiet-sun region.

We cannot firmly conclude this result for now, and we aim to further explore the inference of $\log(gf)$ values for these two lines, which are very important and used very often for studying the solar atmosphere. Since these two lines show NLTE effects that are not negligible (Smitha et al. 2020), we should also aim to infer their $\log(gf)$ values by modelling them in NLTE.

4.2   Finding the optimal strategy for inferring the $\log(gf)$ parameter

The coupled method does not require spatially coherent pixels to infer the atomic parameters. This gives us the freedom to select pixels from an observed field of view which sample different solar features and whose Stokes profiles would be reproducible using the chosen node parametrisation of the atmospheric model. The observed line profiles show the underlying complexity of atmospheric parameter stratification. For example, strong gradients in the line of sight velocity will produce very asymmetric profiles. Flexibility to select pixels is a favourable option since the coupled method simultaneously fits all observed spectra, and having at least one pixel with a spectrum that is irreproducible would hinder a reliable retrieval of all inversion parameters.

To assess the optimal strategy for inferring the $\log(gf)$ parameter of many lines in the observed spectra, we select pixels that represent umbra, penumbra and quiet-sun region from a 3D MHD atmospheric model of a sunspot (Rempel 2012, the same MHD model was also used in Sec. 3.2). We constructed samples of 40, 80, 200, 1000 and 2000 pixels from this MHD model, retaining the same fraction of umbra (8%), penumbra (14%) and quiet-sun pixels (78%). The selected pixels in the sample totalling 1000 atmospheres are shown in Fig. 4.4. Pixels are selected randomly on a uniform polar grid without selecting a given pixel more than once in a given sample. However, there could be overlaps in pixels between different samples.

We synthesised the spectra for each constructed sample over the same spectral region as in Sec. 3.2. These synthetic observations are inverted using the same setup as in Sec. 3.2, inferring the atmospheric parameters and the $\log(gf)$ and $\Delta\lambda$ parameters of each line. Again, line 13 from this spectral region has its atomic parameters fixed to the value used to synthesise these spectra. The accuracy of the retrieved $\log(gf)$ values for all the lines, using either the pixel-by-pixel or the coupled method, is estimated with the standard deviation of $\log(gf)_{\mathrm{inv}} - \log(gf)_0$ weighted by the line core depth measured from the FAL-C atmosphere spectrum. Using this type of weighting, a higher importance is given to stronger lines, which are often less blended than weaker lines.

The weighted standard deviation $\sigma_{\log(gf)}$ for each sample is shown in Fig. 4.5. The $\log(gf)$ value retrieved for each spectral line by the pixel-by-pixel method is averaged over 25% of all pixels with the lowest χ^2 value. The standard deviation of $\sigma_{\log(gf)}$ for samples containing from 40 to 200 pixels is estimated using the bootstrap method on the results from the sample with 1000 pixels. The same figure shows the results from two different inversions using the coupled method. In the first one, spectra from all the pixels in a sample are inverted using the coupled method. We select 50% of pixels from this inversion with the lowest χ^2 (half-sample). We then repeat the inversion of the half-sample using the same initial conditions as we used for the whole sample (the same ones are also used for the pixel-by-pixel inversion). The results from this inversion are displayed with orange squares in Fig. 4.5. In the second inversion using the coupled method, we select again 50% of pixels with the lowest χ^2 from the half-sample, which now represent only 25% of the original sample size (quarter-sample). The results from this inversion are displayed with red squares in Fig. 4.5.

The samples' results in Fig. 4.5 show how the pixel-by-pixel method struggles to re-
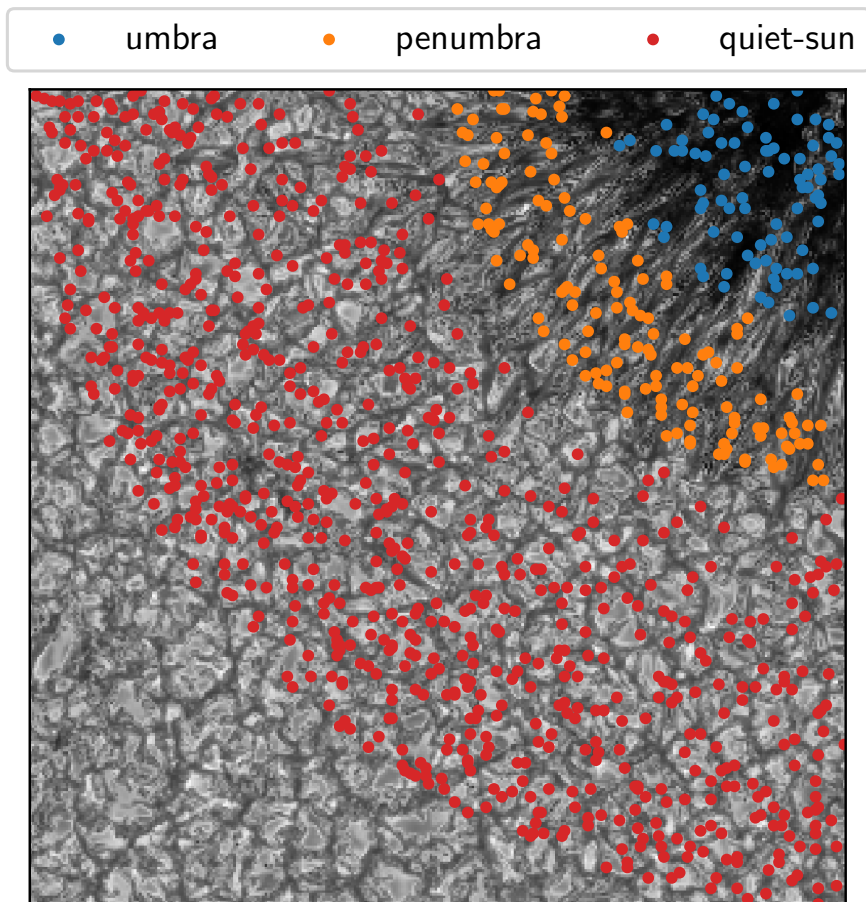
Figure 4.4. The selected pixels from the employed MHD simulation represent the umbra (blue dots), penumbra (orange dots) and quiet-sun (red dots) for the sample with 1000 pixels.

trieve the $\log(gf)$ parameter as reliably as in the coupled method. This indicates the inability of the pixel-by-pixel method to retrieve simultaneously the expected values for temperature and $\log(gf)$ parameter. Because of the averaging of $\log(gf)$ values over many pixels in the pixel-by-pixel method, one expects that increasing the number of pixels in a sample and selecting the very best ones may lead to a smaller $\sigma_{\log(gf)}$. This seems to be a poor assumption, most probably because the line blending hinders the LM algorithm from optimizing for $\log(gf)$ of these very weak and blended lines pushing $\sigma_{\log(gf)}$ to higher values. On the other hand, the coupled method shows a steady decrease and saturation of $\sigma_{\log(gf)}$ with an increasing number of pixels in a sample. The inversion of half-samples and quarter-samples allows the coupled method to reproduce the observed Stokes profiles better, lowering the χ^2 value and allowing weaker and more blended lines to impact the final χ^2. This selection of pixels improves the accuracy of retrieved $\log(gf)$ values for weak and blended lines in a spectrum more than for strong and isolated ones. However, further testing is necessary for a better and more robust comparison, which requires uncertainty estimates for the retrieved $\log(gf)$ values. This will be investigated in the follow-up study.
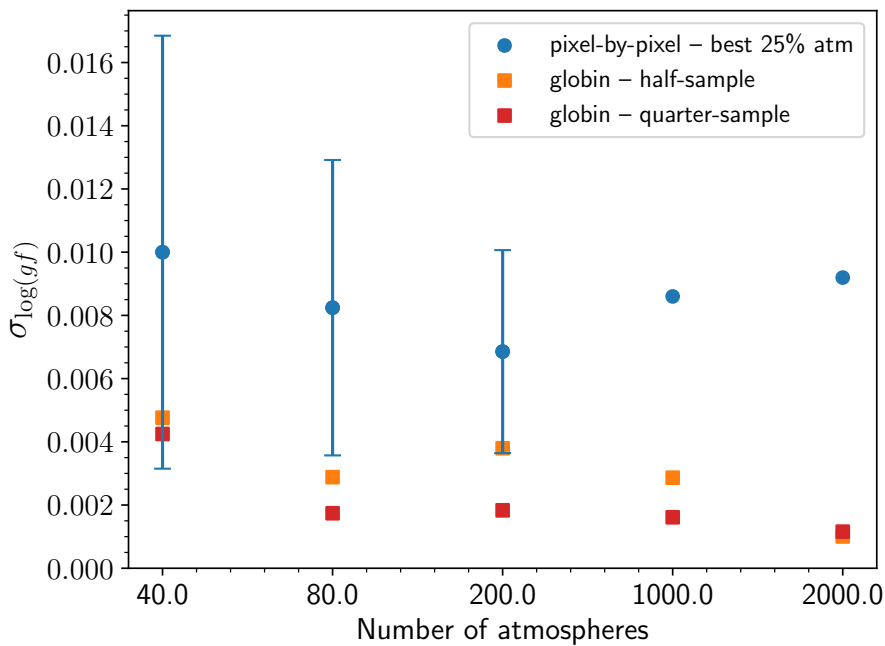
Figure 4.5. The weighted standard deviation of $\log(gf)_{\mathrm{inv}} - \log(gf)_0$ for each sample of atmospheres. Blue circles correspond to results from the pixel-by-pixel method, while the orange and red squares correspond to results from the coupled method applied on a half-sample and quarter-sample.

The analyzed spectra are ideal, and the impact of observational noise on the results has not been considered for now. Adding the noise to the synthetic spectra is expected to diminish the contribution of weak lines to the χ^2 and completely hinder the inference of their $\log(gf)$ parameter. However, it still needs to be tested as to how significant the noise will impact inferring the correct $\log(gf)$ parameter for lines that are significantly above the noise level and/or blended.

Further on, we still have to investigate the minimum number of atmospheres needed to retrieve accurate $\log(gf)$ values for many lines using the coupled method and check how this number depends on line blending. The half-samples and the quarter-samples contain pixels representing the umbra, penumbra and quiet-sun region whose fraction differs from the one in the full sample. We still have to explore if inverting the spectra from a particular solar feature introduces biases in inferred $\log(gf)$ values compared to inverting diverse spectra observed from different solar features.

4.3   Inference of the opacity fudge coefficients

The motivation to tackle the problem of poorly known atomic parameters comes from the work by Riethmüller & Solanki (2019), who showed a large discrepancy between the spatially averaged observed spectrum and the average synthetic spectrum from a 3D atmosphere in the NUV. Sources of this discrepancy could come from poor atomic line parameters, missing continuum opacity and significant uncertainties in adopted collisional coefficients of spectral lines. Therefore, we must first understand and model these sources

appropriately to retrieve reliable atmospheric parameters from NUV spectra.

We have already shown the benefits of using the coupled method for retrieving the atomic line parameters ($\log(gf)$ and $\Delta\lambda$) from observed spectra. Trusting that ABO theory correctly models the collisional broadening of lines, in this section, we discuss the possibility of determining the missing UV continuum opacity from observed spectra. The computed UV continuum intensity is known to have a higher continuum level than the observed one, indicating a missing source of opacity in our calculations. This could be coming from the unaccounted millions of very weak unresolved absorption lines that form a thick line haze in the UV, thus reducing the level of the observed continuum. These lines originate from higher excitation levels of metals that mimic continuum opacity (line haze; Rutten 2019). Other sources of missing UV opacity come from poor modelling of ionisation edges of many elements located in the UV and not accounting for NLTE electron number density in computing the continuum opacity (Rutten 2021). The physical nature of the missing UV continuum opacity has yet to be fully understood.

There are multiple ways to model the missing UV opacity. One way is to include all the lines from the Kurucz line list, which would make spectral synthesis very computationally demanding. The approximate solution to this problem is to bin the opacity in these lines and apply their contribution in wavelength bands. The constructed binned opacity is known as the opacity distribution function (e.g. Hubeny & Mihalas 2014) and it is used to construct line-blanketed stellar atmospheric models (e.g. Kurucz 1979). Another method for approximating the contribution of millions of spectral lines in modelling the line-blanketed atmospheres is developed in Busá et al. (2001).

An alternative way to model the missing UV opacity is to multiply the continuum opacity with wavelength-dependent coefficients until a satisfactory fit to the observed continuum is achieved. These coefficients are known as opacity fudge (OF) coefficients and are currently determined only for the quiet-sun atmosphere by matching the synthetic spectrum from the FAL-C atmospheric model to the spatially averaged quiet-sun disc centre spectrum (Bruls et al. 1992, Shapiro et al. 2010). Criscuoli (2019) showed how using the OF coefficients for spectral modeling from atmospheric models other than for the quiet-sun leads to a significant change in the estimated irradiance variability.

The RH code allows the user to specify OF coefficients freely, and by default, it takes the OF coefficients determined in Bruls et al. (1992). We have implemented in globin a possibility to infer pixel-dependent OF coefficients. These coefficients are estimated for each wavelength point specified by the user between which RH linearly interpolates. The position of each OF coefficient in a wavelength grid is arbitrary and allows for modelling strong gradients in the continuum opacity caused by the ionisation edges of metals.

It is expected that OF coefficients will have a cross-talk with the temperature at $\log \tau = 0$ because they both impact the continuum level similarly. This will further reflect on the retrieval of $\log(gf)$ parameter for observed lines because the strength of the line is sensitive to the ratio of line to continuum absorption coefficient. Therefore, we must find a way to decouple the contribution of OF coefficients and the temperature to the continuum to allow for reliable retrieval of the $\log(gf)$ parameter of NUV lines. One possibility would be to include an additional observation at a different wavelength region in inversions containing the true continuum – the continuum intensity, which can be properly modelled without additional fudging of the continuum opacity.

4.4 Inference of the elemental abundances

The abundance of chemical elements in other stars is measured in comparison to the abundance of these elements in the Sun, which illustrates the necessity of precise abundance measurement of elements in the solar atmosphere. The most recent review on the determination of solar abundances is presented in Asplund et al. (2021), based on matching a spatially averaged spectrum from a 3D radiative-hydrodynamical atmosphere model to a spatially averaged disc-center spectrum. Spectral lines of Na, Mg, K, Ca, and Fe are modelled in NLTE using detailed multi-level atomic models, while lines from other chemical elements are modelled in LTE. All these lines are modelled using a 3D approach in the solution of the radiative transfer equation. For some spectral lines, the center-to-limb variation of the spectrum is also used to confirm the quality of the adopted atomic line parameters (such as $\log(gf)$). All the assumptions used to construct the hydrodynamical models and synthesize the lines add to the uncertainties of the determined abundances of chemical elements.

However, it is possible to measure the abundances of different chemical elements using `globin` purely based on the observations and thus overcoming the uncertainties introduced by the selection of the simulations cube. The abundances could be added as an additional inversion parameter in the coupled method. It will be a challenge to simultaneously infer $\log(gf)$ and abundance and disentangle their contributions to the line absorption coefficient, which is $\log \chi^L \propto \epsilon + \log(gf)$. As it has already been discussed in Sec. 1.3.1.3, altering the $\log(gf)$ for some amount will cause the same change for ϵ, but with opposite sign, thus retaining the same χ^L. Therefore, we need a way to decouple these two parameters to infer reliably both. Based on the previous results for $\log(gf)$ inference, we expect that the abundance could be estimated by requiring that at least one line per chemical element has a known reliable $\log(gf)$. The best strategy would be only to use lines with reliable $\log(gf)$ values (experimentally measured ones) and determine the abundance from these lines alone. The same method is already used in Asplund et al. (2021), but the abundance can vary between lines of the same element. We should aim to correct the abundance in all lines simultaneously.

5 Conclusions and outlook

In this thesis, I have developed a new inversion method, called the coupled method, for inferring coupled atomic line parameters from high spatial and spectral resolution observations of the solar atmosphere. The main focus was on the $\log(gf)$ parameter describing the transition probability of a spectral line and $\Delta\lambda$ as uncertainty in the tabulated central wavelength of a line. The $\log(gf)$ parameter is one of the most important atomic parameters that alters the line strength and strongly impacts the inferred temperature stratification from observations. The $\log(gf)$ parameter is determined in laboratories (Sec. 1.3.1.1), from modelling atomic structure (Sec. 1.3.1.2) or from observed stellar and solar spectra (Sec. 1.3.1.3).

The method developed in this thesis improves the pixel-by-pixel method for inferring the $\log(gf)$ parameter presented in the work of Trelles Arjona et al. (2021) by introducing a coupling in atomic line parameters, thus imposing a simultaneous match of the synthetic spectra on the observed ones. In this way, the atomic line parameters can only vary simultaneously in all the pixels from an observed field of view. At the same time, this method allows for the retrieval of the atmospheric parameters in each pixel independently. The coupling of atomic parameters was necessary to effectively decouple temperature and $\log(gf)$ and enable the reliable retrieval of both parameters. The coupling of any global parameter, such as atomic parameters, requires rearranging the response functions for the inversion parameters, altering the block-diagonal form of the uncoupled global Jacobian matrix.

The coupled method is implemented in a new inversion code named `globin` developed in this thesis. The `globin` code is built around the `RH` code used for forward modelling of spectra in NLTE. Parts of the inversion algorithm related to the atmospheric parametrization are based on the methods already implemented in `SNAPI` and `STiC` inversion codes. The `globin` code is primarily developed to reliably infer coupled atomic parameters, which can be used afterwards to infer atmospheric parameters using any other, more sophisticated and specialized, inversion code. The `globin` code has been mainly used and tested for synthesis and inversion of LTE spectra. Since it is built around the `RH` code, there is no principle limitation to use `globin` also for NLTE spectral synthesis and inversion.

Sec. 3.2 shows the advantages of using the coupled method over the pixel-by-pixel method on LTE spectra computed from a 3D MHD atmospheric model for selected pixels, representing different solar features such as umbrae, penumbrae, granules and intergranular lanes. This test showed that coupling in atomic parameters enabled the inversion algorithm to decouple the contribution of blended lines and reliably infer their $\log(gf)$ and $\Delta\lambda$ parameters. In future work, the plan is to investigate how advantageous it is to use the coupled method to infer the atomic parameters of un-blended lines compared to

the pixel-by-pixel method.

The coupled method has already been applied to disc-center spectropolarimetric observations of a quiet-sun region made by the Hinode/SP instrument. Preliminary `globin` inversions of these data indicate that the widely used $\log(gf)$ value of Fe I 6302.5 Å line is poorly constrained, and it is planned to redetermine it using the coupled method. A very similar value for the $\log(gf)$ of this line is also obtained by Thevenin (1990) and Socas-Navarro (2011). Providing the wide solar physics community with the accurate $\log(gf)$ parameter of this line is of great interest since Hinode/SP observations are used frequently to study the solar atmosphere.

One of the significant aspects missing in the coupled method is an adequate way of estimating the uncertainty of inferred atomic parameters. This is very important to establish the accuracy of inferred parameters compared to values determined experimentally and theoretically. One way would be to use the Monte Carlo Markov Chain (MCMC) method to sample the parameter space and obtain their uncertainties. The MCMC method allows us to better assess the cross-talk between different inversion parameters by properly sampling the posterior probability distribution.

The development of the coupled method was motivated by the high spatial and spectral resolution observations in the near ultraviolet (NUV) expected from the instrument SUNRISE UV Spectropolarimeter and Imager (Feller et al. 2020) onboard the next flight of the balloon-borne SUNRISE observatory which has successfully flown twice before (Solanki et al. 2010, 2017) and is expected to fly again in June 2024. SUSI will continuously observe the Sun in the NUV spectral range from 309 nm to 417 nm. Radiation at these wavelengths is strongly absorbed by the Earth's atmosphere, which makes it hard to observe them from the ground. Riethmüller & Solanki (2019) showed many imperfections of modelled spectra when compared to available observations, one of which is poor atomic parameters, which must be corrected to better understand the solar atmosphere at these wavelengths.

The coupled method is general enough to be applied to spectral lines from UV to infrared formed under the assumption of LTE and NLTE. This method is not limited to the inference of $\log(gf)$ and $\Delta\lambda$ only; it can easily be extended to infer, e.g., elemental abundances or to improve an estimate of the continuum opacity correction in UV. The large number density of spectral lines in the UV hinders the proper line identification and estimate of the corresponding atomic parameters. We need precise wavelengths of many spectral lines to correctly identify the lines in line-rich UV spectra. We anticipate that future improvements in the coupled method could also assist in adequately identifying many lines and determining their atomic parameters. The improvements in the atomic parameters are essential for solar physics and the analysis and understanding of stellar atmospheres.

Bibliography

Alfvén, H. 1942, Arkiv för matematik, astronomi och fysik, 29B, 1

Anders, E. & Grevesse, N. 1989, Geochim. Cosmochim. Acta, 53, 197

Anstee, S. D. & O'Mara, B. J. 1995, MNRAS, 276, 859

Asplund, M., Amarsi, A. M., & Grevesse, N. 2021, A&A, 653, A141

Asplund, M., Grevesse, N., Sauval, A. J., & Scott, P. 2009, ARA&A, 47, 481

Asplund, M., Nordlund, Å., Trampedach, R., & Stein, R. F. 2000, A&A, 359, 743

Bahng, J. & Schwarzschild, M. 1961, ApJ, 134, 312

Bard, A., Kock, A., & Kock, M. 1991, A&A, 248, 315

Barklem, P. S. & Aspelund-Johansson, J. 2005, A&A, 435, 373

Barklem, P. S. & Collet, R. 2016, A&A, 588, A96

Barklem, P. S. & O'Mara, B. J. 1997, MNRAS, 290, 102

Barklem, P. S. & O'Mara, B. J. 1998, MNRAS, 300, 863

Barklem, P. S. & O'Mara, B. J. 2000, MNRAS, 311, 535

Barklem, P. S., O'Mara, B. J., & Ross, J. E. 1998, MNRAS, 296, 1057

Bigot, L. & Thévenin, F. 2006, MNRAS, 372, 609

Blackwell, D. E., Booth, A. J., Petford, A. D., & Laming, J. M. 1989, MNRAS, 236, 235

Blackwell, D. E. & Collins, B. S. 1972, MNRAS, 157, 255

Blackwell, D. E., Ibbetson, P. A., & Petford, A. D. 1975, MNRAS, 171, 195

Blackwell, D. E., Ibbetson, P. A., Petford, A. D., & Willis, R. B. 1976, MNRAS, 177, 227

Blackwell, D. E., Petford, A. D., Shallis, M. J., & Leggett, S. 1982, MNRAS, 199, 21

Boeche, C. & Grebel, E. K. 2016, A&A, 587, A2

Born, M. & Wolf, E. 1999, Principles of Optics: Electromagnetic Theory of Propagation, Interference and Diffraction of Light (7th Edition), 7th edn. (Cambridge University Press)

Borrero, J. M. & Bellot Rubio, L. R. 2002, A&A, 385, 1056

Borrero, J. M., Bellot Rubio, L. R., Barklem, P. S., & del Toro Iniesta, J. C. 2003, A&A, 404, 749

Borrero, J. M. & Ichimoto, K. 2011, Living Reviews in Solar Physics, 8, 4

Bridges, J. M. & Wiese, W. L. 1970, ApJ, 161, L71

Bruls, J. H. M. J., Rutten, R. J., & Shchukina, N. G. 1992, A&A, 265, 237

Busá, I., Andretta, V., Gomez, M. T., & Terranegra, L. 2001, A&A, 373, 993

Campbell, R. J., Keys, P. H., Mathioudakis, M., et al. 2023, ApJ, 955, L36

Carlsson, M. 1986, Uppsala Astronomical Observatory Reports, 33

Castellanos Durán, J. S., Korpi-Lagg, A., & Solanki, S. K. 2023, ApJ, 952, 162

Castellanos Durán, J. S., Lagg, A., Solanki, S. K., & van Noort, M. 2020, ApJ, 895, 129

Christensen-Dalsgaard, J., Dappen, W., Ajukov, S. V., et al. 1996, Science, 272, 1286

Cline, A. K. 1974, Commun. ACM, 17, 218–220

Collins, B. S., Petford, A. D., & Blackwell, D. E. 1970, Appl. Opt., 9, 1606

Cowan, R. D. 1981, The theory of atomic structure and spectra

Criscuoli, S. 2019, ApJ, 872, 52

de la Cruz Rodríguez, J. 2019, A&A, 631, A153

de la Cruz Rodríguez, J., Leenaarts, J., Danilovic, S., & Uitenbroek, H. 2019, A&A, 623, A74

de la Cruz Rodríguez, J. & Piskunov, N. 2013, ApJ, 764, 33

de la Cruz Rodríguez, J. & Socas-Navarro, H. 2011, A&A, 527, L8

Degl'Innocenti, E. L. 2014, Atomic Spectroscopy and Radiative Processes

del Toro Iniesta, J. C. 2003, Introduction to Spectropolarimetry

del Toro Iniesta, J. C. & Ruiz Cobo, B. 2016, Living Reviews in Solar Physics, 13, 4

den Hartog, E. A., Duquette, D. W., & Lawler, J. E. 1987, Journal of the Optical Society of America B Optical Physics, 4, 48

Den Hartog, E. A., Ruffoni, M. P., Lawler, J. E., et al. 2014, ApJS, 215, 23

Denker, C., Verma, M., Wiśniewska, A., et al. 2023, Journal of Astronomical Telescopes, Instruments, and Systems, 9, 015001

Feller, A., Gandorfer, A., Iglesias, F. A., et al. 2020, in Society of Photo-Optical Instrumentation Engineers (SPIE) Conference Series, Vol. 11447, Society of Photo-Optical Instrumentation Engineers (SPIE) Conference Series, 11447AK

Fischer, C. F., Godefroid, M., Brage, T., Jönsson, P., & Gaigalas, G. 2016, Journal of Physics B: Atomic, Molecular and Optical Physics, 49, 182004

Fontenla, J. M., Avrett, E. H., & Loeser, R. 1993, ApJ, 406, 319

Fox, N. J., Velli, M. C., Bale, S. D., et al. 2016, Space Sci. Rev., 204, 7

Frutiger, C., Solanki, S. K., Fligge, M., & Bruls, J. H. M. J. 2000, A&A, 358, 1109

Gingerich, O., Noyes, R. W., Kalkofen, W., & Cuny, Y. 1971, Sol. Phys., 18, 347

Goedbloed, J. P. H. & Poedts, S. 2004, Principles of Magnetohydrodynamics: With Applications to Laboratory and Astrophysical Plasmas (Cambridge University Press)

Gray, D. F. 2008, The Observation and Analysis of Stellar Photospheres

Grevesse, N. & Anders, E. 1991, in Solar Interior and Atmosphere, 1227–1234

Gurtovenko, E. A. & Kostik, R. I. 1981, A&AS, 46, 239

Gurtovenko, E. A. & Kostik, R. I. 1982, A&AS, 47, 193

Hammerschlag, R. H. & Bettonvil, F. C. M. 1998, New A Rev., 42, 485

Hibbert, A. 1975, Reports on Progress in Physics, 38, 1217

Holweger, H. & Müller, E. A. 1974, Sol. Phys., 39, 19

Hubeny, I. & Mihalas, D. 2014, Theory of Stellar Atmospheres

Huber, M. C. E. & Sandeman, R. J. 1986, Reports on Progress in Physics, 49, 397

Ichimoto, K., Lites, B., Elmore, D., et al. 2008, Sol. Phys., 249, 233

Jurčák, J., Schmassmann, M., Rempel, M., Bello González, N., & Schlichenmaier, R. 2020, A&A, 638, A28

Klose, J. Z. 1971, ApJ, 165, 637

Kosugi, T., Matsuzaki, K., Sakao, T., et al. 2007, Sol. Phys., 243, 3

Kramida, A., Yu. Ralchenko, Reader, J., & and NIST ASD Team. 2022, NIST Atomic Spectra Database (ver. 5.10), [Online]. Available: `https://physics.nist.gov/asd` [2023, July 31]. National Institute of Standards and Technology, Gaithersburg, MD.

Kurucz, R. & Bell, B. 1995, Atomic Line Data (R.L. Kurucz and B. Bell) Kurucz CD-ROM No. 23. Cambridge, 23

Kurucz, R. L. 1979, ApJS, 40, 1

Kurucz, R. L. 2002, in American Institute of Physics Conference Series, Vol. 636, Atomic and Molecular Data and Their Applications, ed. D. R. Schultz, P. S. Krstic, & F. Ownby, 134–143

Kurucz, R. L. & Peytremann, E. 1975, SAO Special Report

Landi Degl'Innocenti, E. & Landi Degl'Innocenti, M. 1977, A&A, 56, 111

Landi Degl'Innocenti, E. & Landolfi, M. 2004, Polarization in Spectral Lines, Vol. 307

Laverick, M. 2019, PhD thesis, KU Luven

Laverick, M., Lobel, A., Royer, P., Martayan, C., & Merle, T. 2017, Canadian Journal of Physics, 95, 843

Laverick, M., Lobel, A., Royer, P., et al. 2019, A&A, 624, A60

Leenaarts, J., Carlsson, M., & Rouppe van der Voort, L. 2012, ApJ, 749, 136

Leighton, R. B., Noyes, R. W., & Simon, G. W. 1962, ApJ, 135, 474

Levenberg, K. 1944, Quarterly of Applied Mathematics, 2, 164

Lites, B. W., Elmore, D. F., Seagraves, P., & Skumanich, A. P. 1993, ApJ, 418, 928

Marquardt, D. W. 1963, Journal of the Society for Industrial and Applied Mathematics, 11, 431

Martínez Pillet, V., del Toro Iniesta, J. C., Álvarez-Herrero, A., et al. 2011, Sol. Phys., 268, 57

Martins, L. P., Coelho, P., Caproni, A., & Vitoriano, R. 2014, MNRAS, 442, 1294

Mauas, P. J., Avrett, E. H., & Loeser, R. 1988, ApJ, 330, 1008

Metcalf, T. R. 1994, Sol. Phys., 155, 235

Milić, I. & van Noort, M. 2017, A&A, 601, A100

Milić, I. & van Noort, M. 2018, A&A, 617, A24

Müller, D., St. Cyr, O. C., Zouganelis, I., et al. 2020, A&A, 642, A1

Nave, G., Johansson, S., Learner, R. C. M., Thorne, A. P., & Brault, J. W. 1994, ApJS, 94, 221

Nave, G., Sansonetti, C. J., Townley-Smith, K., et al. 2017, Canadian Journal of Physics, 95, 811

Neckel, H. & Labs, D. 1984, Sol. Phys., 90, 205

Orozco Suárez, D., Bellot Rubio, L. R., del Toro Iniesta, J. C., et al. 2007, ApJ, 670, L61

Pastor Yabar, A., Borrero, J. M., & Ruiz Cobo, B. 2019, A&A, 629, A24

Peterson, R. C. & Kurucz, R. L. 2022, ApJS, 260, 28

Piskunov, N. E., Kupka, F., Ryabchikova, T. A., Weiss, W. W., & Jeffery, C. S. 1995, A&AS, 112, 525

Pradhan, A. K. & Saraph, H. E. 1977, Journal of Physics B Atomic Molecular Physics, 10, 3365

Press, W. H., Teukolsky, S. A., Vetterling, W. T., & Flannery, B. P. 2007, Numerical Recipes 3rd Edition: The Art of Scientific Computing, 3rd edn. (Cambridge University Press)

Quintero Noda, C., Shimizu, T., de la Cruz Rodríguez, J., et al. 2016, MNRAS, 459, 3363

Raouafi, N. E., Matteini, L., Squire, J., et al. 2023, Space Sci. Rev., 219, 8

Rempel, M. 2012, ApJ, 750, 62

Riethmüller, T. L. & Solanki, S. K. 2019, A&A, 622, A36

Roettenbacher, R. M., Monnier, J. D., Korhonen, H., et al. 2017, ApJ, 849, 120

Ruiz Cobo, B. & del Toro Iniesta, J. C. 1992, ApJ, 398, 375

Ruiz Cobo, B., Quintero Noda, C., Gafeira, R., et al. 2022, A&A, 660, A37

Rutten, R. J. 2003, Radiative Transfer in Stellar Atmospheres

Rutten, R. J. 2019, Sol. Phys., 294, 165

Rutten, R. J. 2021, arXiv e-prints, arXiv:2103.02369

Rybicki, G. B. & Hummer, D. G. 1991, A&A, 245, 171

Sanchez Almeida, J. 1992, Sol. Phys., 137, 1

Sánchez Almeida, J., Bonet, J. A., Viticchié, B., & Del Moro, D. 2010, ApJ, 715, L26

Schlichenmaier, R., von der Lühe, O., Hoch, S., et al. 2016, A&A, 596, A7

Schweikert, D. G. 1966, Journal of Mathematics and Physics, 45, 312

Seaton, M. J. 1987, Journal of Physics B Atomic Molecular Physics, 20, 6363

Shapiro, A. I., Schmutz, W., Schoell, M., Haberreiter, M., & Rozanov, E. 2010, A&A, 517, A48

Shchukina, N. G. & Vasil'eva, I. E. 2013, Kinematics and Physics of Celestial Bodies, 29, 53

Siu-Tapia, A., Lagg, A., Solanki, S. K., van Noort, M., & Jurčák, J. 2017, A&A, 607, A36

Siu-Tapia, A., Lagg, A., van Noort, M., Rempel, M., & Solanki, S. K. 2019, A&A, 631, A99

Smitha, H. N., Holzreuter, R., van Noort, M., & Solanki, S. K. 2020, A&A, 633, A157

Socas-Navarro, H. 2011, A&A, 529, A37

Socas-Navarro, H., de la Cruz Rodríguez, J., Asensio Ramos, A., Trujillo Bueno, J., & Ruiz Cobo, B. 2015, A&A, 577, A7

Solanki, S. K. 1987, PhD thesis, Max-Planck-Institute for Solar System Research, Lindau

Solanki, S. K. 2003, A&A Rev., 11, 153

Solanki, S. K., Barthol, P., Danilovic, S., et al. 2010, ApJ, 723, L127

Solanki, S. K., Riethmüller, T. L., Barthol, P., et al. 2017, ApJS, 229, 2

Sotirovski, P. 1971, A&A, 14, 319

Stenflo, J. 1994, Solar Magnetic Fields: Polarized Radiation Diagnostics, Vol. 189

Stix, M. 2004, The sun : an introduction

Thevenin, F. 1989, A&AS, 77, 137

Thevenin, F. 1990, A&AS, 82, 179

Tikhonov, A. N. & Arsenin, V. Y. 1977, Solutions of ill-posed problems (Washington, D.C.: John Wiley & Sons, New York: V. H. Winston & Sons), xiii+258, translated from the Russian, Preface by translation editor Fritz John, Scripta Series in Mathematics

Tiwari, S. K., van Noort, M., Lagg, A., & Solanki, S. K. 2013, A&A, 557, A25

Tiwari, S. K., van Noort, M., Solanki, S. K., & Lagg, A. 2015, A&A, 583, A119

Trelles Arjona, J. C., Ruiz Cobo, B., & Martínez González, M. J. 2021, A&A, 648, A68

Uitenbroek, H. 2001, ApJ, 557, 389

Uitenbroek, H. & Criscuoli, S. 2011, ApJ, 736, 69

Unsold, A. 1955, Physik der Sternatmospharen, MIT besonderer Berucksichtigung der Sonne.

Valori, G., Löschl, P., Stansby, D., et al. 2022, Sol. Phys., 297, 12

van Noort, M. 2012, A&A, 548, A5

van Noort, M., Lagg, A., Tiwari, S. K., & Solanki, S. K. 2013, A&A, 557, A24

Vernazza, J. E., Avrett, E. H., & Loeser, R. 1981, ApJS, 45, 635

Vocks, C., Mann, G., Breitling, F., et al. 2018, A&A, 614, A54

Vögler, A., Shelyag, S., Schüssler, M., et al. 2005, A&A, 429, 335

Vukadinović, D., Smitha, H. N., Korpi-Lagg, A., et al. 2023, A&A

Westendorp Plaza, C., del Toro Iniesta, J. C., Ruiz Cobo, B., et al. 2001, ApJ, 547, 1130

Wiese, W. L. 1970, Nuclear Instruments and Methods, 90, 25

A `globin` keywords

Below is the list of keywords that can be specified in the `params.input` file that control the behaviour of the `globin` code. The keywords have three types:

required: if the keyword is not provided, the code will raise an `InputError`.

default: if the keyword is not provided, a default value is assigned to it.

optional: keywords of this type are not required for the code to run.

The keyword type can change depending on the mode in which `globin` is being run. Also, there are keywords that are conditioned if some other keyword is provided or not (for example, keywords for constructing the wavelength grid).

General keywords used for optimal execution of `globin`

<u>mode</u> : required (int)
> mode in which to run `globin`.

>> `mode = 0`: spectral synthesis

>> `mode = 1`: pixel-by-pixel inference of atmospheric parameters only

>> `mode = 2`: pixel-by-pixel inference of atmospheric and atomic parameters

>> `mode = 3`: pixel-by-pixel inference of atmospheric parameters and the spatially coupled inference of atomic parameters using the globin method

> Each mode has a set of keywords which are required to be specified in order to run properly.

<u>n_thread</u> : optional (int) , 1   mode=all
> number of CPU threads used to compute the spectra (utilizes `multiprocessing.Pool()` object); if the `n_thread` is larger than the number of individual atmospheres in the input atmospheric model (or pixels in the observed field of view for `mode=1,2,3`), `n_thread` is reduced so that each spawned process takes one atmosphere.

The wavelength grid related keywords

<u>`wave_min`</u> : required/optional (float)   `mode=all`
    minimal wavelength used to construct the wavelength grid, in Angstroms.

<u>`wave_max`</u> : required/optional (float)   `mode=all`
    maximal wavelength used to construct the wavelength grid, in Angstroms.

<u>`wave_step`</u> : required/optional (float)   `mode=all`
    sampling of a wavelength grid, in Angstroms.

<u>`wave_grid`</u> : optional/required (str)   `mode=all`
    path to a file with list of wavelengths for which to compute the spectrum (in nanometers); used if one of `wave_min`, `wave_max` or `wave_step` is omitted.

The keywords referring to the characteristics of observed spectra to be inverted or to be computed

<u>`mu`</u> : default (float) , 1.0   `mode=all`
    $\mu = \cos(\theta)$ value for which to compute the spectrum. `ValueError` is raised if the value is outside the range $(0, 1]$.

<u>`spectrum`</u> : default (str) , 'spectrum.fits'   `mode=0`
    output file name of the synthetic spectra (in FITS format).

<u>`norm`</u> : default , False   `mode=all`
    controls the normalization of synthetic spectra. By default, we compute the spectrum in absolute units W/m^2/Hz/srad. Other normalization options are:

        `norm = 1`: the continuum is set to unity by dividing it with the intensity at the first wavelength point.

        `norm = hsra`: the spectrum is normalized with respect to the continuum intensity (at the first wavelength point) from the HSRA atmospheric model.

        `norm = ` I_c: the synthetic spectrum is normalized by dividing it with I_c value.

`observation` : required (str)   `mode=1,2,3`
    path to the file containing observations which we intend to invert. We assume that it is provided in FITS file format.

`obs_format` : default (str) , 'globin'   `mode=1,2,3`
    format of the `observation`. If `obs_format='globin'`, we assume that the `observation` has one FITS extension in which an array of full Stokes vectors along with the wavelengths is provided. The shape of the array is $(n_x, n_y, n_w, 5)$, where the first element in the last dimension corresponds to the wavelength. If `obs_format='hinode'`, we assume the FITS file has three extensions. In the first, we have an array of Stokes vectors with shape $(n_x, n_y, n_w, 4)$. The second one contains the array of wavelengths at which the Stokes vector is obtained. In the last one, the local continuum intensity used to normalize the Stokes vector.

`range` : optional   `mode=all`
    `mode=0`: specifies the range in x and y directions (in pixels) of `cube_atmosphere` for which we want to synthesise spectra. By default, we compute the spectrum for each atmospheric pixel.

    `mode=1,2,3`: specifies the range in x and y directions (in pixels) of `observation`, which we want to invert. By default, we invert the Stokes spectrum from every pixel.

`mean` : optional (bool)   `mode=all`
    flag controlling the spatial averaging of computed spectra.

`noise` : default (float) , 10^{-3} `mode=all`
    expected noise in Stokes profiles; in `mode=0` we add random Gaussian noise to the synthetic spectra; in `mode=1,2,3` we scale the merit function (see Eq. 2.1 and Eq. 2.12).

`weights` : default (float) , 1,1,1,1   `mode=1,2,3`
    comma-separated weights for each Stokes component used in computing the χ^2. By default, we assume that each Stokes component is equally weighted.

`weight_type` : optional (str)   `mode=1,2,3`
    type of weighting used in computing the χ^2 per wavelength. By default, we use equal weighting. If `weight_type=StokesI`, the inverse of Stokes I is used as weighting. This provides more weighting to the line cores, thus losing the information on the continuum.

`wave_weights` : optional (str)   mode=1,2,3

    path to the file containing wavelength and Stokes dependent weights. The file is assumed to have five columns: wavelength and weights for each Stokes component. The wavelength grid in this file has to correspond either to the constructed wavelength grid using keywords `wave_min`, `wave_max` and `wave_step` or to those provided in the `wave_grid` file.

`stray_factor` : optional (float)   mode=all

    the amount of stray light to be added to the spectrum; if the provided value is negative, it will be considered as the inversion parameter. `ValueError` is raised if the value is larger than 1.

`stray_type` : default (str) , 'grey'   mode=all

    the type of stray light contamination. By default, we assume wavelength-uniform stray light (grey straylight). If `stray_type = hsra`, the stray light is the spectrum computed using the HSRA atmosphere.

`stray_mode` : default (int) , 3   mode=all

    controls the way in which we apply/infer the stray light contamination.

        `stray_mode = 0`: apply the stray light of `stray_type` type.

        `stray_mode = 1,2`: infers the pixel dependent `stray_factor`.

        `stray_mode = 3`: infers the pixel independent `stray_factor`.

`instrumental_profile` : optional (str)   mode=all

    path to the file containing the instrumental profile to be used to convolve the synthetic spectra. The file has two columns: wavelength in Angstroms and the instrumental profile. When the instrumental profile is read, it is normalized and resampled to correspond to the wavelength grid on which we are synthesizing the spectrum.

The keywords referring to the characteristics of the input atmosphere used to compute the spectrum or the initial atmosphere in inversion mode

`cube_atmosphere` : optional (str)   mode=0

    path to the file contining an atmospheric model for which we want to synthesize spectra. We load the FAL C atmospheric model if `cube_atmosphere` is not specified.

`reference_atmosphere` : optional (str)   mode=1,2,3

    path to the file containing a reference atmospheric model used to construct the stratification of atmospheric parameters which are not inferred. We load the FAL C atmospheric model if `reference_atmosphere` is not specified.

`initial_atmosphere` : optional (str)   mode=1,2,3
    path to the FITS file format atmosphere, which contains the node positions and values for each atmospheric parameter that will be used as initial values. This atmosphere needs to of type `atm_type='globin'`.

`atm_type` : default (str) , 'multi'   mode=all
    type of the input atmospheric model (check Sec. 3.1.1).

`atm_scale` : default (str) , 'tau'   mode=all
    type of the scale used to stratify atmospheric parameters.

`logtau_top` : optional (float) , -6.0   mode=all
    top boundary of the atmosphere in $\log \tau_{5000}$.

`logtau_bot` : optional (float) , 1.0   mode=all
    bottom boundary of the atmosphere in $\log \tau_{5000}$.

`logtau_step` : optional (float) , 1.0   mode=all
    sampling of the $\log \tau_{5000}$ grid.

`vmac` : default (float) , 0   mode=all
    macro-turbulent velocity in km/s used to broaden the spectrum; if the provided value is negative and `mode=3`, it is considered as the inversion parameter.

`of_file` : optional (str)   mode=all
    path to a file in which the opacity fudge (OF) coefficients are specified (see example from Listing B.2). The file has two columns: the first column is the wavelength in nanometers, and the second one is the OF coefficient at the given wavelength. It is assumed that the OF changes linearly in wavelengths between given points. If there is only one row in the file, we assume that the OF correction is constant over the wavelength grid for which we are computing the spectra. For two or more rows, the smallest and the largest wavelength points for the OF correction are assumed to correspond to the boundaries of the wavelength grid. The OF correction is not applied to wavelengths outside those provided in `of_file`.

`of_fit_mode` : optional (int)   mode=all
    defines the mode in which we want to apply the opacity fudge (OF) correction. For `of_fit_mode = 0`, we only apply the OF from `of_file` to the synthetic spectra. For `of_fit_mode = 1`, we infer pixel-dependent OF coefficients.

`of_scatt_flag` : optional (int)   mode=all
>   controls if the OF correction should also be applied to the scattering coefficient:

>>   `of_scatt_flag=0` : no fudging

>>   `of_scatt_flag=1` : apply fudging

>   RH independently fudges the H^- opacity, scattering, and the opacity produced by metals. By default, the OF correction is applied only to the H^- opacity.

The keywords related to the inversion of atmospheric and atomic parameters

`nodes_parameter` : optional   mode=1,2,3
>   comma separated node positions for each atmospheric parameter. In the keyword name, `parameter` is substituted by `temp` for temperature, `vz` for line of sight velocity, `vmic` for micro-turbulent velocity, `mag` for magnetic field strength, `gamma` for magnetic field inclination and `chi` for magnetic field azimuth.

`nodes_parameter_values` : optional   mode=1,2,3
>   comma separated initial values for each node specified in `nodes_parameter`. The parameter units are temperature in Kelvin, line of sight velocity and micro-turbulent velocity in km/s, magnetic field strength in Gauss, magnetic field inclination and azimuth in degrees.

`nodes_parameter_vmin` : optional   mode=1,2,3
>   comma separated lower boundary values for each node specified in `nodes_parameter`. If a single value is provided, then each node's lower boundary is the same. By default, the lower boundary for temperature is 2800 K, line of sight velocity -10 km/s, micro-turbulent velocity 10^{-3} km/s, magnetic filed strength 10 G, magnetic field inclination $-180°$, and magnetic field azimuth $-360°$.

`nodes_parameter_vmax` : optional   mode=1,2,3
>   comma separated upper boundary values for each node specified in `nodes_parameter`. If a single value is provided, then each node's upper boundary is the same. By default, the upper boundary for temperature is 10 000 K, line of sight velocity and micro-turbulent velocity 10 km/s, magnetic field strength 10 000 G, magnetic field inclination 360°, and magnetic field azimuth 360°.

`nodes_parameter_reg_weight` : optional   mode=1,2,3
>   spatial regularization weight for a given `parameter`. It scales the `spatial_regularization_weight` because of unit differences between atmospheric parameters.

<u>spatial_regularization_weight</u> : optional (float)   mode=3
    regularization coefficient that controls the amount of spatial regularization added to the χ^2. `ValueError` is raised if the provided value is lower than 0.

<u>interp_method</u> : default (str) , 'bezier'   mode=1,2,3
    specifies the type of interpolating polynomial used to interpolate between nodes for the atmospheric parameters. Possible values are 'bezier' and 'spline'. Bezier interpolation is preferred because of the non-overshooting characteristic (see Sec. 3.1.2.1 for more details).

<u>interp_degree</u> : default (int) , 3   mode=1,2,3
    the degree of polynomial interpolation. Should be either 2 (for quadratic; supported only for `interp_method='bezier'`) or 3 (for cubic).

<u>spline_tension</u> : optional (float)   mode=1,2,3
    controls the tension of the spline interpolation polynomial: regular cubic spline is recovered for `spline_tension=0`. For `spline_tension` > 50, we have linear interpolation.

<u>lines2atm</u> : optional (str)   mode=1,2,3
    path to a file containing information on spectral lines, which will be used to initialize v_{LOS} and the magnetic field strength. We use the centre-of-gravity method to estimate v_{LOS} and the weak-field approximation for the magnetic field. Only the magnetic field strength is estimated, while the inclination and azimuth are taken from the `node_parameter_values`. This file has the following structure: the central wavelength of a line (in nanometers), wavelength window (in milli Angstroms), effective Landé factor, Landé factor of the lower and upper level, and J quantum number of the lower and upper level of a transition.

<u>line_parameters</u> : optional   mode=2,3
    path to a file containing the atomic line parameters to be inferred. The file has the following structure: name of the parameter (currently supported `loggf` for $\log(gf)$ and $\Delta\lambda$), line number in the Kurucz line list, initial value, lower boundary, upper boundary (see Listing B.4).

The keywords related to the Levenberg-Marquardt algorithm

<u>marq_lambda</u> : default (float) , 10   mode=1,2,3
    initial value of the Marquardt parameter λ_M.

<u>max_iter</u> : default (int) , 30   mode=1,2,3
    the maximal number of the Levenberg-Marquardt iterations in which inversion parameters are corrected for. For `ncycle` > 1, we can provide a comma-separated maximal number of iterations for each cycle or use a single value for each.

`chi_tolerance` : default (float) , 10^{-3} `mode=1,2,3`

the relative change of the χ^2 for which we stop the Levenberg-Marquard iteration.

`svd_tolerance` : default (float) , 10^{-5} `mode=1`

the tolerance value used to mask the SVD eigenvalues of the Hessian matrix. The eigenvalues lower than `svd_tolerance` are set to zero.

`ncycle` : default (int) , 1   `mode=1,2,3`

the number of inversion cycles. Each cycle has `max_iter` number of iterations. The atmospheric parameters are perturbed between each cycle to kick the Levenberg-Marquardt algorithm out of the local minimum. The atomic parameters are not perturbed between iterations.

`output_frequency` : default , `max_itter`   `mode=3`

the number of iterations after which the output files will be created (using the suffix `_c0`). Useful for checking intermediate results during long inversion runs.

B   Input files examples

File examples used to control the `globin` code and `pyrh` module. Additionally, we give examples of other relevant files that can be specified in `params.input` file.

Listing B.1. Example of `params.input` file used for spectral synthesis and applying the opacity fudge correction specified in `of.dat` file (see Listing B.2).

```
1  #--- General parameters
2  mode = 0
3  n_thread = 10
4
5  #--- Spectra related keywords
6  spectrum = spec_4016_muram_50G.fits
7  mu = 1.00
8  noise = 1e-3
9  norm = hsra
10
11 #--- opacity fudge parameters
12 of_fit_mode = 0
13 of_file = of.dat
14 of_scatt_flag = 1
15
16 #--- wavelength grid (in Angstroms)
17 wave_min = 4015.0
18 wave_max = 4017.0
19 wave_step = 0.002
20
21 #--- atmosphere
22 cubic_atmosphere = muram_50G.fits
23 logtau_top = -5
24 vmac = 1.85
```

Listing B.2. Example of `of.dat` file referred in Listing B.1.

```
1  # wavelength    OF coeff
2  401.5   0.20
3  401.6   0.17
4  401.7   0.10
```

In Listing B.3 we show an example of `params.input` file that inverts the observations synthesized in Listing B.1 using the globin method (`mode=3`). We allow the code to infer the temperature in four nodes; line of sight velocity, magnetic field strength, inclination and azimuth in three nodes and the height-independent micro-turbulent velocity. Additionally, we also infer the macro-turbulent velocity. In this example, we do not invert all the computed spectra but only for pixels in [1, 10] in the *x* direction and those in [4, 12] in the *y* direction. The atomic line parameters specified in the `line_pars_4016` are given in Listing B.4.

Listing B.3. Example of `params.input` file used for inversion.

```
1  #--- general parameters
2  mode = 3
3  n_thread = 1
4
5  #--- spectra/observation related keywords
6  observation = spec_4016_muram_50G.fits
7  obs_format = globin
8  mu = 1.00
9  noise = 1e-3
10 weights = 1, 10, 10, 7
11 norm = hsra
12 range = 1, 10, 4, 12
13
14 #--- opacity fudge parameters
15 of_fit_mode = 0
16 of_file = of.dat
17 of_scatt_flag = 1
18
19 #--- initial atmospheric parameters
20 vmac = -1.0
21
22 nodes_temp = -2.2, -1.5, -0.8, 0
23 nodes_temp_values = 4021, 5442, 6200, 7032
24
25 nodes_vz = -2.2,   -1.0, 0
26 nodes_vz_values = -0.2, 0.2
27
28 nodes_vmic = 0
29 nodes_vmic_values = 0.1
30 nodes_vmic_vmin = 0.1
31 nodes_vmic_vmax = 3
32
33 nodes_mag = -2.2, -1.0, 0
34 nodes_mag_values = 150, 150, 250
35 nodes_mag_vmax = 500
36
37 nodes_gamma = -2.2, -1.0, 0
38 nodes_gamma_values = 45, 45, 45
39
40 nodes_chi = -2.2, -1.0, 0
41 nodes_chi_values = 20, 20, 20
42
43 interp_degree = 3
44 interp_method = bezier
```

```
45
46 #--- wavelength grid (in Angstroms)
47 wave_min = 4015.0
48 wave_max = 4017.0
49 wave_step = 0.002
50
51 #--- Levenberg-Marquardt parameters
52 ncycle = 1
53 marq_lambda = 1e1
54 max_iter = 30
55 chi2_tolerance = 1e-3
56
57 #--- line parameters
58 line_parameters = line_pars_4016
59
60 #--- reference atmosphere (optional)
61 reference_atmosphere = holmul.spinor
62 atm_type = spinor
63 logtau_top = -4
```

Listing B.4. Example of a file containing the atomic line parameters to be inferred.

```
1  # parID    LineNo    initial      min       max
2  loggf        1      -2.309     -4.172    -0.672
3  loggf        2      -2.226     -3.806    -0.306
4  loggf        3      -0.223     -2.084     1.416
5  loggf        4      -0.609     -2.857     0.643
6  loggf        5      -0.919     -2.781     0.719
7  loggf        6      -2.371     -4.419    -0.919
8  loggf        7       0.247     -1.920     1.580
9  loggf        8      -0.672     -2.515     0.985
10 loggf        9      -0.123     -2.087     1.413
11 loggf       10      -2.119     -3.928    -0.428
12 loggf       11      -1.885     -3.870    -0.370
13 loggf       12      -0.649     -2.714     0.786
14 loggf       14      -3.783     -5.513    -2.013
15 loggf       15      -0.986     -3.160     0.370
16 loggf       16      -2.666     -4.905    -1.405
17 loggf       17      -2.620     -4.576    -1.076
18 loggf       18      -0.843     -2.547     0.953
19 dlam         1      10.184    -30.000    22.000
20 dlam         2       3.690    -30.000    22.000
21 dlam         3      -0.358    -30.000    22.000
22 dlam         4       1.545    -30.000    22.000
23 dlam         6      -4.571    -30.000    22.000
24 dlam         7       4.129    -30.000    22.000
25 dlam         9      -2.068    -30.000    22.000
26 dlam        10      -1.523    -30.000    22.000
27 dlam        11       6.368    -30.000    22.000
28 dlam        12      -6.217    -30.000    22.000
29 dlam        14      -3.025    -30.000    22.000
30 dlam        15      -8.857    -30.000    22.000
31 dlam        16       1.442    -30.000    22.000
32 dlam        17      -3.370    -30.000    22.000
33 dlam        18       1.884    -30.000    22.000
```

C Comparison of numerical schemes used to compute the response function

The computation of the response functions is the most time-consuming part of an inversion algorithm. The `globin` code uses the central difference numerical scheme to compute response functions of inversion parameters, which requires two spectral synthesis per parameter. A simpler and faster approach would be to use the forward difference numerical scheme, which requires only one spectral synthesis per parameter. Fig. C.1 displays the comparison between response functions computed using the central and forward difference methods and their relative difference. These response functions are computed from the FAL-C atmospheric model having a magnetic field vector with $B = 800\,\text{G}$, $\theta = 60°$ and $\phi = 30°$. The relative difference between these response functions is less than $O(10^{-2})$, which is acceptable for inversion purposes.
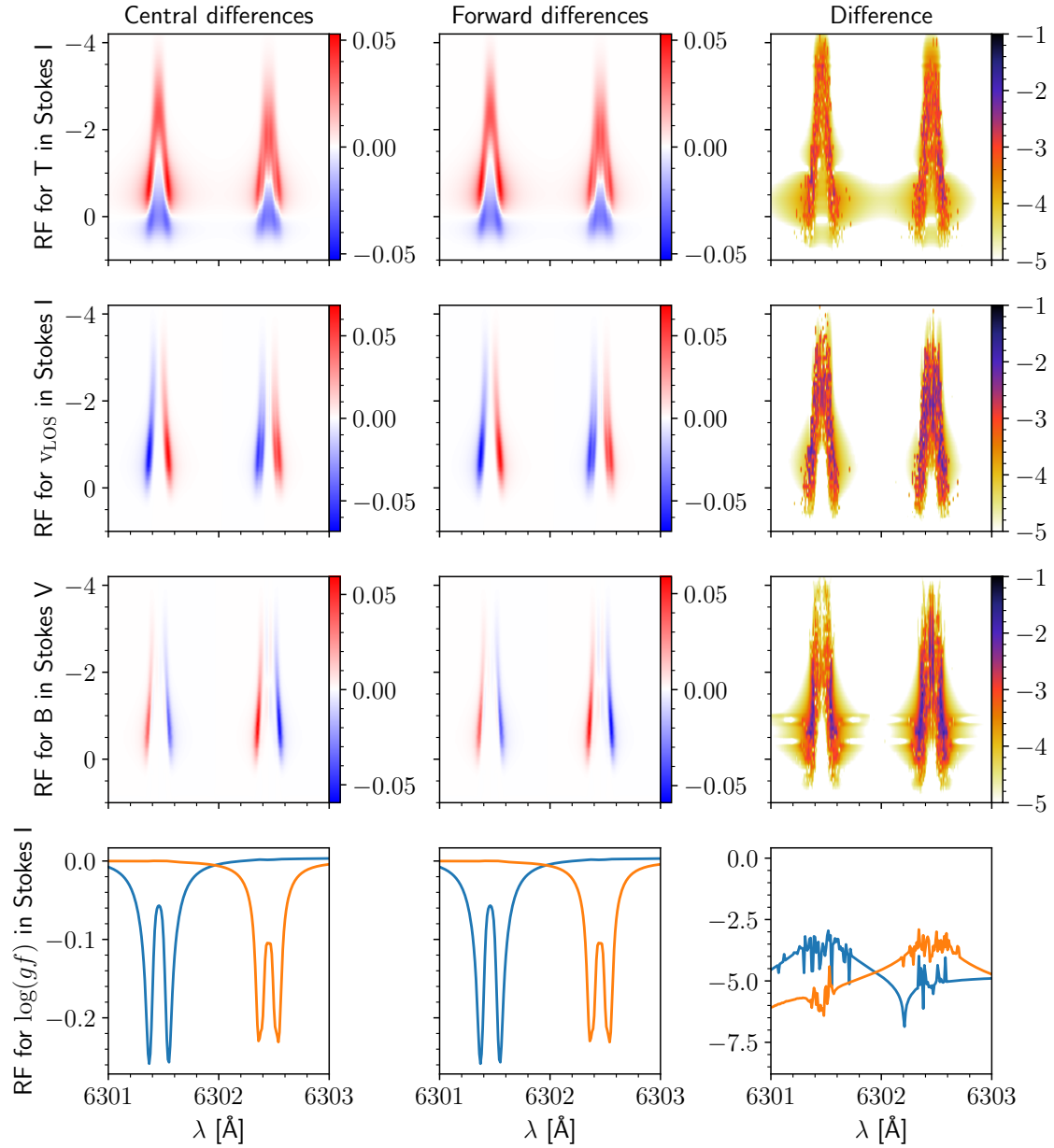
Figure C.1. Comparison between response functions computed using the central difference method (first column) and the forward difference method (middle column). Their relative difference in the logarithmic scale is displayed in the last column. We chose to show the Stokes *I* response function for temperature (first row), LOS velocity (second row) and $\log(gf)$ (fourth row) and the Stokes *V* response function for the magnetic field strength (third row).

Acknowledgements

Not many theses are completed without advice and support from many people, and this one is no exception.

I would like to express a deep bow to Andreas Korpi-Lagg, who strongly supported my doctoral project and provided valuable scientific, technical, and personal advice over the years. In the times when I doubted myself and my coding skills, he was always there to bring my optimism back on track.

Nothing less, I owe to Smitha Narayanamurthy for her efficient and clever guidance throughout the project. Thank you for all your time and patience for my, sometimes stupid and silly, questions regarding the radiative transfer theory. Thank you for supporting the idea of students and organising the course in radiative transfer for us.

To Sami Solanki, from whom I learned many things in solar physics in a few meetings that we had together over the years. These meetings and intermittent discussions helped me to see a broader picture of my project.

To Michiel van Noort, whom I should have bothered more over these years for... Anything that I could think of. Even though you were very busy, you always allocated time and energy to explain to me the beautiful world of radiative transfer, inversions and solar observations in an authentic way.

To Ivan Milić, who introduced me to the radiative transfer theory many years ago and who supported me and pushed me when I needed it in all my endeavours to reach this stage. It is always a great pleasure to discuss and work with you.

The time at the MPS would be boring without many great people. I have to start with those closest in space to me, and those are great office mates Tanay, Argiris and Sangitha, with whom I had plenty of discussions, not only about (solar)physics but also about basketball, camping, finances and so on and on till we realised, we have to work for a bit. On rare sunny days in Göttingen, I have managed to survive and enjoy long bike rides with Tanay, Jonas, Ilse, Paula, Neelanchal and Damien. Thank you for making those days memorable, and painful sometimes. To Jesper, with whom I share an understanding of the beauty in the world among us. To Nikolina, who was the only person I had talked with in person in months of strict pandemic measures. To Amanda, who always finds a way to make my day cheerful and spreads her positive energy and wisdom. I promise I will be less late for group lunch breaks. To Philipp, with whom I share an interest in baking. Waiting for the dough to rise was never boring, and it was filled with many discussions and views on what to do before you get old. To Johannes, Sebas, Francisco and Sam, who made time in Esrange enjoyable and fun. Being stranded above the polar circle for two months and running into the snow after the sauna was an amazing experience. I have unintentionally dragged Sebas into my project, on his own will, and since then, I have been learning many things about solar physics and observations from him. It is always

Scientific contributions

Publications

globin: a spectropolarimetric inversion code for the coupled inference of atomic line parameters
Vukadinović D., Smitha H. N., Korpi-Lagg A., van Noort M., Castellanos Durán J. S., Solanki S. K.
submitted to A&A; under revision

Investigating magnetic field inference from the spectral region around the Mg I b2 line using the weak-field approximation
Vukadinović D., Milić I., Atanacković O.
A&A **664**, A182 (2022)

Conferences and seminars

Second NLTE inversion workshop, Porto, Portugal (4th–6th of September 2023)
contributed talk

SOLARNET conference: The Many Scales of the Magnetic Sun, Potsdam, Germany (8th–12th of May 2023.)
contributed talk

Hinode-15/IRIS-12 conference, Prague, Czech Republic (19th–23rd of September 2022.)
poster

National Astronomical Observatory of Japan, online (16th of September 2022)
invited talk

European Solar Physics Meeting, online (6th–10th of September 2021.)
poster presentation

Virtual Annual Meeting of the German Astronomical Society, online (21st–25th of September 2020.)
poster presentation

First NLTE inversion workshop, Stockholm, Sweden (16th–18th of December 2019.)
contributed talk

Curriculum Vitae

Name: Dušan Vukadinović
Year of Birth: 1994
Nationality: Serbian

Education

Dr. rer. Nat. in physics
November 2019 – January 2024
International Max Planck Research School (IMPRS) at the Max Planck Institute for Solar System Research and University of Göttingen, Göttingen, Germany.
Thesis title: Inferring atomic line parameters from solar spectra
Supervisors: Sami K. Solanki, Stefan Dreizler, Andreas Korpi-Lagg and Michiel van Noort.

MSc in astrophysics
October 2017 – September 2018
Department of astronomy, Faculty of Mathematics, University of Belgrade, Belgrade, Serbia.
Thesis title: Formation and polarization in Mg I b line in solar spectrum.
Supervisors: Olga Atanacković, Ivan Milić, Dušan Onić.

BSc in astrophysics
October 2013 – September 2017
Department of astronomy, Faculty of Mathematics, University of Belgrade, Belgrade, Serbia.